Crystalline Morphologies of Poly(butadiene)-b-Poly(ethylene oxide) Block Copolymers in n-Heptane

DISSERTATION

zur Erlangung des akademischen Grades eines
Doktors der Naturwissenschaften
- Dr. rer. nat. -
der Fakultät Biologie, Chemie und Geowissenschaften
der Universität Bayreuth

vorgelegt von

Adriana Mirela Mihut

geboren in Zalau/ Rumänien

Bayreuth, 2009

Die vorliegende Arbeit wurde an der Universität Bayreuth in der Zeit von Oktober 2005 bis Oktober 2009 am Lehrstuhl für Physikalische Chemie I unter der Betreuung von Herrn Prof. Dr. Matthias Ballauff angefertigt.

Vollständiger Abdruck der von der Fakultät für Biologie, Chemie und Geowissenschaften der Universität Bayreuth zur Erlangung des akademischen Grades Eines doktors der Naturwissenschaften genehmigten Dissertation.

Dissertation eingereicht am: 21.10.2009
Zulassung durch die Promotionskommission: 28.10.2009
Wissenschaftliches Kolloquium: 03.02.2010

Amtierender Dekan: Prof. Dr. Stephan Clemens

Prüfungsausschuss:
Prof. Dr. Matthias Ballauff (Erstgutachter)
Prof. Dr. Andreas Fery (Zweitgutachter)
Prof. Dr. Werner Köhler
Prof. Dr. Axel H. E. Müller (Vorsitzender)

Anyone who has never made a mistake has never tried anything new.

(Albert Einstein)

To my family

Contents

Acknowledgments

Only with the support of the people around me I was able to complete this thesis. I am thankful to all of them.

I would like to express my gratitude to Prof. Matthias Ballauff for giving me the opportunity to carry out my PhD under his supervision. I want to thank him for sharing his scientific knowledge, for his patience and for the guidance in scientific writing. His support and guidance were central in advancing the quality of my work. It was a great chance to work with him.

My thanks to Prof. Andreas Fery for the inspiring discussions that will not be forgotten, for his help and great enthusiasm for science.

I would like to sincerely thank Prof. Georg Krausch, who guided my first steps as a researcher, for his encouragement and help through my first year of PhD here at the University of Bayreuth.

Words of thanks go to Dr. Holger Schmalz for his help during my research work and for our fruitful collaboration on block copolymers crystallization.

Dr. Arnauld Chiche is acknowledged for his constructive suggestions and scientific expertise that helped with the development of this project.

I owe special thanks to Dr. Larisa Tsarkova for her readiness in helping me and in answering my every question.

I am also obliged to Prof. Michael Wübbenhorst and Simone Napolitano of the Catholic University of Leuven (KUL) for their help and cooperation.

Financial support was provided by the European PolyFilm Network. Thanks to all members of this network for the constructive meetings and discussions we had. Special thanks to Prof. Günter Reiter, Dr. Dimitri Ivanov and Dr. Mark Geoghegan for the valuable scientific discussions.

My thanks go to Dr. Markus Drechsler, Markus Hund, Carmen Kunert and Ute Kuhn for their help during all these years.

I am grateful to all my colleagues, past and present for the pleasant time we spent together. Thanks to Dr. Kristin Schmidt and Dr. Günther Jutz for their friendship and support. My thanks to Dr. Frank Schubert, Heiko Schoberth and Christa Weber for their help during our measurement sessions at the ESRF synchrotron.

Many thanks to our secretaries, Sybille Zimmermann and Elisabeth Düngfelder, for their help with the paper work and good advice.

No doubt the one person whom I must thank most is Jérôme. Thank you for the help in preparing this thesis, for having the patience to read all my manuscripts, for the valuable scientific comments and for the continuous support throughout these years.

I would also like to thank the members of the examination committee for reading this manuscript.

Finally I would like to mention my family. This thesis is dedicated to them. There are no words I could thank them for their unfailing support, and guidance. I could not have achieved this without your support.

CHAPTER 1

Introduction

Crystallization is one of the most important properties of polymers, and its understanding is necessary especially in relation with the performance of polymeric materials. The polydisperse nature of polymer chains, the high degree of entanglements between long chains in polymer melts, and the presence of the chain folds introduce structural complexities in polymer crystals. As the kinetics of polymer crystallization and morphology are controlled by factors such as molecular weight, chain flexibility, or chain defects, they differ from that of small molecules. The crystallization process is also affected by experimental conditions such as temperature, pressure, nucleating agents, or stress.

1.1 Polymer Crystallization

1.1.1 Background: discovery of chain folding

It is known that polymeric materials crystallize only partially, i.e., the bulk polymers consist of microscopic crystalline and amorphous phases. The first model describing polymer crystals in the solid state was the so-called fringed micelle model [1]. According to this model, the polymer chains thread their way through several crystallites via intermediate region, as shown in Fig. 1.1. The observation that polymer single crystals are very thin platelets (10 nm) and that the chain axis is approximately perpendicular to the crystal basal plane led Keller to the chain-folding model [2]. Keller concluded in 1957, based on electron-diffraction patterns, that a single polymer chain threads though the same crystal many times by folding regularly on the crystal basal surfaces. Since the length of the polymer molecules exceed by many times the crystal thickness, the polymer chain must be folded. Such thin platelets are called *chain-folded lamellar crystals* (Fig. 1.2).

The phenomenon of folded-chain crystallization in long chain polymer molecules trig-

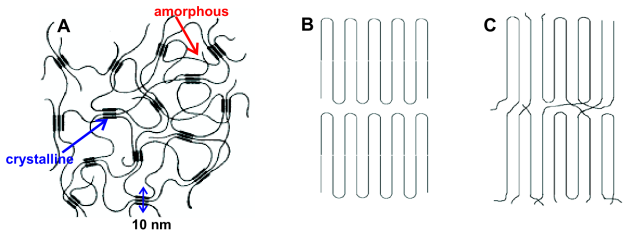

Figure 1.1: Schematic illustration of: (A) fringed-micelles model; (B) the folded chain crystal, showing adjacent re-entry; (C) the switchboard model.

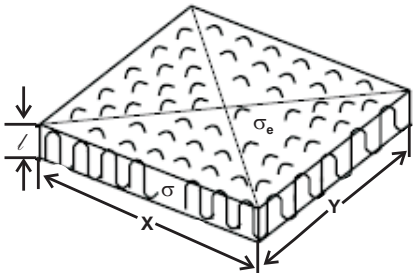

Figure 1.2: Schematic of chain-folded lamellae structure in semicrystalline polymers with lateral dimensions x, y and thickness l, σ and σ_e are the surface free energies associated with lateral and fold surface respectively.

gered numerous research activities in the new area of polymer crystallization. It is now establish that adjacent re-entry folding of the polymers occurs upon crystallization in solution while in bulk in the switchboard model chains do not have re-enter into lamellae by regular folding but re-enter more or less randomly (Fig. 1.1).

Various models have been proposed to explain the crystallization behavior of polymers, especially to explain the faceted growth in solution-growth crystals and the inverse relationship between the degree of supercooling and fold-length, i.e., the decrease in crystal thickness upon lowering of the crystallization temperature. The obvious question is: why do polymer chains fold upon crystallization instead of forming extended chain crystals? An easy answer is that the kinetic energy barrier of the folded-chain crystals is lower, and consequently the crystals form faster then extended chain (EC) crystals, namely crystallization is controlled by kinetics (Fig. 1.3).

The Gibbs free energy G of folded-chain crystals is higher then that of the equilibrium extended-chain crystals, and they will melt accordingly at a lower temperature as shown in Fig. 1.4. In the case of polymer crystals, we have to differentiate between the equilibrium melting temperature T_m^0 and the actual melting temperature T_m, which is dependent on the fold length or crystal thickness.

The thermodynamic driving force for crystallization $\Delta G = G_L - G_{EC}$ at crystallization temperature T_c is given by:

$$\Delta G = \Delta H - T\Delta S \tag{1.1}$$

where ΔH and ΔS represent the enthalpy and the entropy, respectively. At the equi-

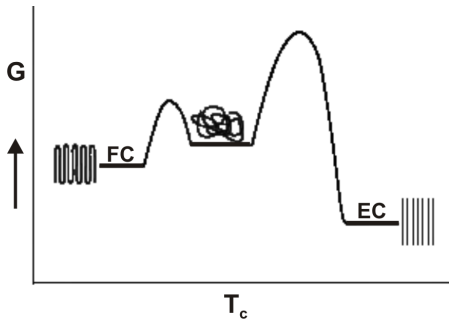

Figure 1.3: Folded-chain (FC) vs. Extended-chain (EC) crystallization.

librium melting temperature, T_m^0, $\Delta G = 0$ and

$$T_m^0 = \Delta H / \Delta S \tag{1.2}$$

Substituting eq 1.1 into eq. 1.2 gives:

$$\Delta G = \Delta H (T_m^0 - T)/T_m^0 \tag{1.3}$$

The driving force for crystallization can be approximated at a particular crystallization temperature T_c as:

$$\Delta G = \Delta H \Delta T / T_m^0 \tag{1.4}$$

with $\Delta T = T_m^0 - T_c$.

Folded-chain crystals are metastable and melt below the equilibrium melting temperature T_m^0, see Fig. 1.4. The determining factor is the relatively small dimensions of the crystals in the chain direction, 10-30 nm.

1.1.2 Thermodynamics of Polymer Crystallization

The formation of lamellar platelet-like crystals during polymer crystallization results in a large amount of specific surface area which reduces their thermodynamic stability. Two types of surface free energy, σ_e and σ have been defined, which are associated with the fold and lateral surfaces, respectively, as shown in Fig. 1.2. The free energy of fusion for a lamellar single crystal described in Fig. 1.2 can be expressed as:

$$\Delta G_f = xyl\Delta G_f^\infty - 2xy\sigma_e - 2l(x+y)\sigma \tag{1.5}$$

where ΔG_f^∞ is the free energy of fusion per unit volume for a perfect crystal with infinite dimension, x and y represent the dimensions of the basal crystal plane and l is the lamellar thickness defined on Fig. 1.2.

For infinitely large perfect crystals, for which the effect of surface free energies is

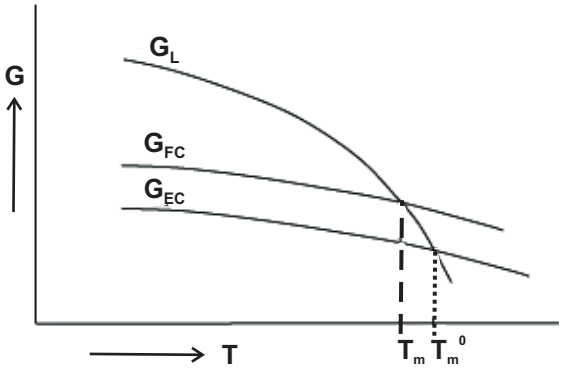

Figure 1.4: Gibbs free energy of : liquid phase (G_L), folded-chain (G_{FC}) and extended-chain (G_{EC})

neglected, the free energy of fusion is given as:

$$\Delta G_f^{\infty}(T) = \Delta H_f^{\infty}(T) - T\Delta S_f^{\infty}(T) \tag{1.6}$$

where $\Delta H_f^{\infty}(T)$ and $T\Delta S_f^{\infty}(T)$ are the enthalpy and entropy changes upon fusion at temperature T. At the equilibrium melting temperature, T_m, the melt is in equilibrium with the perfect crystal of infinite size.

Hence $\Delta G_f^{\infty}(T_m) = 0$, which gives:

$$T_m = \frac{\Delta H_f^{\infty}(T)}{\Delta S_f^{\infty}(T)} \tag{1.7}$$

For lamellar crystals with finite dimensions, the associated melting temperature $T_m^{'}$ can be calculated by substituting ΔG_f^{∞} with $\Delta G_f^{\infty}(T_m^{'}) = \Delta H_f^{\infty}(T_m^{'}) - T_m^{'}\Delta S_f^{\infty}(T_m^{'})$ in eq. 1.5 and using eq. 1.7. Assuming x, $y \gg$l and $\sigma \ll \sigma_e$, $T_m^{'}$ can be given as:

$$T_m^{'} = T_m(l - \frac{2\sigma_e}{l\Delta H_f^{\infty}}) \tag{1.8}$$

This is the famous Gibbs-Thomson (or Gibbs-Thomson-Tammann) equation which correlates the melting temperature and the thickness of a given lamellar crystal. According to eq. 1.8, the fold surface free energy σ_e, and the equilibrium melting temperature T_m can be estimated if the melting temperature can be determined experimentally as a function of lamellar thickness, given that ΔH_f^{∞} is known.

It should be noted that the above derivations are based on considerations of equilibrium thermodynamics, i.e., assuming $\Delta G = 0$ for the melting process. For a kinetic process, ΔG should be less than 0. Therefore, the above equations only set some bounds for polymer crystallization process. For example, the minimum lamellar thickness l that

will be stable at temperature T can be obtained from eq. 1.8:

$$l_{min} = \frac{2\sigma_e T_m}{\Delta H_f^\infty \Delta T} \tag{1.9}$$

where $\Delta T = T_m - T$, which is known as the supercooling. The l_{min} is the critical minimum length needed to form a thermodynamically stable nucleus. For polymer crystallization, it is widely accepted that the morphology and the growth rate of semicrystalline polymers are controlled by kinetic factors rather than by thermodynamic ones. Therefore, a theory based on kinetics is desired to describe the process of the crystallization.

1.1.3 Kinetic Theory of Polymer Crystallization

Two main kinetic theories have been proposed including the Lauritzen-Hoffman secondary nucleation (LH) theory [3] and Sadlers rough surface or entropic theory [4, 5, 6]. Both models share the assumption of a free energy barrier. The nature of the barrier distinguishes the LH theory from rough surface theory.

The driving force for crystallization is controlled by the supercooling. To describe the driving force quantitatively, the free energy change during crystallization, ΔG_c, can be used. For a lamellar crystal showed in Fig. 1.2, ΔG_c is expressed as:

$$\Delta G_c(T) = lxy\Delta G_c^\infty(T) + 2xy\sigma_e + 2l(x+y)\sigma \tag{1.10}$$

Here, $\Delta G_c^\infty(T) = \Delta H^\infty(T) - T\Delta S^\infty(T)$, $\Delta S^\infty(T) \approx \Delta S^\infty(T_m) = \Delta H^\infty(T_m)/T_m$ and $\Delta H^\infty(T) \approx \Delta H^\infty(T_m)$. In addition, σ can be neglected because the magnitude of the lateral dimension x, y ($\sim 10\mu$m) is much larger than that of the lamellar thickness l ($\sim 10nm$).

On the basis of these assumptions, and using eq. 1.9, $\Delta G_c(T)$ can be expressed as:

$$\Delta G_c(T) = lxy(2\sigma_e/l - \Delta H^\infty(T)\Delta T/T_m) = 2xy\sigma_e(l - l/l_{min}) \tag{1.11}$$

From eq. 1.11 one can see that $\Delta G_c(T) < 0$ if $l > l_{min}$. Therefore, the greater the lamellar thickness is, the larger is the free energy change during crystallization and the driving force.

The crystallization starts with the formation of the primary nuclei. The nucleation itself can be defined as the formation of a small amount of crystalline material due to fluctuations in density or order in the supercooled melt. The primary nucleation can be either homogeneous or heterogeneous. Homogeneous nucleation is the result of a single molecule or number of small molecules forming a nucleus with a size that is large enough to overcome the barrier of the primary nucleation. Heterogeneous nucleation typically occurs due to presence of dust, catalyst particles, or designed nucleating agents in the polymers.

To form stable nuclei the free energy barrier to crystallization needs to be overcome. The size of this critical nucleus obviously depends on this free energy barrier as represented in Fig. 1.5. Primary nucleation involves the largest specific area while the area

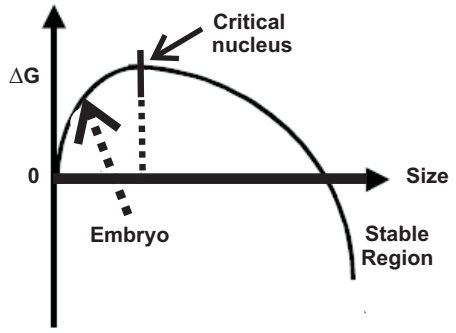

Figure 1.5: Variation of free energy with nucleus size. The initial free energy barrier needs to be crossed for the nucleus to become stable.

is reduced for secondary nucleation on the surface.

On the other hand, when an amount of chains deposits at the crystal growth front, the localization of the stem on the crystal surface is associated with a decrease in the entropy of the polymer chain. This leads to an entropic barrier that increases with crystal thickness. The growth rate therefore is the result of an interplay between the free energy barrier and the driving force and is proportional to $\exp(-1/\Delta T)$. The actual thickness of lamellar crystals corresponds to the thickness of crystals that have the largest growth rate under given experimental conditions. It should be noted that both the free energy barrier and the driving force are undercooling dependent. Besides undercooling, other factors such as the chain length and the concentration of defects on the chain backbone also have a significant influence on the growth rate and the final morphology.

1.2 Morphologies of Semicrystalline Polymers

When polymers crystallize from melt or solution, the size, shape, and regularity of the crystals depend on their growth conditions, such as solvent, temperature and concentration.

1.2.1 Melt Crystallization

Spherulite Structure

It is a well-established that a lamellar crystal is the fundamental structure formed by polymers when they crystallized from the bulk or from melt. When polymer samples are crystallized from the molten bulk, where the chains are highly entangled, the most commonly observed structures are spherulites (Fig. 1.6).

The spherulites are composed of stacks of individual lamellae of similar thickness and slightly diverging. X-ray and electron diffractions of the spherulites indicate that the c axis (which determines the thickness size) of the crystals is oriented tangentially to the radial (growth) direction of the spherulites. In order to obtain a spherical superstructure

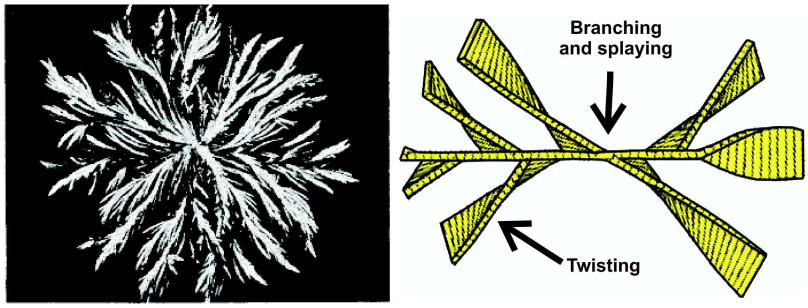

Figure 1.6: Polarized optical micrograph (left) of spherulite growth at 135^0C in a blend containing 40% of isotactic polypropylene blend and 60% of atactic polypropylene and development of the spherulite structure from planar crystals (right).
[7]

from planar lamellae, a mechanism for branching and splaying of the lamellae has to be available. Lamellar branching is produced by screw dislocations, which generate secondary lamellae from the mother crystal.

To explain the splaying of branching lamella, Bassett et al [8] proposed that during the process of attachment of stems to the growth surface of a growing crystal, the remaining uncrystallized part of a single chain is in the form of a cilium. The ensemble of cilia in the vicinity of the contact point should generate a positive internal pressure that makes the crystal arms to diverge. If the degree of branching of the growing lamellae is low, the superstructure obtained will not be spherical, and axialites will be formed (Fig. 1.6 (right)). Lamellar twisting is the phenomenon which leads to the apparition of a pattern of concentric rings (banding) in polymer spherulites. Keith and Padden [9] suggested that the lamellar twisting has its origin in the asymmetry generated by chain tilt, which introduces opposite bending moments between opposite fold surfaces.

Shish kebab Structure

Polymer shish kebab crystals were formed under shear field in melt or solution state. This was first observed in 1960s by Pennings [10, 11]. The electron micrograph in Fig1.7 cleared shows the structure of flow-induced PE shish kebab crystals. A shish-kebab polymer crystal usually consists of a central fibril (shish) and disc-shaped folded-chain lamellae (kebab) oriented perpendicularly to the shish. It is generally understood that the shish of these crystallites was formed by crystallization of fully stretched or extended chains.

The kebabs are believed to be folded-chain lamellar structures. The growth direction of the kebabs is normal to the shish. The chain alignment in the kebabs is parallel to the shish. For a polymer solution (i.e. 5% polyethylene/xylene) under an extension/shear flow, polymer chains which normally possess a coil conformation might undergo a coil-to-stretch transition [12]. If the chain is longer than a critical molecular weight, the stretched polymer chains aggregate to form extended fibrillar crystals [13]. The remaining coil polymer chains could then crystallize upon the fibrillar crystals in a periodic

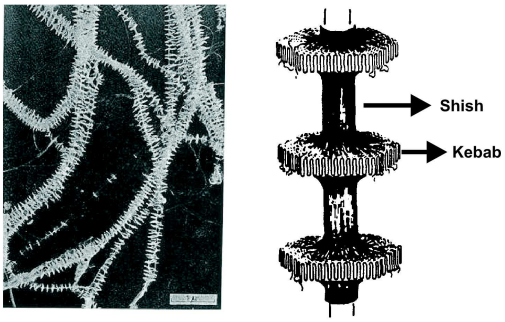

Figure 1.7: Electron micrograph and schematic of shish kebab structure. [10]

fashion, forming the shish-kebab morphology.

1.2.2 Crystallization from dilute solution

While the polymer crystallization from melt is well established and has been extensively reviewed, the crystallization in selective solvents is less understood. Crystallization in solution depends drastically on solvent selectivity. If the solvent is selective for the crystalline block, it can swell the crystalline lamellae (T_m is obviously reduced). In contrast, if the solvent is selective for the amorphous block, the semicrystalline copolymer can precipitate out in a nonequilibrium structure.

Early studies on the crystallization of block copolymer from solution mainly concentrated on the macroscopic morphology of the crystals formed and the crystallization kinetics. Lotz and Kovacs[14, 15] have been the first to study the morphology of polystyrene -*block*-poly(ethylene oxide)(PEO-*b*-PS) block copolymers crystallized from solution in 1960. They found that single crystals as square platelets with crystalline regions having the same structures as PEO homopolymers can be grown in dilute solutions as shown in Fig. 1.8. In this system, the PS blocks can be viewed as being tethered on the basal surfaces of the PEO block single crystal (substrate) to form a sandwiched structure. With a constant molecular weight of the PEO block and crystallization temperature, the thickness of the single crystal and thus, the number of folds, are fixed. This leads to a fixed tethering density. In other words, the tethering density can be adjusted by changing the crystallization temperature (undercooling) and the molecular weights of the crystalline blocks.

Gast and coworkers [16, 17] obtained large stable crystalline lamellae of polystyrene-*block*-poly(ethylene oxide) (PS-*b*-PEO) in cyclopentane. They have shown that the PEO crystallization and the resulting shaped lamellae can be switched off by the addition of a small amount of water that swells the PEO block, and results in spherical micelles with an amorphous core.

Self-consistent field theory was used to model the density profile of the tethered chains and SANS and SAXS were performed to provide the volume fraction profiles and the crystal domain thicknesses, which were compared with the predicted values from theory

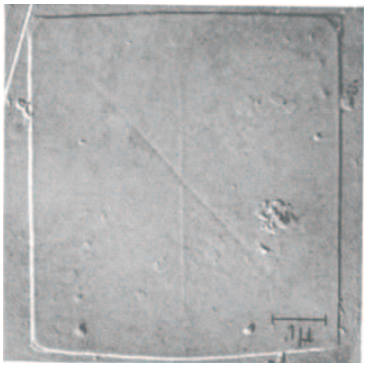

Figure 1.8: Replica of electron micrograph of PEO crystal grown from ethyl benzene at 25^0C.

[18]. The core thickness is due to the balance of an entropic contribution from the brush stretching and an enthalpic term from crystalline chain folding (and defects due to ethyl branches). Measurements were performed on solutions of polyethylene-*b*-poly(ethylene-alt-propylene) PE-*b*-PEP in *n*- decane (selective solvent for PEP).

1.2.3 Crystallization in micelles

When the insoluble block of a block copolymer is able to crystallize, crystal packing forces play a dominant role in determining the structure of the core objects that form. The core crystallinity affects the equilibrium state via the following two routes: (1) the chain fold crystallization determines the packing mode of the core blocks, and sets the relationship between grafting density of the amorphous block and core geometry; (2) the chain fold crystallization gives rise to two different surface tensions. One is associated with the folds plane, while the other characterizes the lateral surface which incorporates unlinked chain segments.

A scaling analysis of morphology of semicrystalline block copolymers in selective solvents has been publish by Vilgis and Halperin in which the insoluble block is crystalline [19]. In this model the insoluble block forms crystals through adjacent folds within the core, and a sharp interface divides the crystalline core from the solvent-swollen corona. The overall shape of the self- assembled structure depends on the interplay between the interfacial energy between the core and the solvent and stretching within the corona due to the overlap of adjacent coils. The corona chains are grafted to the core at a spacing that depends on the number of folds per core block. Thus, the response to strong corona chain repulsion is a large number of thinner folds in the crystalline core- forming chain. They identified two separate contributions to the interfacial free energy, one due to the interfacial tension σ_f in the fold plane and the other is due to the lateral interfacial tension σ_l at the edge of each crystal as shown in Fig 1.9.

The most common morphology expected from this model is lamellae with the corona chains protruding from both faces. If the soluble block is very long, cylindrical or even star-like micelles are expected. Because the core is formed by adjacent folds of the

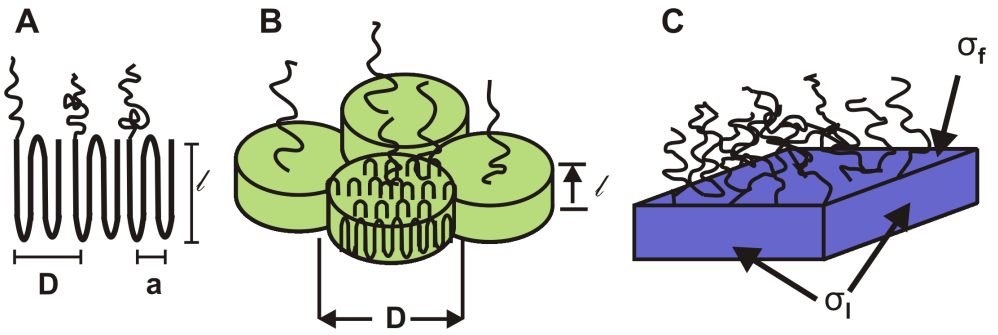

Figure 1.9: (A) Monolayer structure satisfying the Vilgis and Halperin model of how the crystalline block pack in an aggregate formed in a selective solvent. (B) Schematic representation of coil-crystalline lamellae where the crystalline blocks are depicted as cylinders with a coronal block attached to the bases centers. (C) Schematic platelet formed by coil-crystalline block copolymers showing the origin of σ_f and σ_l.

crystalline polymer, the core of a cylindrical micelles does not have a circular cross section but must be formed by end-to-end packing of a rectangular unit cell. Furthermore, they postulated that star-like micelles formed from polymers with long corona chains have a core in the form of a rectangular solid.

Vilgis and Halperin considered aggregates with a crystalline core, in which the crystalline chain, of length N_B, adopts a tight folding conformation (Fig. 1.9 (A)). A sharp interface divides the crystalline core from the solvent-swollen corona formed by the soluble block of length N_A. The corona chains are treated as though they are grafted to the core at a spacing that depends on the number of folds n_f per core block. Two interfacial energies enter into the description of the surface free energy per chain ($F_{surface}$), σ_f, the surface tension associated with the fold surface, and σ_l, the lateral surface tension.

$$\frac{F_{surface}}{kT} = n_f \frac{\sigma_f a^2}{kT} + n_f^{-1/2} N_B \frac{\sigma_l a^2}{kT} \tag{1.12}$$

where a is the size of the monomer, T is temperature, and k is the Boltzmann constant. A representative structure showing the origin of σ_f and σ_l is shown in (Fig1.9 (C)). The equilibrium free energy of a lamellae is expressed as:

$$\frac{F_{surface}}{kT} = N_B^{2/3} \frac{\sigma_l^{2/3} \sigma_f^{1/3} a^2}{kT} \tag{1.13}$$

Within the core, the distance D between grafting sites and the layer thickness l are given by

$$D = N_B^{1/3} (\sigma_l / \sigma_f)^{1/3} a \tag{1.14}$$

$$l = N_B^{1/3} (\sigma_f / \sigma_l)^{2/3} a \tag{1.15}$$

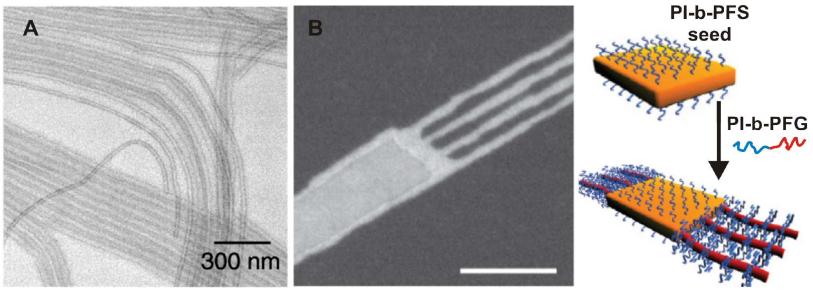

Figure 1.10: (A) TEM micrographs of PFS-*b*-PDMS assemblies formed in *n*-decane at 61^0C where the sample was allowed to age for 1 day at room temperature. (B) Dark-field TEM micrograph and schematic representation and of grown scarf-shaped micelles with PI-*b*-PFG tassels and a PI-*b*-PFS platelet core architectures.

According to this theory, D/l is proportional to σ_l/σ_f. Thus, one can have an anisotropic structure with many folds per chain (with D$\gg$l) when the lateral surface tension σ_l is much larger than the surface tension σ_f associated with the folds.

Self-assembly of semicrystalline block copolymers have attracted attention due to their theoretical interests but also because they provide an opportunity to develop self-assembly strategies for complex nanostructures. Such polymers are for example polyferrocenylsilanes which can be oxidized to a semiconducting state and serve as precursor to magnetic ceramics. Winnik, Manners and co-workers have shown that block copolymers containing a crystallisable polyferrocenyldimethylsilane (PFS) exhibit unique phase behavior in the presence of a nonpolar selective solvent and different micellar architectures can be obtained [20, 21, 22]. They showed that crystallization is the main driving force behind the cylindrical micelles formation of poly (ferrocenyldimethylsilane)-*block*-polydimethylsiloxane (PFDMS-*b*-PDMS) as shown in Fig. 1.10 (A) [23, 24, 25, 26]. This was the first example of cylindrical micelles formed via crystallization- induced self-assembly in a diblock copolymer upon cooling. In addition, a reversible transition was observed from cylindrical micelles to hollow nanotubes by varying block length and solvent composition. This work has demonstrated that the interplay between aggregation and crystallization can lead to a time-dependent reorganization in micellar systems.

Recently, they have shown that by a driven epitaxial crystallization process of PI-*b*-PSF diblock copolymers micellar morphologies as scarf-like with cylinder-cylinder and platelet-cylinder connections are formed (Fig. 1.10 (B)) [27]. The length of the micelles can be controlled by addition of extra PFS block-copolymer unimers to preform micellar seeds due to the high reactivity and nucleation potential of the exposed crystal surfaces leading to a living type extension of the structure.

By changing composition, solvent, and structure of the crystalline block, spherical, cylindrical, and lamellar micelles are observed. Poly(ϵ-caprolactone)-*b*-poly(ethylene oxide) (PCL-*b*-PEO) is another crystalline-coil system. The results show that the morphology of the crystalline coil micelles of PCL-*b*-PEO block copolymers strongly depends on the lengths of both blocks. In this system, the formed micelles are composed of a crystalline PCL core and a soluble PEO corona in aqueous medium. Spherical micelles

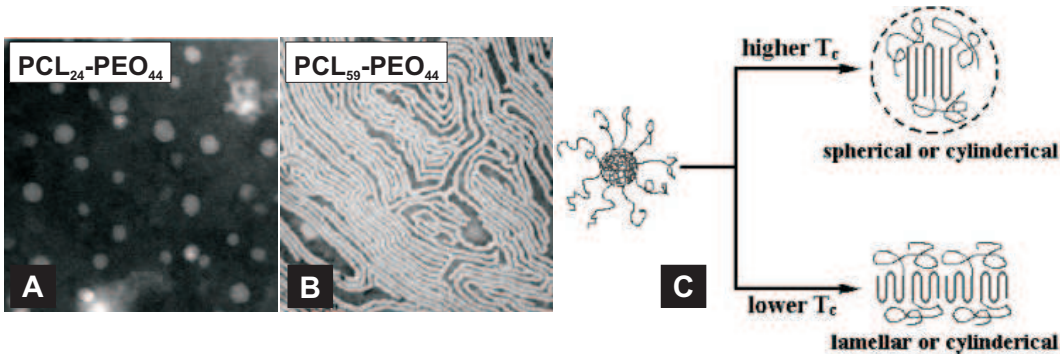

Figure 1.11: TEM images of micelles of PCL_mPEO_{44} block copolymers: (A) spherical micelles of the $PCL_{24}PEO_{44}$ and (B) worm- like micelles of the $PCL_{59}PEO_{44}$ blocks. (C) Schematics for micellar morphologies of PCL_nPEO_{113} at different crystallization temperatures. The subscripts represent the polymerization degrees of the blocks.

are formed at the shortest PCL block, then the micellar morphology turns into cylindrical and worm- like structures as the length of the PCL block increases, whereas lamellar micelles are formed in the longest PCL-*b*-PEO block copolymer (Fig. 1.11 (A) and (B)). The micellar morphologies can be as well regulated by crystallization temperature. At a higher crystallization temperature, the chain-folding number of the crystalline PCL block becomes smaller and the grafting density increases, so spherical or cylindrical micelles with a larger length/ diameter ratio are formed, whereas lamellar and cylindrical micelles with a smaller length/ diameter ratio are formed at a lower crystallization temperature (Fig. 1.11 (C)) [28, 29].

Xu et al. [30] investigated the effect of architecture on the morphology and the crystallization of oxyethylene/oxybutylene (EB) block copolymers from micelles in *n*-hexane. At high temperature the block copolymer form micelles with a E core. Upon cooling, the micelles undergo deformation. The E block becomes more anisotropic and deformation-induced crystallization occurs, which is reflected by a drastic increase in crystallinity. They reported that the B block is highly stretched in shorter block copolymer and this may allow aggregation of the micelles, while the B block is densely packed in the longer block copolymer. In addition, macroaggregates of lamellae were observed [31].

Disk-like micelles formed by crystallization of alkyl chains have also been observed from SAXS/SANS experiments on a PME-*b*-PHOVE oligomer in water, a selective solvent for hydrophilic ether block [32].

As one can see, the micellar morphology of crystalline-coil block copolymers critically depends on the crystallization conditions, such as crystallization temperature, the nature and the lengths of the block copolymers, concentration, the solvent selectivity, etc.

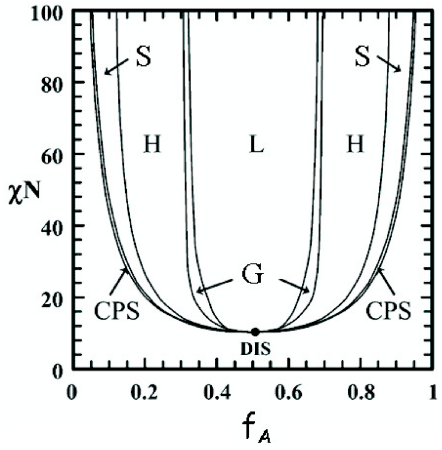

Figure 1.12: The theoretical prediction of the phase diagram of a diblock copolymer (Matsen and Bates, 1996). Labeling of the phases: L (lamellar), G (bicontinuous gyroid), H (hexagonal cylinders), S (spheres), CPS (close-packed, cubically ordered spherical micelles) and Dis (disordered).

1.3 Block Copolymers in Solution: Non-Crystalline Complex Morphologies

As was point out in the previous section the self-assembly of coil-crystalline block copolymers, where the insoluble block can crystallize, the final morphology is controlled by the core crystallization of the micelles. In contrast to coil- crystalline block copolymers the self-assembly of fully amorphous (coil-coil) block copolymers is well understood.

Self- Assembly in Bulk. A lot of research has to be done to understand the relationships between block copolymer architecture and self-assembly in the bulk. Linear diblock copolymers are the best-known class of block copolymers. Due to the covalently bonding between the blocks, they form 10-100 nm -sized microdomain structures with a morphology that is determined by the relative volumes of the blocks [33]. A diblock copolymer with equal block volumes leads to a lamellar morphology, which is a sequence of the layers of the two different blocks. With increasing block volume ratio gyroid, cylindrical, and spherical equilibrium morphologies are formed [34].

The phase behavior of block copolymers is determined by three factors: the degree of polymerization N, the composition f (volume fraction of the A component), and the A-B segment-segment interaction parameter χ, which is the Flory-Huggins parameter.

The Flory-Huggins theory describes the phase separation process from the thermodynamic point of view. It minimizes the unfavorable interaction energy between different molecules to achieve the smallest surface to volume ratio. The Flory-Huggins free energy of mixing at a temperature T, with a degree of polymerization N is given by:

$$\frac{F_{max}}{kT} = lnf_A\frac{f_A}{N} + lnf_B\frac{f_B}{N} + f_Af_B\chi \tag{1.16}$$

The phase diagram of a diblock copolymer is shown in Fig. 1.12, where χN represents

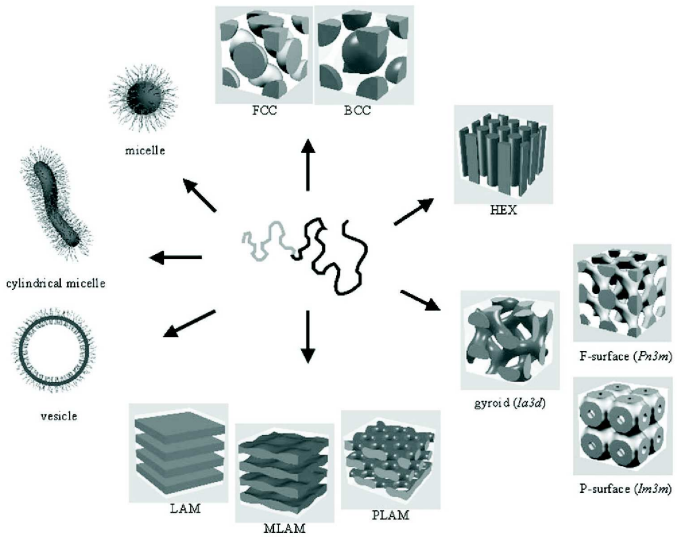

Figure 1.13: Self-organization structures of block copolymers and surfactants: spherical micelles, cylindrical micelles, vesicles, fcc- and bcc-packed spheres (FCC, BCC), hexagonally packed cylinders (HEX), various minimal surfaces (gyroid, F surface, P surface), simple lamellae (LAM), as well as modulated and perforated lamellae (MLAM, PLAM).

the degree of incompatibility between the blocks and f_A is the volume fraction of the A component. If χN $\leq$10 the entropy of mixing dominates, resulting in a disordered phase. If χN$\geq$10, entalpic terms dominate, producing an order -to- disorder transition (ODT), where the unlike segments segregate into a variety of ordered periodic microstructures. The connectivity of the blocks have a strong effect on the phase behavior by changing the ODT temperature compared to the phase separation of a blend of blocks, and on the structure of the boundaries between the ordered phases [35, 36, 37, 38].

Self- Assembly in Solution. Chemical dissimilarity between the A and B blocks often confers an amphiphilic character to this class of materials. Particularly, there is a subset of block copolymers that contain both hydrophilic and hydrophobic blocks, and these compounds can be regarded as macromolecular analogs of conventional small molecule surfactants.

Amphiphilic polymer systems self-assembled in a variety of nanostructures in surfactant solutions ranging from spherical micelles to vesicles. (Fig. 1.13) [39]. Three basic structures can be created in the dilute limit: spheres, cylinders, and bilayers, dictated primarily by the ratio of the sizes of the hydrophobic and hydrophilic parts of the molecule. These basic micellar morphologies can be modeled using simple geometrical concepts that correlate molecular structure with interfacial curvature. Israelachvili and co-workers [40] developed a phenomenological description of the optimal micellar geometry in terms of the packing parameter defined as p=$v/l_0 a$ where v is the volume of the hydrophobic chain, l_0 is the maximum effective length of the hydrophobic chain, and a is the measured interfacial area per chain. The preferred geometries are spheres for $v/l_0 a \leq 1/3$, cylinders for $1/3 \leq v/l_0 a \leq 1/2$, bilayers for $1/1 \leq v/l_0 a \leq 1$ and inverted structures for $v/l_0 a \geq 1$ as shown in Fig. 1.14 [41]. Numerous complex morphologies

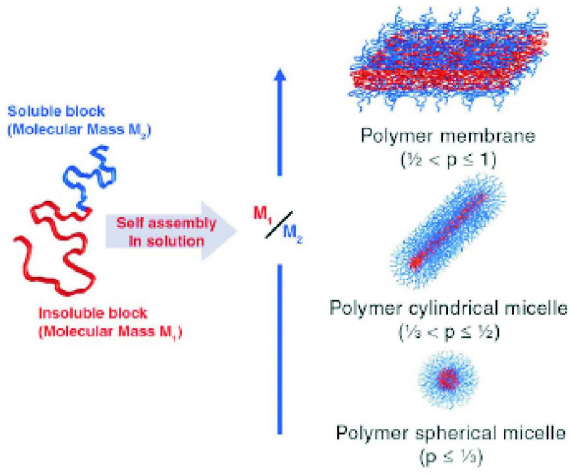

Figure 1.14: Different geometries formed by block copolymers in selective solvent conditions.

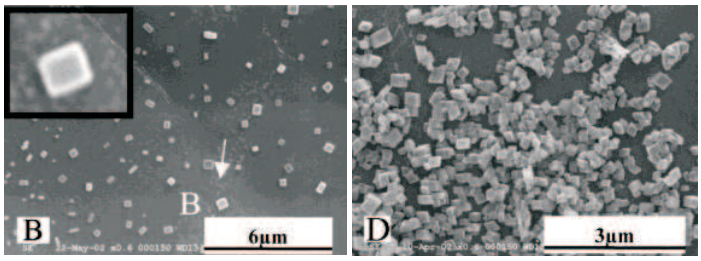

Figure 1.15: SEM image of cubic microparticles formed after solvent evaporation from PS-*b*-PAA micellar solution in water/butanone.

have been observed for block copolymers in dilute solutions, often these are not in equilibrium as a result of the preparation method. This is especially a problem for micelles containing a glassy core (e.g. PS or PMMA).

A variety of morphologies including tubules, vesicles, branched vesicles and large compound vesicles have been observed for PS-*b*-PAA [42] and PS-*b*-PEO [43] diblocks in DMF/ water mixture. Eisenberg et al. dissolved the polymers first in a nonselective solvent, then a precipitant for PS was added. The structures formed may be nonequilibrium morphologies trapped by PS vitrification.

Cubic particles (edge length 200-600 nm) result from the aggregation of PS-*b*-PAA diblock micelles upon evaporation of the aqueous/organic solvent mixture [44]. The micelles formed in aqueous solution, to which one of the several organic solvents was added. The effect is not fully understood. Hydrogen bonding may play a role, and the addition of solvent leads to ternary system. When the organic solvent evaporates, the phase diagram may pass through a cubic micellar phase (Fig. 1.15).

Polymeric surfactants such as poly(butadiene-*b*-ethylene oxide) (PB-*b*-PEO) have been investigated by Bates and coworkers [45]. Giant worm-like micelles formed in dilute aqueous solution by a low molecular weight PB-*b*-PEO block copolymer have been observed

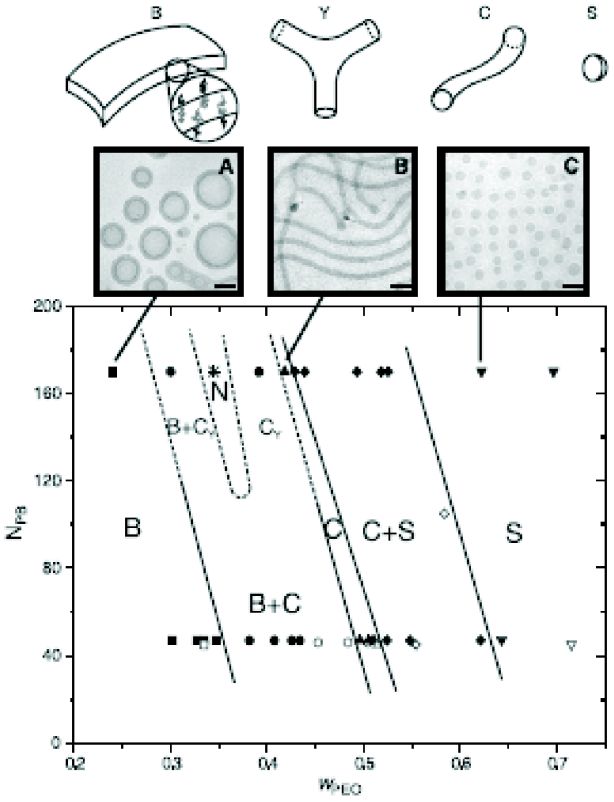

Figure 1.16: Summary of micellar morphologies observed using cryo-TEM with dilute aqueous solutions of PEO-*b*-PB diblock copolymers. The regions of stability for spherical (S), cylindrical (C), branched (C-Y), network(N), and bilayer morphologies are given as functions of the degree of polymerization of the PB block (N_{PB}) and the weight fraction of the PEO block (w_{PEO}).

by TEM and the structure studied in detail by SANS [46, 47]. These elongated micelles successively pack into a nematic and then columnar phase as the polymer concentration is increased [46]. The authors studied the micellar morphology diagram as a function of molecular size and composition, where N_{PB} and w_{PEO} are the degree of polymerization and weight fraction of the PB and PEO blocks, respectively as can be visualized in Fig. 1.16. Additional to the basic structural elements as spheres (S), cylinders (C), and bilayers (B) they discovered intermediate morphologies that assembles in the solution.

Bilayer-to-cylinder and cylinder-to-sphere [48] boundaries were tilted toward lower values of the weight fraction of PEO w_{PEO} as the hydrophobic chain size N_{PB} is increased. Therefore, one could observe a bilayer-to-cylinder or cylinder-to-sphere transition by increasing the overall molecular weight of the surfactant at a fixed PEO weight fraction. This is consistent with the picture that the hydrophilic (corona) chains are normally in a more extended conformation than the hydrophobic (core) chains (Fig. 1.17).

The morphological transition from bilayer to cylinder to sphere is understood to be a

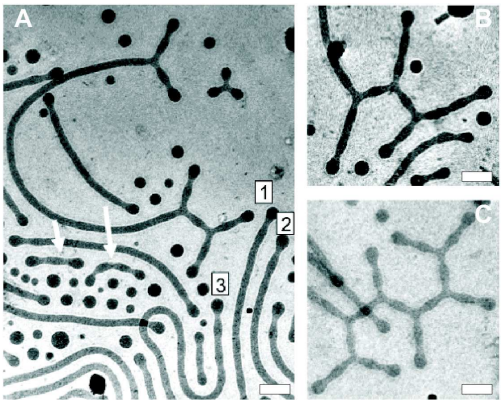

Figure 1.17: Cryo-TEM images from a solution of binary mixture of PEO-*b*-PB diblocks close to the boundary between cylinder and sphere structure. Undulation in the cylindrical micelles with bead-like end caps: (A) short cylinders with one and two undulations. In (B) and (C) the number of undulations in the cylinder branches is quantized according to the distance between branch and end junction. The scale bars indicate 100 nm.

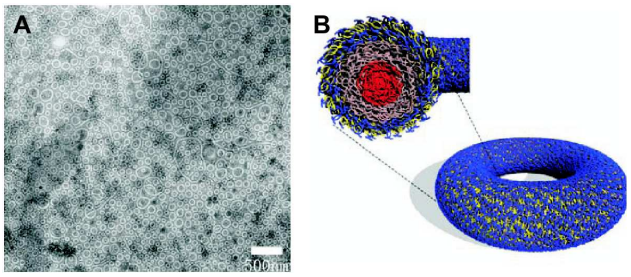

Figure 1.18: Toroidal micelles formed by a PAA-*b*-PMA-*b*-PS triblock in a THF/water mixed solvent with EDDA divalent cations. (A) TEM image of cast film, negatively stained with uranyl acetate. (B) Schematic of toroidal structure showing hydrophobic PS (center) and PMA (inner shell) with a corona of hydrophilic PAA with closely associated EDDA.

result of the increase in the preferred interfacial curvature, which tends to reconcile the increased asymmetry between the excluded volumes of the hydrophilic and hydrophobic segments with increasing hydrophilic composition.

Pochan et al. [49] showed that toroidal structure can self-assemble through the collapse of negatively charged cylindrical micelles, driven by interaction with a divalent organic cation (Fig. 1.18). The micelles were formed by PAA-*b*-PMA-*b*-PS triblocks in THF/water mixtures with the divalent 2,2′-(ethylendioxy) diethylamine.

The divalent nature of the cation was shown to be essential to this process due to condensation in the presence of multivalent ions. It was shown to be necessary to control the ratio of divalent ion to acid, and to prepare the aggregates from a mixed solvent (THF/ water). THF was needed to ensure initial dissolution of the hydrophobic PS core. A range of intermediate structures, with trifunctional branch points as for the

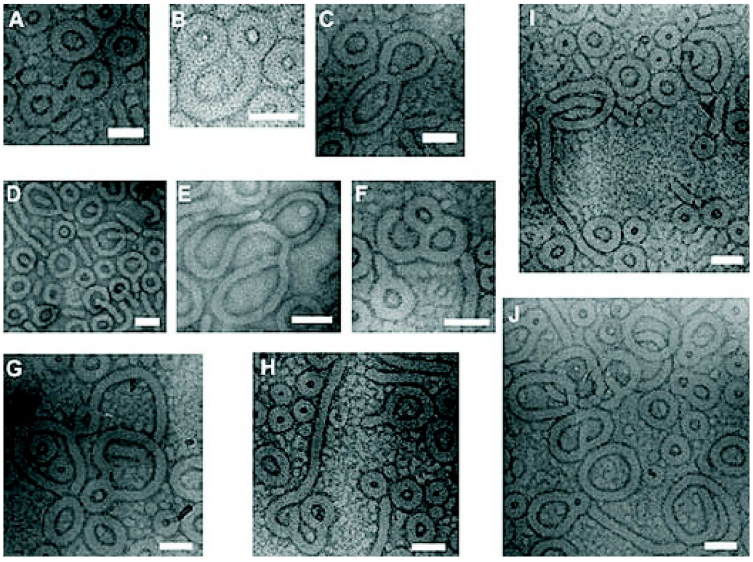

Figure 1.19: TEM images showing intermediate structures formed by casting films from THF/ water+ EDDA solutions of a PAA-*b*-PMA-*b*-PS triblock: (a, b, g) dumb-bells; (e, f, g, i) interior closed rings; (d, f, h) lariats; (c, j)figure eights; (g) and (i) cylinders with end connected but not fused together. The scale bars indicate 100 nm.

aggregates studied by Jain and Bates [48], was noted (Fig. 1.19).

1.4 Aim of the thesis

The results described in this thesis were obtained on the poly(butadiene)-*b*-poly(ethylene oxide)(PB-*b*-PEO) semicrystalline block copolymers, where the length of the blocks were varied.

This study aims at understanding the kinetically controlled crystallization of block copolymer micelles in a selective solvent (*n*-heptane), and targets the development of morphologies with new architecture without changing the chemistry.

Through a thermally controlled crystallization of the PEO blocks, we are able to obtain a large variety of micellar morphologies. The interplay between the crystallization of the PEO block and the self-assembly behavior, as a function of the molecular composition of the block copolymers is one key element of this thesis.

Bibliography

[1] K. H. Storks. *J. Am. Chem. Soc*, 60:1753–1761, 1938.

[2] A. Keller. *Phil. Mag.*, 2:1171–1175, 1957.

[3] J. I. Jr. Lauritzen and J. D. Hoffman. *J.Appl.Phys.*, 44:4340–4352, 1973.

[4] D. M. Sadler and G. H. Gilmer. *Phys Rev Lett*, 56:2780, 1986.

[5] D.M. Sadler. *Polymer*, 24:1401, 1983.

[6] D.M. Sadler and G. H. Gilmer. *Polymer*, 25:1446, 1984.

[7] H. D. Keith and F. J. Padden. *J. Appl. Phys.*, 35:1270–1285, 1964.

[8] D.C. Bassett and R.H. Olley. *Polymer*, 25:935, 1984.

[9] H.D. Keith and F.J. Jr. Padden. *Polymer*, 25:28, 1984.

[10] A. J. Pennnings and A. M. Kiel. *Kolloid Z. Z. Polym.*, 205:106, 1965.

[11] A. M. Pennnings, A. J. Pennnings, J. M. A. A. Van der Mark, and A. M. Kiel. *Kolloid Z. Z. Polym.*, 237:336, 1970.

[12] P. G. De Gennes. *J. Chem. Phys.*, 60:5030–5042, 1970.

[13] A. Kelarakis, K. Yoon, I. Sics, R. H. Somani, X. M. Chen, B. S. Hsiao, and B. Chu. *J. Macromol. Sci. Phys.*, 45:247–261, 2006.

[14] B. Lotz and A. J. Kovacs. *Kolloid Z. Z. Polym.*, 209:97–114, 1966.

[15] B. Lotz, A. J. Kovacs, G. A. Bassett, and A. Keller. *Kolloid Z. Z. Polym.*, 209:115–128, 1966.

[16] A. P. Gast, P. K. Vinson, and K. A. Coganfarinas. *Macromolecules*, 26:1774–1776, 1993.

[17] K. A. Cogan and A. P. Gast. *Macromolecules*, 23:745–753, 1990.

[18] E. K. Lin and A. P. Gast. *Macromolecules*, 29:4432–4441, 1996.

[19] T. Vilgis and A. Halperin. *Macromolecules*, 24:2090–2095, 1991.

[20] J. Raez, J. P. Tomba, I. Manners, and M. A. Winnik. *J. Am. Chem. Soc.*, 125:9546–9547, 2003.

[21] J. Raez, I. Manners, and M. A. Winnik. *Langmuir*, 18:7229–7239, 2002.

[22] X. Wang, H. Wang, D. J. Frankowski, P. G. Lam, P. M. Welch, Winnik M. A., J. Hartmann, Manners I., and R. J. Spontak. *Adv. Mater.*, 19:2279–2285, 2007.

[23] J. Raez, R. Barjovanu, J. A. Massey, M. A. Winnik, and I. Manners. *Angew. Chem. Int. Ed.*, 39:3862–3865, 2000.

[24] G. Guerin, J. Raez, I. Manners, and M. A. Winnik. *Macromolecules*, 38:7819–7827, 2005.

[25] I. Korczagin, M. A. Hempenius, R. G. Fokkink, M. A. C. Stuart, M. Al-Hussein, P. H. H. Bomans, P. M. Frederik, and G. J. Vancso. *Macromolecules*, 39:2306–2315, 2006.

[26] L. Shen, H. Wang, G. Guerin, C. Wu, I. Manners, and M. A. Winnik. *Macromolecules*, 41:4380–4389, 2008.

[27] T. Gädt, N. S. Ieong, G. Cambridge, Winnik M. A., and Manners I. *Nat. Mater.*, 8:144–150, 2009.

[28] Z. X. Du, J. T. Xu, and Z. Q. Fan. *Macromol. Rapid Commun.*, 29:467–471, 2008.

[29] Z. X. Du, J. T. Xu, and Z. Q. Fan. *Macromolecules*, 40:7633–7637, 2007.

[30] J. T. Xu, J. P. A. Fairclough, S. M. Mai, and A. J. Ryan. *J. Mater. Chem.*, 13:2740–2748, 2003.

[31] D. Richter, D. Schneiders, M. Monkenbusch, L. Willner, L. J. Fetters, J. S. Huang, M. Lin, K. Mortensen, and B. Farago. *Macromolecules*, 30:1053–1068, 1997.

[32] M. Nakano, K. Matsumoto, H. Matsuoka, and H. Yamaoka. *Macromolecules*, 32:4023–4029, 1999.

[33] F. S. Bates and G. H. Fredrickson. *Annu. Rev. Phys. Chem.*, 41:525557, 1990.

[34] M. W. Matsen and F. S. Bates. *Macromolecules*, 29:1091–1098, 1996.

[35] M. Olvera de la Cruz and I. C. Sanchez. *Macromolecules*, 19:2501 – 2508, 1996.

[36] G. Floudas, N. Hadjichristidis, H. Iatrou, T. Pakula, and E. W. Fisher. *Macromolecules*, 27:7735–7746, 1994.

[37] G. Floudas, S. Pispas, N. Hadjichristidis, T. Pakula, and I. Erukhimovich. *Macromolecules*, 29:4142–4154, 1996.

[38] G. Floudas, N. Hadjichristidis, N. Tselikas, and I. Erukhimovich. *Macromolecules*, 30:3090–3096, 1997.

[39] S. Förster and T. Plantenberg. *Angew. Chem. Int. Ed.*, 41:688–714, 2002.

[40] J. N. Israelachvili. *Intermolecular and Surface Forces*. Academic Press San Diego, 2nd edition.

[41] T. Smart, H. Lomas, M. Massignani, M. V. Flores-Merino, L. Ruiz Perez, and BattagliaG. *Nanotoday*, 3:38–46, 2008.

[42] L. Zhang and A. Eisenberg. *Macromolecules*, 32:2239–2249, 1999.

[43] K. Yu and A. Eisenberg. *Macromolecules*, 31:3509–3518, 1998.

[44] W. Zhang, L. Shi, Y. An, X. Shen, Y. Guo, L. Gao, Z. Liu, and B. He. *Langmuir*, 19:36026–6031, 2003.

[45] S. Jain and F. S. Bates. *Science*, 300:460–464, 2003.

[46] Y. Y. Won, H. T. Davis, and F. S. Bates. *Science*, 283:960–963, 1999.

[47] Y. Y. Won, H. T. Davis, F. S. Bates, M. Agamalian, and G. D. Wignall. *J. Phys. Chem. B*, 104:7134–7143, 2000.

[48] S. Jain and F. S. Bates. *Macromolecules*, 37:1511–1523, 2004.

[49] D. J. Pochan, Z. Chen, H. Cui, K. Hales, K. Qi, and K. L. Wooley. *Science*, 306:94–97, 2004.

CHAPTER 2

Overview of the thesis

This work aims to provide new approaches for studying crystal formation of block copolymers in a selective solvent. Various crystalline morphologies of poly(butadiene)-*b*-poly (ethylene oxide) (PB-*b*-PEO) were investigated in *n*-heptane. *n*-Heptane is a good solvent for the PB block and a poor solvent for the crystallizable PEO block. Above the melting temperature of the PEO block at 70^oC, micelles containing a molten PEO core and a soluble PB corona are observed. The micellar morphology diagram as a function of the crystallization temperature and molecular composition of the block copolymers was studied. It has been found that, the competition between the PEO core crystallization and the self-assembly behavior, is the driving force that dictates the morphological development.

This thesis consists of six chapters including four publications which are presented in Chapters 3 to 6.

Special attention was drawn in the case of a symmetric PB-*b*-PEO block copolymer. The polymer solutions were kept at 70^0C for 30 min, in order to erase any thermal history, and then quenched via two thermal pathways. A fast quenching into liquid nitrogen results in the formation of crystalline micelles retaining the spherical shape present in the molten state at 70^0C. If crystallization took place at 30^0C, a meander-like structure was formed. The description of this new morphology including the study of the crystallization kinetics is summarized in Chapter 3.

Chapter 4 extends the previous analysis to a detailed investigation of the crystallization and aggregation behavior of the symmetric PB-*b*-PEO block copolymer in *n*-heptane. At low crystallization temperatures, $T_c \leq 30^0C$, the high nucleation rate of the PEO core dictates the growth of the crystals by a fast aggregation of the micelles into meander-like (branched) structures, whereas at $T_c > 30^0C$, the nucleation rate is diminished and a slow growth rate, i.e., no depletion of micelles occurred at the crystal

growth front, leads to the formation of twisted lamellae.

In the case of a highly asymmetric PB-*b*-PEO block copolymer spherical crystalline micelles formed at -30^0C. However, the quenching in liquid nitrogen leads to rod-like micelles formation. The decrease of solvent quality for the PB-corona chains at very low temperatures leads to this transition from spheres to rods. The rod-like micelles are metastable in solution and self-assemble into needle-like morphology as described in Chapter 5.

To conclude, various self-assembled morphologies of the PB-*b*-PEO block copolymer were summarized in the form of a morphological phase diagram in Chapter 6. The morphologies are controlled by the crystallization temperature and the length of the constituting blocks. The presented approach opens an alternative way for developing crystalline nanostructures of varying shape, i.e. spheres, cylinders (rods, worms, twisted cylinders) and lamellae (meanders, twist lamellae, platelets or dendrites).

In the following, an overview of the main results is presented.

2.1 Switching of the PB-b-PEO Micellar Crystalline Morphology

The effect of crystallization on the self-assembled micellar morphologies of the symmetric $B_{52}EO_{48}$ block copolymer in *n*-heptane was studied. The subscripts denote the mass fraction in percent. At 70^0C, the block copolymer self-assembles into spherical micelles composed of a liquid PEO core and a soluble PB corona. The micellar morphologies discussed here have been generated from the hot solution (70^0C) via two pathways: (A) by direct immersion into liquid nitrogen and (B) by quenching to 30^{o}C, i.e., the crystallization temperature of the PEO block.

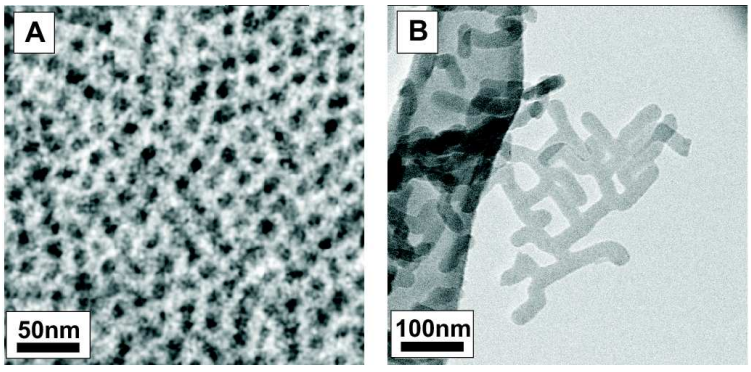

Figure 2.1: In situ freeze- drying Cryo -TEM micrographs of crystalline structures formed by $B_{52}EO_{48}$ in *n*-heptane: (A) spherical micelles obtained from pathway A, after quenching in liquid nitrogen ; (B) meander-like obtained from pathway B, after quenching at 30^{o}C.

At low crystallization temperatures (pathway A), the liquid PEO-block crystallizes

within the cores of the spherical micelles and the melt morphology is retained (Fig. 2.1 A). The darker cores correspond to the PEO block (higher electron density) embedded in the PB matrix (lower electron density). The spherical objects appeared to be monodisperse in size with a mean core radius of 13 nm. DLS reveal an R_H of 18 nm. The WAXS analysis confirmed that homogeneous nucleation takes place within each individual spherical microdomain, i.e, kinetics are determined by nucleation.

Pathway B leads to the formation of an novel micellar morphology as meander-like structure (Fig. 2.1 B). The PEO core structure resembles a ribbon-like or rectangular prismatic structure having ellipsoidal endings. This morphology exhibits lateral growth and forms simultaneously two or four new branches of equivalent width ranging from 20 to 35 nm. The meanders development in the solution was investigated by time - resolved WAXS and dynamic light scattering (DLS). Both techniques indicated that the growth of the meanders starts around a micellar structure in which nucleation has taken place. Further micelles will aggregate and immediately become crystalline upon merging with the primary nucleus. The formation of the meander-type structure is a 2D growth process combined with a breakout crystallization of the melt morphology. The crystallinity within the meanders increased to 27%, whereas, in the case of the spherical micelles the crystallinity reached just 22%. All data demonstrated that the meander-like structure is formed via a crystallization-induced aggregation of spherical micelles upon cooling.

2.2 Influence of Crystallization Kinetics on Morphology

In this study, we discuss the effect of crystallization kinetics on the formed morphology upon crystallization-induced aggregation of spherical micelles of a symmetric poly(1,2-butadiene)-*block*-poly(ethylene oxide) diblock copolymer ($B_{52}EO_{48}^{5.6}$). The polymer solutions were first kept at 70^0C for 20 min and then quenched to different crystallization temperatures for two hours. At 70^0C, DLS revealed the presence of spherical micelles with a molten PEO core and a hydrodynamic radius R_H of 12 nm.

The size evolution of the aggregates and the kinetics at different crystallization temperatures (T_c) was monitored by static (SLS) and dynamic light scattering (DLS). Evidence on the crystallization/melting temperatures in solution were supported by differential scanning calorimetry (DSC). The combination of the various techniques indicated that the final morphology is directly controlled by T_c: meander-like structures formed at low T_c, whereas higher T_c lead to twist lamellae formation.

Fig. 2.2 displays the evolution with time of the normalized hydrodynamic radius (R_H/R_0) upon quenching the hot solution from 70^0C to different T_c. The R_H retained a constant value of 12 nm when the solution was quenched to 35^0C or higher temperatures. At temperatures below 35 ^0C crystallization takes place in the micellar PEO core as monitored by the increase of R_H, indicating rearrangement of micelles and growth into larger structures (Fig. 2.2). R_H strongly depends on T_c, i.e., R_H decreases with decreasing T_c, from 195 nm at T_c= 34 ^0C to 85 nm at T_c= 20 ^0C, respectively (Fig. 2.3)

A low induction time of the crystallization process was recorded at $T_c \leq 30^0C$ (only

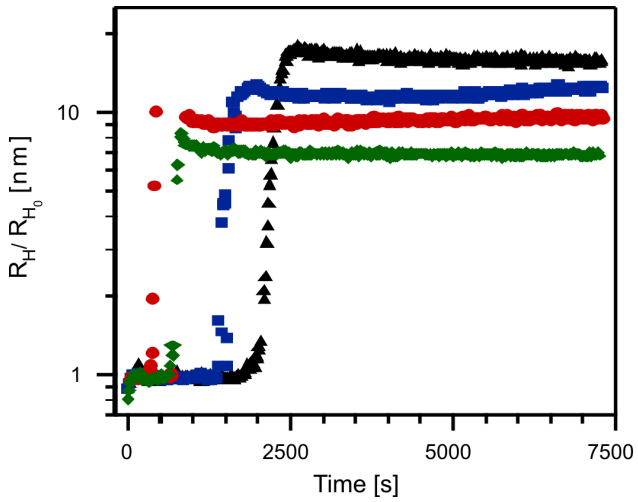

Figure 2.2: Evolution of the normalized hydrodynamic radius R_H/R_0 of 0.1wt% solution of $B_{52}EO_{48}$ in *n*-heptane first equilibrated at 70^0C and then immersed directly into the vat of the light scattering apparatus to 34^0C (black $\triangle$), 32^0C (blue $\square$), 30^0C (red $\circ$) and 20^0C (green $\diamond$), respectively.

few seconds), whereas at $T_c > 30^0C$, it was delayed with 30 min at $T_c = 34\ ^0C$ (Fig. 2.3). The lowest induction time (400 s) was observed at 30^0C, where the maximum crystallization exotherm is located in solution. Moreover, T_c affects the aggregation time of the micelles, that is, the time until a stable R_H plateau is reached, after the onset of crystallization. The lowest aggregation time was observed at $T_c \leq 30^0C$, whereas at $T_c > 30^0C$, the aggregation time was higher (Fig. 2.2).

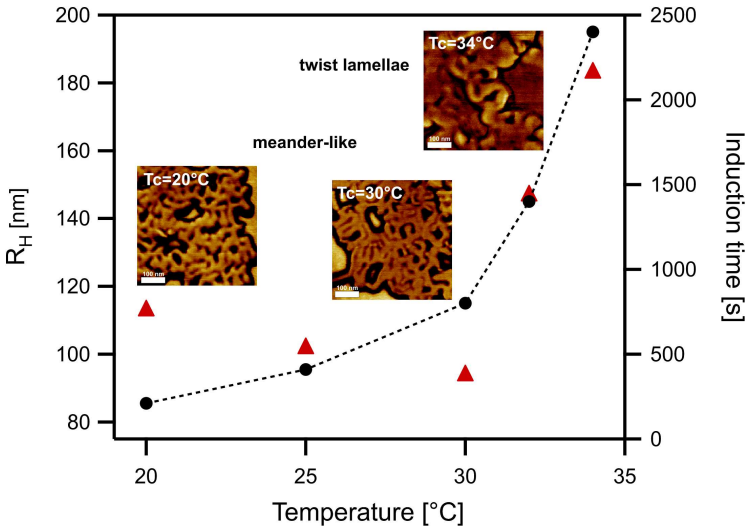

Figure 2.3: Dependence on the crystallization temperature of the crystal size (black $\circ$) and of the induction time of the primary nucleation process (red $\triangle$). The SFM images of 0.1wt% solution of $B_{52}EO_{48}$ in *n*-heptane indicates the crystalline morphologies formed after quenching to 20^0C, 30^0C: meander-like structures, and to 34^0C: twist lamellae.

The above results suggest the presence of two types of mechanism where the crystal growth proceeds in different manners. At $T_c \leq 30^0C$, crystallization induced a high nucleation rate in the solution on a narrow time scale. Subsequently, fast aggregation of adjacent micellar neighbors and fast advancing of the crystallization front in the solution leads to fast depletion of micelles at the growing front. Herein, the crystallization front, therefore the nucleation and growth process, propagates very fast in the solution.

At $T_c > 30^0C$, the nucleation rate is lower and only few nuclei formed at the same time in the solution. Due to the reduced number of nuclei/time the growth process is slow and no depletion of micelles occurred at the crystal growth front, as a gradual development of R_H to a stable value was observed (Fig. 2.2). Here, the growth process has obviously become the step that determines the crystal pattern rather than the nucleation process. It is interesting to note that the crystal morphology changed from meanders (branched lamellae) to twist lamellae at $T_c > 30^0C$ (Fig. 2.3). All data demonstrate that the formation mechanism of the crystals through micellar aggregation is dictated by two competitive effects, namely, by the nucleation and growth of the PEO core.

2.3 Sphere-to-Rod-like Transition of Crystalline Micelles

The crystallization behavior of a highly asymmetric $B_{88}EO_{12}$ block copolymer in *n*-heptane was investigated. The PB block is the larger component, longer than the crystalline PEO block by a factor of 7. The subscripts denote the mass fraction in percent.

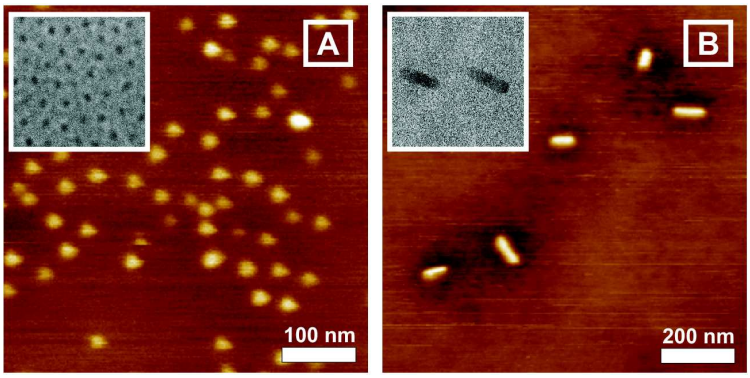

Figure 2.4: SFM phase contrast images of 0.1wt% solution of $B_{88}EO_{12}$ in *n*-heptane showing the morphologies formed by (A) quenching to -30^0C which leads to spherical micelles (pathway A) and (B) by quenching into liquid nitrogen leading to rod-like micelles (pathway B). The two insets represent the TEM micrographs of the two morphologies. The scales bares of the micrographs are identical with the ones of the corresponding SFM images. The SFM phase contrast images have a resolution of 256 x 256.

When crystallization took place at -30^0C, it induced the formation of crystalline micelles that retained the spherical shape present in the molten state at 70^0C (pathway A: Fig 2.4(A)). DLS confirmed the presence of spherical micelles with a molten PEO

core at 70^0C. The solution was maintained for 24 hours at -30^0C to reach the maximum crystallinity. The crystalline micelles are stable even after 6 months.

Quenching of the hot solution (70^0C) into liquid nitrogen, that is, pathway B emphasized a transition from spheres to rod-like micelles (Fig 2.4(B)). If at -30^0C, *n*-heptane is a good solvent for the PB block, at much lower temperatures it finally becomes a poor solvent. The PB chain of the corona micelles will shrink and occupy less space on the surface of the PEO-cores. Consequently, the spherical micelles become unstable and rearrange into morphologies with smaller curvatures, i.e., rod-like micelles. After the PEO block crystallization the core of the micelles become rigid. The freezing point of *n*-heptane is at -90.6^0C and once the solvent is frozen no further rearrangement of the micelles can occur. The conformational changes must occur between -30 and -90^0C in the solution. Thus the rod-like structure is fixed by crystallization and the rod-like shape is therefore preserved when the solution is warmed up to ambient temperature.

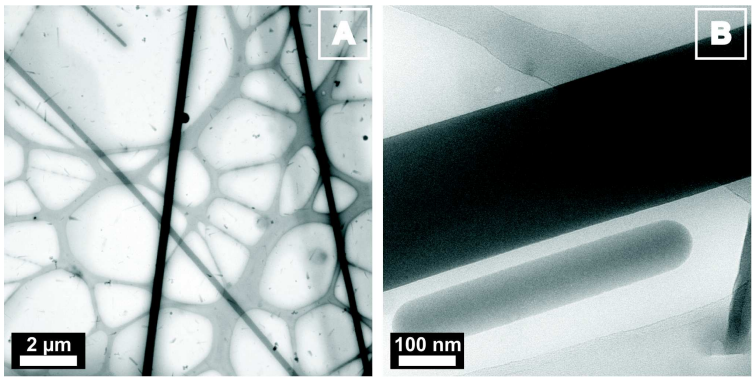

Figure 2.5: Self- assembly of the rod-like micelles to needles after two weeks at room temperature. (A) and (B) present the Cryogenic TEM (cryo-TEM) images of the needle-like morphology and rod-like micelles developed in solution.

The rod-like micelles aggregate and rearrange with time at room temperature and a transition to needle-like morphology occurs in solution. The needles with lengths up to 30 μm and width ranging from 50 to 550 nm are displayed in the cryo-TEM image obtained from 1wt% solution (Fig 2.5 (A)). Fig 2.5 (B) taken at higher magnification provides closer insights of the needle-like and rod-like structure.

The low PEO crystallinity of the rods is responsible for the rearrangements and re-crystallization at room temperature. The rapid morphological transition from spherical to rod-like micelles leaves some PEO exposed in the rods as compared to the much better crystallized spherical micelles. Thus, the rods have a stronger tendency to thicken and recrystallize leading to more stable structures, i.e., needle-like structures.

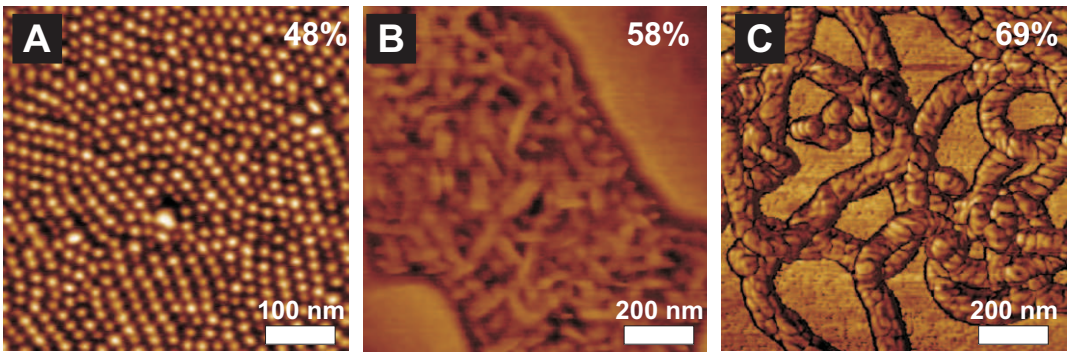

Figure 2.6: Pathway A: SFM phase contrast images of crystalline micellar morphologies formed in *n*-heptane after immersion into liquid nitrogen of the 0.1 wt% polymer solutions from 70^0C: (A) spherical micelles; (B) worm-like micelles and (C) twisted cylinders. The weight fraction of the PEO block is indicated for guidance.

2.4 Phase Diagram of Crystalline Micelles in Selective Solvent

We have investigated the crystalline morphological diagram of the poly(butadiene)-*b*-poly(ethylene oxide)(PB-*b*-PEO) diblock copolymer with various molecular weights and blocks ratio in a selective solvent (*n*-heptane) following two thermal pathways. SFM and TEM enabled imaging of the dried polymer morphologies, whereas the hydrodynamic radii of the micelles in solution were investigated by dynamic light scattering (DLS). The crystallization of the PEO core was confirmed by selected area electron diffraction (SAED) and X-ray diffraction (XRD).

Pathway A, that is, undercooling of the hot solution from selective solvent condition (70^oC in *n*-heptane) into liquid nitrogen, allowed morphological transitions from spheres to rods, worms or twisted cylinders with the increase of the crystalline content of the PEO core (Fig 2.6). Here, *n*-heptane becomes a poor solvent for both blocks at very low temperatures. In this case, the micellar shape present in the molten state at 70^0C is retained after a fast quenching into liquid nitrogen. TEM investigations allowed imaging of the micellar core, after staining the samples with osmium tetroxide to improve the contrast of the PB coronar chains. The aggregation number of the spherical micelles is affected by the weight fraction and crystallinity of the PEO block, that is, the aggregation number increased with the weight fraction of the PEO block, whereas the surface area per chain decreased.

Meanwhile the morphologies generated via the pathway B, that is, by quenching of the hot solutions (70^oC) to the crystallization temperature of the PEO blocks, varied from spheres, cylinders, lamellae, platelets and dendrites structures with the increases of the PEO block length (Fig 2.7). Moreover, an increase of the chain folding number was observed at a high PEO composition, which in turn reduced the lamellar thickness of the crystals. In this pathway *n*-heptane is a poor solvent only for the PEO block.

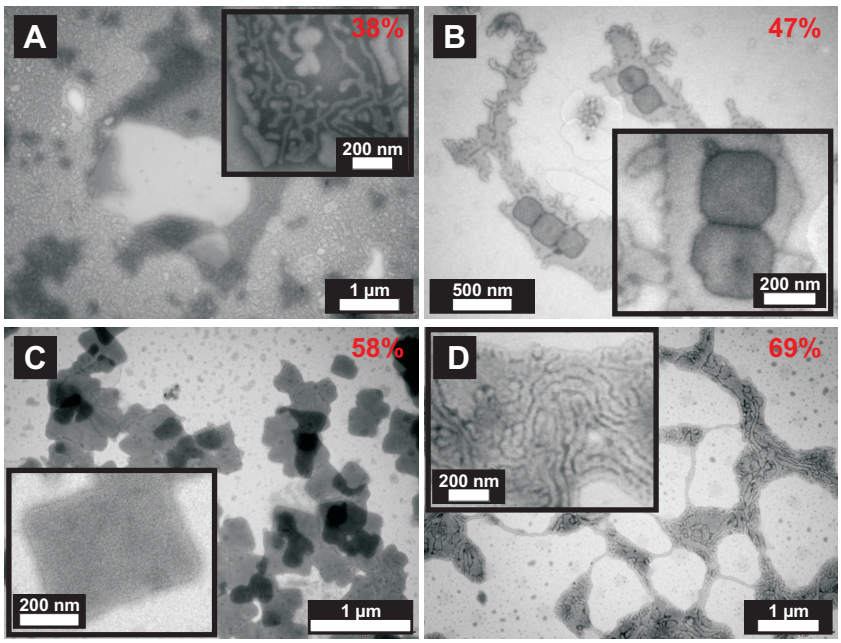

Figure 2.7: Pathway B: TEM micrographs of the crystalline micellar morphologies formed at the crystallization temperature of the PEO block: (A) coexistence of cylinders and platelets; (B)coexistence of lamellae and platelets; (C) platelets; (D) dendrites. Osmium tetroxide was used as a staining agent to improve the PB block contrast. The weight fraction of the PEO block is indicated for guidance.

Fig 2.8 summarizes the diagram of the PB-*b*-PEO crystalline morphologies in *n*-heptane as a function of molecular size and composition, where N_{PEO} and w_{PB} are the degree of polymerization and weight fraction of the PEO and PB blocks, respectively. This representation describes the tendency of the micelles (present in the molten state at 70^0C) to reorganizes at different crystallization conditions.

As crystallization takes place at low temperatures (pathway A), the spherical morphology is mostly retained at PB block compositions above ≥ 0.52. At the crystallization temperature of the PEO block (pathway B), after w_{PB}= 0.68 a transition from the spherical morphology of the melt to lamellar morphologies occurred. Decreasing the size of the PB block below 42%, retained the worm-like micelles in liquid nitrogen, whereas pathway B leads to larger morphologies formation as platelets or dendrites.

At equal composition of the PEO and PB block, crystallization induced aggregation of the spherical units of the melt, favoring the development of branched lamellae (BL), platelets (P), or lamellae and platelets (L + P). On exception occurred at w_{PB}= 0.88, where rod- like micelles formed via pathway A, whereas pathway B retained the spherical shape present in the molten state.

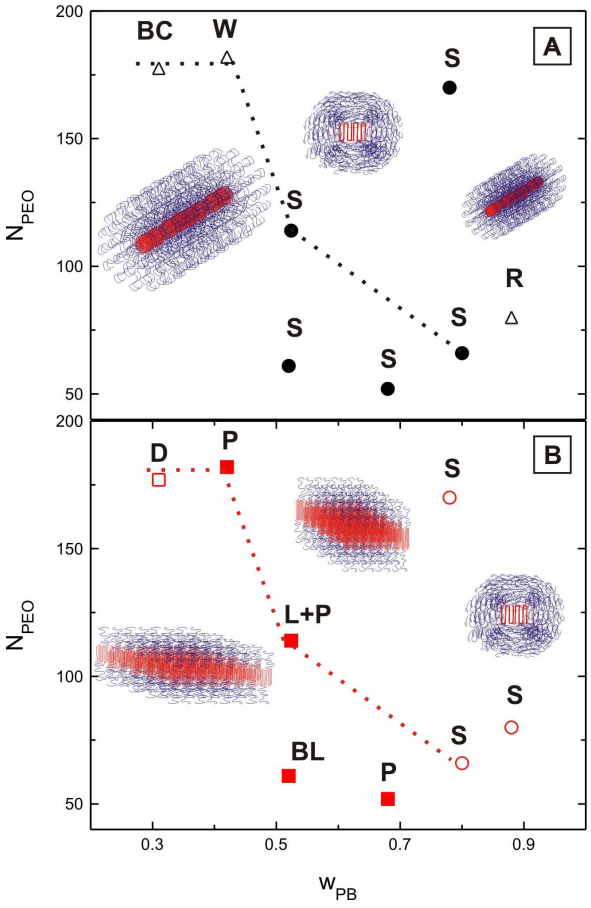

Figure 2.8: Crystalline morphology diagram of PB-*b*-PEO block copolymer in *n*-heptane as a function of molecular size and composition, where N_{PEO} and w_{PB} are the degree of polymerization and weight fraction of the PEO and PB blocks, respectively. Two basic morphologies- spheres (S) and cylinders (referred as rods (R), worms (W) and twisted cylinders (BC)) formed by immersion into liquid nitrogen, pathway A (Top graph). As a decreasing of the PB block composition, at the crystallization temperature of the PEO block (pathway B, bottom graph) spheres (S), lamellae (L) or branched lamellae (BL), platelets (P) and dendrites (D) formed in the solutions. Mixed population of lamellae + platelets (L + P) was observed at w_{PB}= 0.53. The dashed lines establish the morphological trend of the PB-*b*-PEO block copolymers at similar molecular weights, M_n.

The presented approach hereby provides a straightforward way to control the micellar morphology through the choice of the block copolymers and through the thermally controlled crystallization.

2.5 Individual Contributions to Joint Publications

The results presented in this thesis were obtained in collaboration with others, and have been published or will be submitted to publication as indicated below. In the following, the contributions of all the coauthors to the different publications are specified. The asterisk denotes the corresponding author.

Chapter 3

This work is published in *Soft Matter* (**2009**, 5, 208) under the title:

Crystallization-induced switching of the morphology of poly(ethylene oxide)-*block*-polybutadiene micelles

by Adriana M. Mihut, Arnaud Chiche, Markus Drechsler, Holger Schmalz*, Emanuela Di Cola, Georg Krausch and Matthias Ballauff*

I conducted all experiments, evaluated the data and wrote the publication.

Exceptions are stated in the following:

Markus Drechsler performed some cryo-TEM measurements.

Arnaud Chiche helped during the WAXS measurements at the ESRF synchrotron in Grenoble and was involved in the scientific discussion.

Emanuela Di Cola helped during the WAXS experiments at ESRF as a local contact.

Holger Schmalz performed the anionic polymerization of the PB-*b*-PEO block copolymer and was involved in the scientific discussion and corrections of this manuscript.

Georg Krausch and Matthias Ballauff were involved in the scientific discussion and corrections of this manuscript.

Chapter 4

This work is published in *Colloid. Polym. Sci.* (**2009**, DOI 10.1007/s00396-010-2185-y) under the title:

Crystallization-Induced Aggregation of Block Copolymer Micelles: Influence of Crystallization Kinetics on Morphology

by Adriana M. Mihut, Jérôme J. Crassous, Holger Schmalz* and Matthias Ballauff*

I conducted all experiments, evaluated the data and wrote the publication.

Exceptions are stated in the following:

Jérôme J. Crassous was involved in scientific discussion and helped to performed the DLS measurements.

Holger Schmalz performed the anionic polymerization of the PB-*b*-PEO block copolymer.
Holger Schmalz and Matthias Ballauff were involved in the scientific discussion and corrections of this manuscript.

Chapter 5

This work is published in *Macromol. Rapid Commun.* (**2009**, DOI 10.1002/marc.200900571) under the title:

Sphere-to-Rod Transition of Micelles formed by the Semicrystalline Poly (butadiene)-*b*-Poly(ethylene oxide) Block Copolymer in a Selective Solvent

by Adriana M. Mihut, Markus Drechsler, Michael Möller and Matthias Ballauff*

I conducted the SFM measurements, evaluated the data and wrote the publication.

Exceptions are stated in the following:

Markus Drechsler performed the cryo-TEM and SAED measurements.
Michael Möller performed the XRD measurements.
Matthias Ballauff was involved in the scientific discussion and corrections of this manuscript.

Chapter 6

This work will be submitted under the title:

Block Copolymers Assembly in Solution via Kinetic Crystallization Control: Morphological Phase Diagram

by Adriana M. Mihut, Jérôme J. Crassous, Holger Schmalz, Markus Drechsler and Matthias Ballauff*

I conducted all experiments, evaluated the data and wrote the publication.

Exceptions are stated in the following:

Markus Drechsler performed the cryo-TEM and SAED measurements.
Michael Möller performed the XRD measurements.
Holger Schmalz performed the anionic polymerization of the symmetric PB-*b*-PEO block copolymer.
Jérôme J. Crassous and Matthias Ballauff were involved in the scientific discussion and corrections of this manuscript.

CHAPTER 3

Crystallization-Induced Switching of the Morphology of Poly(ethylene oxide)-*block*-Polybutadiene Micelles

Abstract
We study the morphology of micelles formed by a well-defined poly (1, 2-butadiene)-*block*-poly(ethylene oxide) diblock copolymer (PB-*b*-PEO). Dissolved in *n*-heptane at 70^0C, that is, above the melting point of PEO, spherical micelles are formed due to the selectivity of the solvent for the PB-block. If the solutions are cooled down to low temperatures, the liquid PEO-block crystallizes within the cores of the spherical micelles that remain stable. If, however, the solutions are quenched to 30^0C, the spherical micelles aggregate to a novel meander-like structure within several minutes. In its final state, the meander-like super-structure is crystalline as revealed by time-resolved wide-angle X-ray scattering. The super-structure is shown to result from crystallization induced aggregation of spherical micelles. Moreover, crystallization leads to well-defined angles between subsequent aggregating units. A quantitative Avrami-type analysis of the crystallization kinetics demonstrates that the formation of the meander-type structure resembles a 2D growth process combined with a breakout crystallization, showing an Avrami-exponent of 2.5. In opposite to this, crystallization at low temperatures resembles a confined crystallization with a low Avrami-exponent of 0.7. All data demonstrate that the morphology of block copolymers having a crystallizable block can be switched by the competition of aggregation and crystallization.

The results of this chapter have been published as:

Crystallization-induced switching of the morphology of poly(ethylene oxide)-block-polybutadiene micelles
by Adriana M. Mihut, Arnaud Chiche, Markus Drechsler, Holger Schmalz, Emanuela Di Cola, Georg Krausch and Matthias Ballauff, *Soft Matter*, **2009**, 5, 208.

3.1 Introduction

Amphiphilic block copolymers can assemble to micellar structures that extend over many length scales. Hence, amphiphilic block copolymers can self-assemble in selective solvents for one block to form well-defined micellar structures such as spheres [1, 2], cylinders [3], or more complex architectures [4, 5, 6, 7, 8, 9, 10, 11, 12]. The interest in these types of materials is largely stimulated by their potential in various applications from nanotechnology [4, 13] to drug delivery systems [14]. It has been shown that specific morphologies can be controlled through the selection of the monomer, the adjustment of the chain length and architecture [5, 15, 16, 17], temperature [18], and through solution conditions [2, 7, 19, 20, 21, 22] (quality of the solvent, pH, and salinity).

Control of the self-assembly of block copolymers can also be achieved by crystallization of block copolymers when the insoluble block is able to crystallize. While crystallization of polymers and block copolymers has been intensively studied in good solvents [23, 24] or in bulk [25, 26, 27, 28], less work has been done for crystalline block copolymers in selective solvents for the amorphous block. Lotz and Kovacs [23, 24] have been the first to study the morphology of polystyrene -*block*-poly(ethylene oxide) block copolymers crystallized from solution. Square platelets with crystalline regions having the same structures as PEO homopolymers were observed. Gast and coworkers [29, 30] obtained large stable crystalline lamellae of polystyrene-*block*-poly(ethylene oxide) (PS-*b*-PEO) in cyclopentane. They have also shown that the PEO crystallization and the resulting shaped lamellae can be switched off by the addition of a small amount of water that swells the PEO block, and results in spherical micelles with an amorphous core. Richter et al. [31] and Gast et al. [32] studied the chain folding in micelles of polyethylene-*block*-poly(ethylene-*alt*-propylene) (PE-*b*-PEP) block copolymers in *n*-decane. Cheng et al. [33, 34] have studied the interaction changes of the polystyrene (PS) chains on the poly(ethylene oxide) (PEO) or poly (L-lactic acide) (PLLA) platelet basal surface. Xu et al. [35, 36] reported on a strong effect of molecular weight on the micellar structure for poly(ethylene oxide)-*block*-poly(butylene oxide) (PEO-*b*-PBO, 55 wt% PEO) diblock copolymers in solution and blends with low-molecular-weight PBO. High molecular-weight PEO-*b*-PBO diblock copolymers formed spherical micelles, whereas samples with identical composition but lower molecular weight formed platelet-like structures.

Recently, Winnik, Manners and co-workers [37, 38, 39, 40, 41] have reported that block copolymers containing crystalline blocks can form cylindrical micelles. They showed that crystallization is the main driving force behind the cylindrical micelles formation of poly

(ferrocenyldimethylsilane)-*block*-polydimethylsiloxane (PFDMS-*b*-PDMS). In addition, a reversible transition was observed from cylindrical micelles to hollow nanotubes. This work has demonstrated that the interplay between aggregation and crystallization can lead to a time-dependent reorganization in micellar systems.

Here, we study the size and shape of semicrystalline block copolymer micelles using a well-defined poly(1,2-butadiene)-*block*-poly(ethylene oxide) diblock copolymer. We demonstrate that the thermally controlled crystallization of the confined poly(ethylene oxide) (PEO) core in a selective solvent leads to different but well-defined morphologies, that can be explained by concomitant aggregation and crystallization.

3.2 Experimental section

Materials and Methods. The poly (1,2-butadiene)-*block*-poly(ethylene oxide) diblock copolymer was synthesized via sequential anionic polymerization of butadiene and ethylene oxide in tetrahydrofuran using the phosphazene base *t*-BuP_4, as described elsewhere [42, 43]. The composition of the diblock copolymers is $B_{52}EO_{48}^{5.6}$ (subscripts denote the mass fraction in percent and the superscript gives the overall number average molecular weight M_n in kg/mol). The molecular weights of the B and EO blocks are 2900 g/mol and 2700 g/mol, respectively; the polydispersity index of the diblock copolymer is 1.02. The amount of 1,2-units within the polybutadiene block is 92 mol%. The polymer was dried for 2 days at 70^{o}C under vacuum, until residual traces of water were removed. The samples were prepared from 1wt% and 20wt% *n*-heptane solutions at different crystallization temperatures for the PEO block.

Cryogenic Transmission Electron Microscopy (cryo-TEM). Samples for cryo-TEM were prepared by adding a 2 μl droplet of a 1wt% solution of $B_{52}EO_{48}^{5.6}$ in *n*-heptane on a lacey carbon coated copper grid, where most of the liquid was removed with blotting paper, leaving a thin film stretched over the lace. The specimens were prepared by vitrification in liquid nitrogen and then cooled to approximately 77 K in a temperature controlled freezing unit (Zeiss Cryobox, Zeiss NTS GmbH, Oberkochen, Germany). After freezing the specimen was placed into a cryo-transfer holder (CT 3500, Gatan, München, Germany) and transferred to a Zeiss 922 OMEGA EFTEM (Zeiss NTS GmbH, Oberkochen, Germany). Due to the fact that the contrast provided by the electron-density differences between the block copolymer and the solvent is very low, the embedding *n*-heptane was heated in situ at a temperature of 163 K for 15 min and sublimated during this time [44]. After sublimation of *n*-heptane, the objects could be

identified on the supporting "lacey" carbon membrane. Subsequently, the sample was cooled to a temperature of 97 K for image recording. The TEM was operated at an acceleration voltage of 200 kV. A CCD camera system (Ultrascan 1000, Gatan) was used for image recording and the images were processed with a digital image processing system (Gatan Digital Micrograph 3.15 for GMS 1.5).

Transmission Electron Microscopy (TEM). Samples were prepared by placing a drop of the $B_{52}EO_{48}^{5.6}$ solution (0.1wt% in *n*-heptane) on a carbon-coated copper grid. After few seconds, excess solution was removed by blotting with filter paper. Subsequently, bright-field TEM was performed on a Zeiss CEM 902 operating at 80 kV. Staining was performed with OsO_4 vapor for 60 min. OsO_4 is known to selectively stain PB; i.e., PB domains are expected to appear darker compared to PEO domains, which enables to distinguish between the two polymers.

Dynamic Light Scattering (DLS). Dynamic Light Scattering was carried out on an ALV DLS/SLS-SP 5022F compact goniometer system with an ALV 5000/E correlator and a He-Ne laser ($\lambda = 632.8$ nm). All measurements were performed on a 0.1wt% solution of $B_{52}EO_{48}^{5.6}$ in *n*-heptane at a scattering angle of 90^o. A CONTIN analysis was taken for the measured intensity correlation function. For the temperature dependent measurements the toluene bath of the instrument was thermo-stated and the target temperatures were equilibrated at least 20 min before the experiments. A Second Cumulant analysis was used in order to investigate the morphology formation at different temperatures.

Wide Angle X-ray Scattering (WAXS). Time-resolved wide-angle X-ray scattering (WAXS) experiments were performed at the ID2 beam lime at the European Synchrotron Radiation Facilities (ESRF, Grenoble, France). The operating wavelength of the X-ray was $\lambda = 0.1$ nm. The intensity is represented as a function of the scattering vector $q = (4\pi \sin\theta)/\lambda$, 2θ being the scattering angle. The beam size was 0.3×0.3 μm and the sample-detector distance was 2 m. The detector was a fiber optically coupled FReLoN (Fast-Readout, Low Noise) CCD with a readout rate of 5 frames/s. Prior to data analysis, background scattering was subtracted from the data and corrections were made for spatial distortion, the detector efficiency and beamstop. Typical data acquisition time was 1s per frame separated by a waiting-time of 2.75 s. The temperature-dependent WAXS experiments were performed using a Linkam THMS600 temperature controller system as a sample holder. The hot stage was equipped with a liquid-nitrogen cooling accessory and enabled fast temperature ramps with 80 ^{o}C/min (nominal stability of 1^oC). The 20wt% solutions of the diblock copolymer in *n*-heptane

were first heated above the melting temperature at 70^{o}C and quenched to the desired crystallization temperature (-30^{o}C and 30^{o}C) and held until isothermal crystallization was completed.

3.3 Results and Discussion

3.3.1 Morphologies of $B_{52}EO_{48}^{5.6}$ in n-heptane

To study the effect of crystallization on self-assembly with a given block ratio of a block copolymer, we prepared samples having two distinct thermal histories: The dried polymer was dissolved in *n*-heptane at 70^{o}C, first. The hot *n*-heptane solution (70^{o}C) was then quenched to different crystallization temperatures: The first solution was quenched into liquid nitrogen and will correspond to pathway A. The second solution which was quenched to 30^{o}C corresponds to pathway B. All solutions were equilibrated at room temperature for at least 1 day after quenching. The solution corresponding to **pathway A** was transparent after quenching. Solutions corresponding to **pathway B** were turbid. The whole process is reversible as soon as the solutions are heated up again to 70^{o}C.

Pathway A. Fig. 3.1 shows the obtained morphologies by cryogenic transmission electron microscopy (cryo-TEM), where the samples have been prepared by in-situ freeze-drying. Spherical core-corona micelles with crystalline PEO domains were observed. The darker cores correspond to the PEO block (higher electron density) embedded in the PB matrix (lower electron density). DLS at 70^{o}C revealed the presence of spherical micelles with a molten PEO core, as will be discussed later (see Fig. 3.3). Thus, upon quenching from 70^{o}C into liquid nitrogen the spherical morphology is retained. The spherical objects appeared to be mono-disperse in size with a mean core radius of 13 nm. Fig. 3.1 (b) shows that the spherical micelles are regularly packed forming a hexagonal structure over the whole film. The packing is induced during the freeze-drying sample preparation process. This points to a rather narrow size distribution of the micelles. The size estimated from Fig. 3.1 corresponds well to the hydrodynamic radius of 18 nm measured by DLS of micellar solution after quenching in liquid nitrogen. The micellar solutions are stable over months. No aggregation was observed even after a few months by DLS at room temperature.

Pathway B. Fig. 3.1 (e, f) show the morphologies obtained through pathway B, namely, by quenching the hot solution from 70^{o}C to 30^{o}C. Pathway B leads to the formation of an novel meander-like morphology. The length of the objects is in the

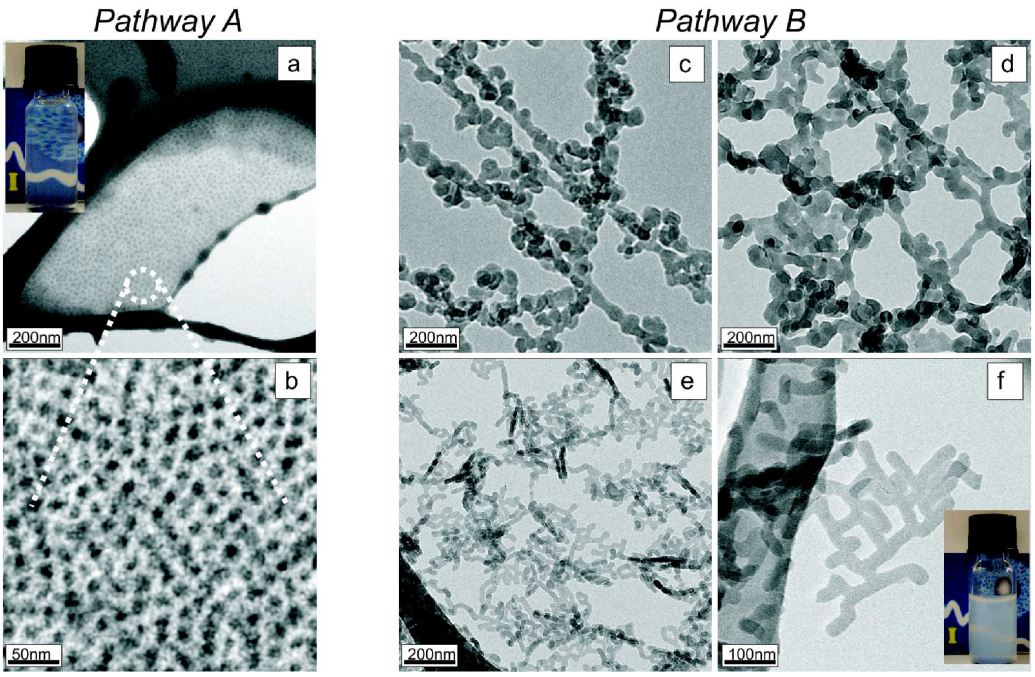

Figure 3.1: Cryo -TEM micrographs of structures formed by $B_{52}EO_{48}^{5.6}$ in *n*-heptane: (a), (b) spherical crystalline micelles obtained from pathway A and (e), (f) meander-like structures obtained from pathway B. Images (c)-(f) represent the evolution of meander-like structure over time upon cooling at 30°C after: (c) 1 min, (d) 3 min (e, f) 24 h. The inset picture from Fig. 3.1 (a) represents the solution corresponding to pathway A, and the picture from Fig. 3.1 (f) corresponds to pathway B.

range of 100nm to 1μm, enabling a bridging over the lacey carbon grids. The structure exhibits lateral growth and forms simultaneously two or four new branches of equivalent width. By tilting the samples during the image recording process the width of these objects has been shown to vary (from a minimum of 20 nm to a maximum of 35 nm). Tilted objects can be visualized in Fig. 3.1 (e) as the darker structures. This excludes a cylindrical morphology. The structure of the core resembles more a ribbon-like or rectangular prismatic structure having ellipsoidal endings.

Selectively staining of the PB domains with OsO_4 was used to obtain a closer insight into the morphology of meander-like structures. The sample was first drop coated onto a carbon-coated copper grid (0.1wt% solution in *n*-heptane), followed by staining with OsO_4 vapor for 60 min. The crystalline PEO domains in the core appear bright because of the preferential staining of the PB blocks. Well-separated darker areas (higher scattering contrast), corresponding to stained PB domains, can be detected along the PEO crystalline domains that formed the meander-like structure (Fig. 3.2).The average width of the crystalline PEO domains was 17 nm surrounded by an amorphous PB layer

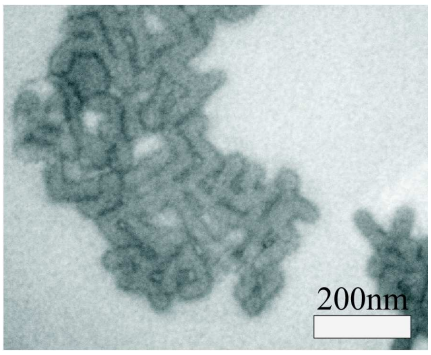

Figure 3.2: TEM micrograph of $B_{52}EO_{48}^{5.6}$ in *n*-heptane : meander-like structures obtained from pathway B. The sample was prepared by dip-coating a 0.1wt% solution onto a carbon-coated copper grid, followed by staining with OsO_4 vapor for 60 min.

of 16 nm.

Fig. 3.1 (c) and (d) display images of the $B_{52}EO_{48}^{5.6}$ structures evolved upon cooling after different times. After 1 min the amorphous micelles, which are present in the hot solution, aggregate upon cooling to 30^{o}C. The radius of these aggregates is ca. 26 nm which is twice the original radius of the micelles in hot *n*-heptane. The micrograph (Fig. 3.1(d)) taken after 3 min demonstrates clearly the aggregation of the micelles to larger objects. Moreover, the round endings of the meanders point to an aggregation of spherical micelles.

The apparent hydrodynamic radius of the meander-like structure obtained from pathway B was determined by DLS. The radius was determined to be 150-200 nm. Moreover, the evolution of the meander-like structure over time upon cooling from 70^{o}C to 30^{o}C could be monitored by DLS as well. Fig. 3.3 shows the dependence of the hydrodynamic radius on time at 70^{o}C, and after quenching from 70^{o}C to 30^{o}C for a 0.1wt% $B_{52}EO_{48}^{5.6}$ *n*-heptane solution. At 70^{o}C the DLS measurements revealed that $B_{52}EO_{48}^{5.6}$ self-assembles in *n*-heptane, a selective solvent for the PB block, into a stable micellar structure with an average hydrodynamic radius of 12 nm (see Fig. 3.3). Upon quenching to 30^{o}C (pathway B) a marked increase of the intensity is observed after an induction period of $t \sim 400s$. This is accompanied by an increase of the R_h from 12 nm to over 140 nm, indicating rearrangement of micelles and growth into larger structures. This rearrangement is relatively fast, occurring in only a few minutes and the resulting structures are stable over months.

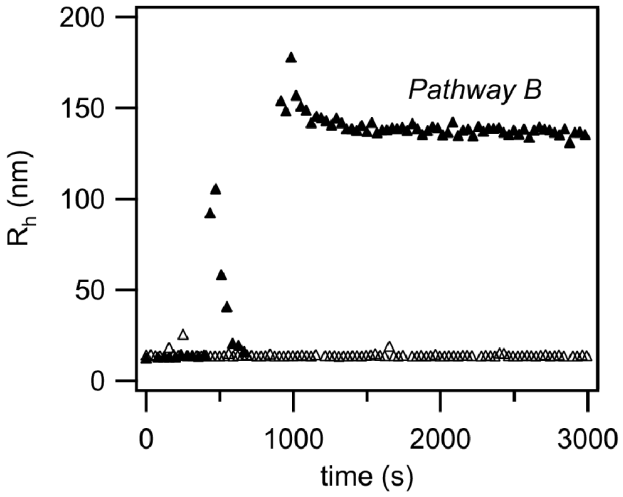

Figure 3.3: Time resolved hydrodynamic radius of $B_{52}EO_{48}^{5.6}$ in *n*-heptane solution measured by DLS at 70^{o}C (△) and after quenching at 30^{o}C (▲), pathway B. The quenching at 30^{o}C is followed by an aggregation process into a larger crystalline structure.

3.3.2 Time dependent WAXS: Crystallization kinetics

Fig. 3.4 shows the WAXS profiles as a function of time collected during isothermal crystallization experiments performed at T = -30^{o}C (a) and T = 30^{o}C (b) on a 20wt% solution. The samples have been previously equilibrated at 70^{o}C, i.e. above the melting temperature of PEO (60^{o}C), for 15 min before quenching to the crystallization temperature.

Pathway A. The PEO crystal reflections (monoclinic unit cell; cf.ref.[45, 46, 47, 48]) appeared immediately after quenching to -30^o (Fig. 3.4 (a)). The strongest PEO reflections were observed at q = 13.41 and 16.34 nm^{-1}. These peaks are assigned to the crystallographic reflection of the planes indexed by (120), and (032 + 112) of the monoclinic unit cell of the PEO crystals.

Pathway B. The isothermal crystallization at 30^{o}C is shown in the Fig. 3.4 (b). Comparing with the isothermal crystallization at -30^{o}C (Fig. 3.4 (a)), the WAXS profiles measured at T_c = 30^{o}C show only an amorphous halo scattering in the earlier stage, until the first appearance of discernable crystalline peaks at $t \sim 300$ s. This is consistent with the observed induction period in DLS (cf. Fig. 3.3). Between 300s and 600s the PEO crystals are forming the meander-like structure. The WAXS patterns show the same reflections of the monoclinic unit cell of PEO as observed in Fig. 3.4 (a) for the crystalline micelles. In addition, PEO shows a monoclinic crystal modification in $B_{52}EO_{48}^{5.6}$ bulk samples, too.

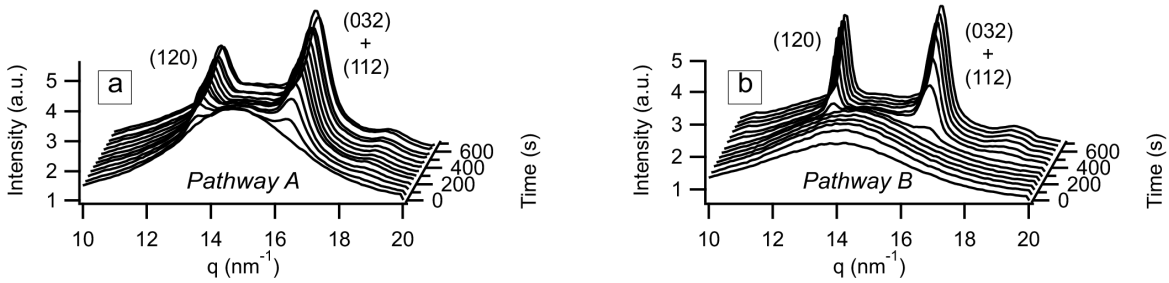

Figure 3.4: The evolution of the WAXS patterns of 20wt% $B_{52}EO_{48}^{5.6}$ in *n*-heptane quenched at a rate of 80^{o}C/min from 70^{o}C to - 30^{o}C (a) and to 30^{o}C (b), forming respectively micelles and meander-like structure. The figure shows the time-resolved WAXS profiles from the moment the quenching temperatures were reached.

3.3.3 Mechanism of Self-Assembly

All data obtained so far demonstrate that the meander-like structure is formed via a crystallization-induced aggregation of spherical micelles upon cooling. Fig. 3.6 displays the tentative mechanism of the formation of micelles along both pathways. The selective solvent *n*-heptane leads to formation of micelles having a liquid core at elevated temperatures. In case of pathway A supercooling to low temperatures leads to rapid crystallization of the cores. Thus, the structure of the micelles is fixed by crystallization and no further growth can occur.

However, if the solution is cooled down to only 30^0C, an induction period was observed by DLS and WAXS, followed by a sudden growth of the meander-like structures. Approximately at this point, crystallization starts and clear WAXS-peaks can be seen. Moreover, the ramifications seen in the later stage point to the fact that the overall shape of the meanders must be related to crystallization. Obviously, crystallization favors well-defined angles between two subsequent micelles. Thus, it seems that growth of the meanders starts around a micellar structure in which nucleation of the crystalline phase has taken place. Further micelles will aggregate and immediately become crystalline upon merging with this primary nucleus. Evidently, this is a rather fast process as shown by DLS which may be followed by a depletion of micelles around the rapidly growing core micelle. This may explain the formation of a meander-like structure which is reminiscent of fractal growth of particles. Similar fractal growth processes have been observed for diblock copolymers in thin films, too [49]. Hence, crystallization triggers the aggregation and formation of a stable super-structure. In a later stage, crystallinity within the meanders is increasing.

3.3.4 Degree of crystallinity

The degree of crystallinity was determined from the WAXS data where the reflection profiles were separated into the crystalline PEO reflections and an amorphous halo by using Vonk's method [50]. The crystallinity of the samples was calculated as the ratio between the diffracted areas under the deconvoluted crystalline peaks over the total diffracted area after subtraction of the continuous background. The shape of the amorphous halo due to the amorphous fraction was estimated from the diffraction pattern of the amorphous samples at temperatures above their melting points. Crystallinity increased to 22% in the case of the spherical micelles and up to 27% for the meander-like structures.

Further information can be obtained from an Avrami analysis. The Avrami equation can be expressed as:

$$1 - X_c = exp(-zt^n) \tag{3.1}$$

where X_c is the fraction crystallized at time t, z is a constant dependent on nucleation and growth rates and n is related to the type of nucleation and growth geometry. The Avrami exponent n is assumed to range from 1 to 4 and is related to the geometric characteristic of nuclei: $n = 1$ being ascribed to a rod, 2 to pellets or disk-like (lamellar) and 3 or 4 to a 3-D structure [51].

The information about the early stage crystallization of $B_{52}EO_{48}^{5.6}$ at T_c = -30^{o}C and T_c = 30^{o}C are given in Fig. 3.5. The Avrami exponent of 0.7 shows that a confined crystallization takes place in $B_{52}EO_{48}^{5.6}$ at low temperature (T_c = -30^{o}C). Here, in each micelle nucleation and crystallization occurs independent from all other spheres. Avrami exponents (n = 0.5) were also found by Lotz and Kovacs [52] for block copolymers with a glassy matrix and a crystallizable minority block (PEO-*b*-PS), or by Shiomi [53] for polytetrahydrofuran-*block*-polystyrene (PTHF-*b*-PS). The small exponent seems to reflect the constraints imposed by the confinement by a glassy matrix. Thus, Xu et al. [54] observed as well an Avrami exponent of $n = 0.5$ for PS-*b*-PEO-*b*-PS, which was attributed to confined crystallization.

Therefore, we conclude that the Avrami exponent of $n = 0.7$ found for pathway A is related to confined crystallization where a homogeneous nucleation exclusively takes place within each individual spherical microdomain, i.e, kinetics are determined by nucleation. The Avrami exponent thus reflects the rate at which PEO microdomains nucleate [52]. Predominant homogeneous nucleation was also observed for PEO confined

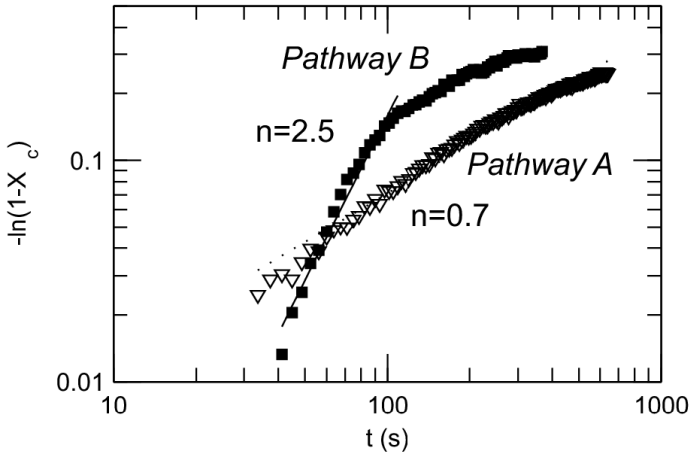

Figure 3.5: Avrami plots derived from WAXS data for $B_{52}EO_{48}^{5.6}$ isothermally crystallized at different T_c: ($\bigtriangledown$) spherical micelles, T_c = -30^{o}C, (■) meander-like structures, $T_c = 30^o$C. The dotted line and the full line represent the first degree fits from which the Avrami exponents n are obtained. The crystallization process for the meander-like structures (Pathway B) has a 300 s delay compared with the micellar structures after the temperature of crystallization was reached.

in miniemulsion droplets [55].

The situation changes when the crystals are no longer confined to the microdomains in which they nucleate, i.e., breakout occurs upon crystallization [28, 56]. Fig. 3.5 shows that a value of $n = 2.5$ is found for the early stage of the crystallization within the meanders (pathway B) at $T_c = 30^o$C. This Avrami exponent is consistent with the observed 2D growth of the meander-like structure as revealed by cryo-TEM (Fig. 3.1 (e, f)). Furthermore, comparable Avrami exponents were found for crystallization in bulk under comparable conditions [51].

Our results showed that the observed meander-like structures are formed by crystallization induced aggregation of spherical micelles upon quenching from 70^{o}C to 30^{o}C. The present results can hence be compared qualitatively to recent data obtained by Winnik, Manners and coworkers [41]. The Avrami exponent of 2.5 indicates that crystallization and aggregation of spherical micelles occurs side-by-side, rather then step-wise as reported for PEO-*b*-PBO blends with low-molecular-weight PBO [35]. Crystallization may hence be used to adjust the morphology of micellar systems.

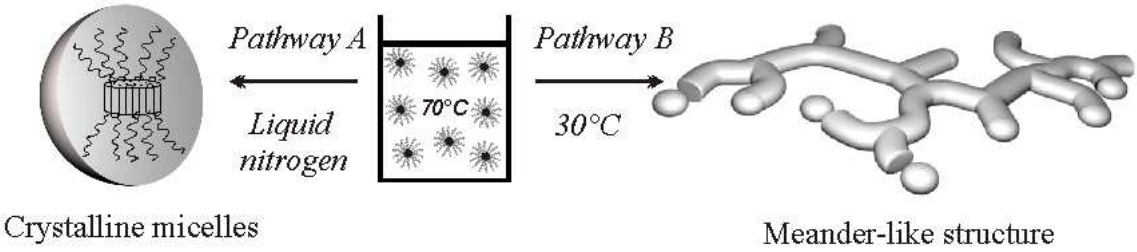

Figure 3.6: Schematic representation of different morphologies formed by $B_{52}EO_{48}^{5.6}$ in *n*-heptane driven by crystallization. The morphologies that emerge depend on the thermal history of the two different pathways A and B. Amorphous micelles are formed at 70^oC. After quenching from 70^oC by liquid nitrogen crystalline spherical micelles are formed (Pathway A), whereas a quenching at 30^oC (Pathway B) results in a branched crystalline morphology denoted as a meander-like structure with squeezed ellipsoidal endings.

3.4 Conclusion

We have observed the formation of meander-like structures and of spherical crystalline micelles for a PB-*b*-PEO diblock copolymer via crystallization upon cooling. As shown in Fig. 3.6 rapid supercooling leads to crystallization of the liquid PEO-cores and to fixation of the single spherical micelles (pathway A). In case of pathway B, i.e., by cooling down the solution to 30^0C, crystalline meanders are formed. The rapid aggregation process leads to a depletion of the micelles around this growing core leading to the ramificated meander-like structure of the micelles. Hence, crystallization induced aggregation can lead to a novel type of micellar super-structure.

Acknowledgments

The authors acknowledge helpful discussions with Alejandro Müller and Günter Reiter. A.M.M. and A.C. acknowledge the financial support from the European Community's "Marie-Curie Actions" under Contract No. MRTN-CT-2004-504052 [POLYFILM]. M.D acknowledge the financial support from the SFB 481 project.

Bibliography

[1] Harada A. and Kataoka K. *Science*, 283:65–67, 1999.

[2] Zhang L. F. and Eisenberg A. *Science*, 268:1728–1731, 1995.

[3] Pedersen J. S., Hamley I. W., Ryu C. Y., and Lodge T. P. *Macromolecules*, 33:542–550, 2000.

[4] Jenekhe S. A. and Chen X. L. *Science*, 283:372–375, 1999.

[5] Won Y. Y., Davis H. T., and Bates F. S. *Science*, 283:960–963, 1999.

[6] Discher B. M., Won Y. Y., Ege D. S., Lee J. C. M., Bates F. S., Discher D. E., and Hammer D. A. *Science*, 284:1143–1146, 1999.

[7] Discher D. E. and Eisenberg A. *Science*, 297:967–973, 2002.

[8] Won Y. Y., Brannan A. K., Davis H. T., and Bates F. S. *J. Phys. Chem. B*, 106:3354–3364, 2002.

[9] Yang L. and Alexandridis P. *Curr. Opin. Colloid Interface Sci.*, 5:132–143, 2000.

[10] Yu K., Zhang L. F., and Eisenberg A. *Langmuir*, 12:5980–5984, 1996.

[11] Yu Y. S., Zhang L. F., and Eisenberg A. *Macromolecules*, 31:1144–1154, 1998.

[12] Svensson M., Alexandridis P., and Linse P. *Macromolecules*, 32:637–645, 1999.

[13] Park M., Harrison C., Chaikin P. M., Register R. A., and Adamson D. H. *Science*, 276:1401–1404, 1997.

[14] Malmsten M. *Soft Matter*, 2:760–769, 2006.

[15] Minatti E., Viville P., Borsali R., Schappacher M., Deffieux A., and Lazzaroni R. *Macromolecules*, 36:4125–4133, 2003.

[16] Ouarti N., Viville P., Lazzaroni R., Minatti E., Schappacher M., Deffieux A., and Borsali R. *Langmuir*, 21:1180–1186, 2005.

[17] Zheng Y., Won Y. Y., Bates F. S., Davis H. T., Scriven L. E., and Talmon Y. *J. Phys. Chem. B*, 103:10331–10334, 1999.

[18] Bhargava P., Tu Y. F., Zheng J. X., Xiong H. M., Quirk R. P., and Cheng S. Z. D. *J. Am. Chem.Soc.*, 129:1113–1121, 2007.

[19] Allen C., Maysinger D., and Eisenberg A. *Colloids Surf., J. B*, 16:3–27, 1999.

[20] Choucair A. and Eisenberg A. *Eur. Phys. J. E*, 10:37–44, 2003.

[21] Soo P. L. and Eisenberg A. *J. Polym. Sci., Part B: Polym. Phys.*, 42:923–938, 2004.

[22] Zhang L. F., Yu K., and Eisenberg A. *Science*, 272:1777–1779, 1996.

[23] Lotz B. and Kovacs A. J. *Kolloid Z. Z. Polym.*, 209:97–114, 1966.

[24] Lotz B., Kovacs A. J., Bassett G. A., and Keller A. *Kolloid Z. Z. Polym.*, 209:115–128, 1966.

[25] Ryan A. J., Hamley I. W., Bras W., and Bates F. S. *Macromolecules*, 28:3860–3868, 1995.

[26] Loo Y. L., Register R. A., and Ryan A. J. *Phys. Rev. Lett.*, 84:4120–4123, 2000.

[27] Reiter G., Castelein G., Sommer J. U., Rottele A., and Thurn-Albrecht T. *Phys. Rev. Lett.*, 87:226101–1–226101–4, 2001.

[28] Müller A. J., Balsamo V., Arnal M. L., Jakob T., Schmalz H., and Abetz V. *Macromolecules*, 35:3048–3058, 2002.

[29] Cogan K. A. and Gast A. P. *Macromolecules*, 23:745–753, 1990.

[30] Gast A. P., Vinson P. K., and Coganfarinas K. A. *Macromolecules*, 26:1774–1776, 1993.

[31] Richter D., Schneiders D., Monkenbusch M., Willner L., Fetters L. J., Huang J. S., Lin M.; Mortensen K., and Farago B. *Macromolecules*, 30:1053–1068, 1997.

[32] Lin E. K. and Gast A. P. *Macromolecules*, 29:4432–4441, 1996.

[33] Chen W. Y., Zheng J. X., Cheng S. Z. D., Li C. Y., Huang P., Zhu L., Xiong H. M., Ge Q., Guo Y., Quirk R. P., Lotz B., Deng L. F., Wu C., and Thomas E. L. *Phys. Rev. Lett.*, 93:028301–1–028301–4, 2004.

[34] Zheng J. X., Xiong H. M., Chen W. Y., Lee K. M., Van Horn R. M., Quirk R. P., Lotz B.; Thomas E. L., Shi A. C., and Cheng S. Z. D. *Macromolecules*, 39:641–650, 2006.

[35] Xu J. T., Jin W., Liang G. D., and Fan Z. Q. *Polymer*, 46:1709–1716, 2005.

[36] Xu J. T., Fairclough J. P. A., Mai S. M., and Ryan A. J. *J. Mater. Chem*, 13:2740–2748, 2003.

[37] Guerin G., Raez J., Manners I., and Winnik M. A. *Macromolecules*, 38:7819–7827, 2005.

[38] Raez J., Barjovanu R., Massey J. A., Winnik M. A., and Manners I. *Angew. Chem. Int. Ed.*, 39:3862–3865, 2000.

[39] Raez J., Tomba J. P., Manners I., and Winnik M. A. *J. Am. Chem. Soc.*, 125:9546–9547, 2003.

[40] Korczagin I., Hempenius M. A., Fokkink R. G., Stuart M. A. C., Al-Hussein M., Bomans P. H. H., Frederik P. M., and Vancso G. J. *Macromolecules*, 39:2306–2315, 2006.

[41] Shen L., Wang H., Guerin G., Wu C., Manners I., and Winnik M. *Macromolecules*, 41:4380–4389, 2008.

[42] Schmalz H., Lanzendörfer M. G., Abetz V., and Müller A. H. E. *Macromol. Chem. Phys.*, 204:1056–1071, 2003.

[43] Schmalz H., Knoll A., Müller A. J., and Abetz V. *Macromolecules*, 35:10004–10013, 2002.

[44] Borsali R., Minatti E., Putaux J.-L., Schappacher M., Deffieux A., Viville P., Lazzaroni R., and Narayanan T. *Langmuir*, 19:6–9, 2003.

[45] Tadokoro H., Chatani Y., Yoshihara T., Tahara S., and Murahashi S. *Makromol. Chem.*, 73:109–127, 1964.

[46] Takahash Y., Sumita I., and Tadokoro H. *J. Polym. Sci., Part B: Polym. Phys.*, 11:2113–2122, 1973.

[47] Takahash Y. and Tadokoro H. *Macromolecules*, 6:672–675, 1973.

[48] Zhu L., Huang P., Chen W. Y., Ge Q., Quirk R. P., Cheng S. Z. D., Thomas E. L., Lotz B., Hsiao B. S., Yeh F. J., and Liu L. Z. *Macromolecules*, 35:3553–3562, 2002.

[49] Reiter G., Hörner P., Hurtrez G., Riess G., Sommer J. U., and Joanny J. F. *J. Surf. Sci.Technol.*, 14:93–103, 1998.

[50] Vonk C. G. *J. Appl. Crystallogr.*, 6:148–152, 1973.

[51] Xu J. T., Fairclough J. P. A., Mai S. M., Ryan A. J., and Chaibundit C. *Macromolecules*, 35:6937–6945, 2002.

[52] Lotz B. and Kovacs A. *Am. Chem. Soc., Div. Polym. Chem.*, 10:820, 1969.

[53] Shiomi T., Imai K., Takenaka K., Takeshita H., Hayashi H., and Tezuka Y. *Polymer*, 42:3233–3239, 2001.

[54] Xu J. T., Yuan J. J., and Cheng S. Y. *Eur. Polym. J*, 39:2091–2098, 2003.

[55] Taden A. and Landfester K. *Macromolecules*, 36:14037–4041, 2003.

[56] Müller A., Balsamo V., and Arnal M. L. *Adv. Polym. Sci.*, 190:1–63, 2005.

CHAPTER 4

Crystallization-Induced Aggregation of Block Copolymer Micelles: Influence of Crystallization Kinetics on Morphology

Abstract
We present a systematic investigation of the crystallization and aggregation behavior of a poly (1,2-butadiene)-*block*-poly(ethylene oxide) diblock copolymer (PB-*b*-PEO) in *n*-heptane. *n*-Heptane is a poor solvent for PEO and at 70^0C the block copolymer self-assembles into spherical micelles composed of a liquid PEO core and a soluble PB corona. Time- and temperature-dependent light scattering experiments revealed that when crystallization of the PEO cores is induced by cooling, the crystal morphology depends on the crystallization temperature (T_c): Below 30^0C, the high nucleation rate of the PEO core dictates the growth of the crystals by a fast aggregation of the micelles into meander-like (branched) structures due to a depletion of the micelles at the growth front. Above 30^0C the nucleation rate is diminished and a relatively small crystal growth rate leads to the formation of twisted lamellae as imaged by scanning force microscopy. All data demonstrate that the formation mechanism of the crystals through micellar aggregation is dictated by two competitive effects, namely, by the nucleation and growth of the PEO core.

The results of this chapter have been published as:

Crystallization-Induced Aggregation of Block Copolymer Micelles: Influence of Crystallization Kinetics on Morphology
by Adriana M. Mihut, Jérôme J. Crassous, Holger Schmalz and Matthias Ballauff, *Colloid. Polym. Sci.*, **2009**, DOI 10.1007/s00396-010-2185-y.

4.1 Introduction

Self-assembly of crystalline-coil block copolymers in solution has attracted steadily increasing attention during the last years since the resulting morphology may be largely influenced by the crystallizable block. In selective solvents, the insoluble block undergoes chain folding upon crystallization and the expected morphology can be viewed as the solvent-soluble corona blocks being grafted on both sides of the lamellar crystalline core [1, 2, 3]. The chain-folded crystalline region leads to a dense packing of the amorphous blocks and results in highly stretched tethered chains. The overall shape thus depends on the interplay between the interfacial energy of the crystalline block and the solvent, and the stretching within the amorphous block [4]. Thus, the micellar architecture is strongly influenced by the crystallization conditions, such as temperature [5], and composition of the block copolymers [3, 6, 7, 8, 9, 10, 11].

By changing composition, solvent, and structure of the crystalline block, spherical [8, 12, 13, 14], cylindrical [10, 15, 16], and lamellar micelles were observed [1, 3, 6, 17, 18]. Winnik and co-workers reported recently the possibility to obtain cylindrical micelles with controlled dimensions and architectures of organometallic block copolymers containing the crystallizable polyferrocenyldimethylsilane (PFS) as one block. These authors, reported the transition from spherical micelles to wormlike, cylindrical or tubular morphologies in nonpolar selective solvent [9, 19, 20, 21]. Recently, the formation of wormlike micelles was observed in which the corona had undergone a microphase separation in organic media due to crystallization-induced aggregation of triblock terpolymers [15].

In our previous studies we demonstrated that solutions of poly(butadiene)-*block*-poly(ethylene oxide) in *n*-heptane present a good model system for the study of the interplay between crystallization and aggregation. For a symmetric PB-*b*-PEO block copolymer ($B_{52}EO_{48}^{5.6}$) in *n*-heptane, a fast quenching in liquid nitrogen results in the formation of crystalline micelles retaining the spherical shape present in the molten state at 70^0C [22]. If crystallization took place at 30^0C, a meander-like structure was formed. Moreover, in the case of a highly asymmetric PB-*b*-PEO block copolymer ($B_{88}EO_{12}^{29.5}$) we observed rod-like micelles [23]. With time these rod-like micelles aggregate and re-crystallize in solution forming long needles. Investigation on a poly(ϵ- caprolactone)-*b*-poly(ethylene oxide) (PCL-*b*-PEO) block copolymer showed that the morphology can be influenced by the crystallization temperature, due to an increased chain folding at lower crystallization temperatures [5].

All previous studies have highlighted the importance of the kinetics of crystallization for the resulting morphology. A more detailed investigation of the various factors influencing the micellization of semicrystalline systems is very important and a fundamental understanding is still lacking. In this study, we discuss the effect of crystallization kinetics on the formed morphology upon crystallization- induced aggregation of spherical micelles of a symmetric poly(1,2-butadiene)-*block*-poly(ethylene oxide) diblock copolymer ($B_{52}EO_{48}^{5.6}$). The evolution of the size of the aggregates and the kinetics at different crystallization temperatures (T_c) was monitored by static (SLS) and dynamic light scattering (DLS). The resulting crystalline micellar morphologies were imaged by scanning force microscopy (SFM). The combination of the various techniques indicated that the final morphology is directly controlled by T_c: meander-like structures formed at low T_c, whereas higher T_c lead to twist lamellae formation.

4.2 Experimental section

The poly(1,2-butadiene)-*block*-poly(ethylene oxide) diblock copolymer was synthesized via sequential anionic polymerization with a composition given by $B_{52}EO_{48}^{5.6}$ as described elsewhere [24, 25, 26]. The subscripts denote the mass fraction in percent and the superscript gives the overall number average molecular weight of the block copolymer in kg/mol. The molecular weights of the PB and PEO blocks are 2.9 kg/mol and 2.7 kg/mol, respectively. The polydispersity index of the diblock copolymer is 1.02. The samples were prepared from 0.1 wt% *n*-heptane solutions at different crystallization temperatures for the PEO block.

Differential scanning calorimetry (DSC) measurements were performed on a Setaram MicroDSC III in screwcapped stainless aluminum cells. The samples were heated from 25^0C to 80 ^{0}C and cooled again to 25 ^0C at a scanning rate of 0.5 ^0C min^{-1}. This cycle was performed three times to check reversibility of the transitions. The samples were kept at 25 ^0C for 60 min and 20 min at 80 ^0C.

Dynamic (DLS) and static light scattering (SLS) were carried out on a ALV compact goniometer system equipped with a He-Ne laser (λ = 632.8 nm). All measurements were performed on 0.1 wt% solutions of $B_{52}EO_{48}^{5.6}$ in *n*-heptane at a scattering angle of 90 ^{o}. The hydrodynamic radius R_H derived from the second cumulant analysis was monitored in two degrees steps with a waiting time of 5 min at each temperature. The samples for the aggregation kinetics were first kept at 70 ^0C during 20 min to erase the thermal history. Then, the samples were quenched in the DLS to different crystallization

temperatures. R_H and I/I_0 were monitored every 15 s during 2 hours.
The SFM experiments were performed using a Dimension 3100M microscope (Veeco Instruments) equipped with a Nanoscope software operated in TappingMode at room temperature. The samples were prepared by spin-coating the 0.1 wt% $B_{52}EO_{48}^{5.6}$ solution onto freshly cleaned silicon wafers. Scan rates between 0.5 - 1.0 Hz were used. The crystalline PEO block is much stiffer then the amorphous PB block which allowed us an imaging mode base on a mechanical contrast, complementary to the topographic imaging mode.

4.3 Results and Discussion

4.3.1 Influence of Crystallization Temperature (T_c) on the Micellar Morphology

Recently, we described that crystallization of a poly(1,2-butadiene)-*block*-poly(ethylene oxide) diblock copolymer ($B_{52}EO_{48}^{5.6}$) in *n*-heptane yielded spherical and meander-like micelles via a fast quenching of the hot solutions (70^0C) into liquid nitrogen (pathway B) and to 30 ^0C (pathway A), respectively [22]. The micelles were composed of a crystalline PEO core and a soluble PB corona. The meander structure formed via crystallization-induced aggregation of spherical micelles upon cooling in *n*-heptane. In this study, samples with different thermal histories were prepared in order to investigate the influence of the crystallization conditions on the finally formed morphology. The 0.1 wt% solutions of $B_{52}EO_{48}^{5.6}$ block copolymer in *n*-heptane were kept at 70^0C for 20 min, in order to erase any thermal history, and then quenched for two hours to 20 ^0C, 30^0C and 34^0C, respectively. The phase-contrast images clearly confirm the morphological difference between the crystals formed at a distinct T_c (Fig. 4.1).

Fig. 4.1 (A-D) shows the meander-like morphologies formed in the solutions crystallized at 20^0 and 30^0C, respectively. The width of the meanders was found to be rather uniform, 35 ± 5nm (Fig. 4.1 A, B) and 40 ± 4 nm (Fig. 4.1 C, D), quantified by measurements from over 50 crystals. The length distribution of the branches is relatively broad, ranging from 35 nm to 300 nm at T_c= 30^0C. The branch lengths of the meanders formed at 20^0C, is much shorter, varying from 35 nm to 150 nm.

At 30^0C, the width of the ribbon-like PEO core has an average value of 20 ± 2 nm, surrounded by an amorphous PB layer of 20 ± 4 nm. The bright areas correspond to the PEO block surrounded by the PB layer as the darker areas indicated in Fig. 4.1

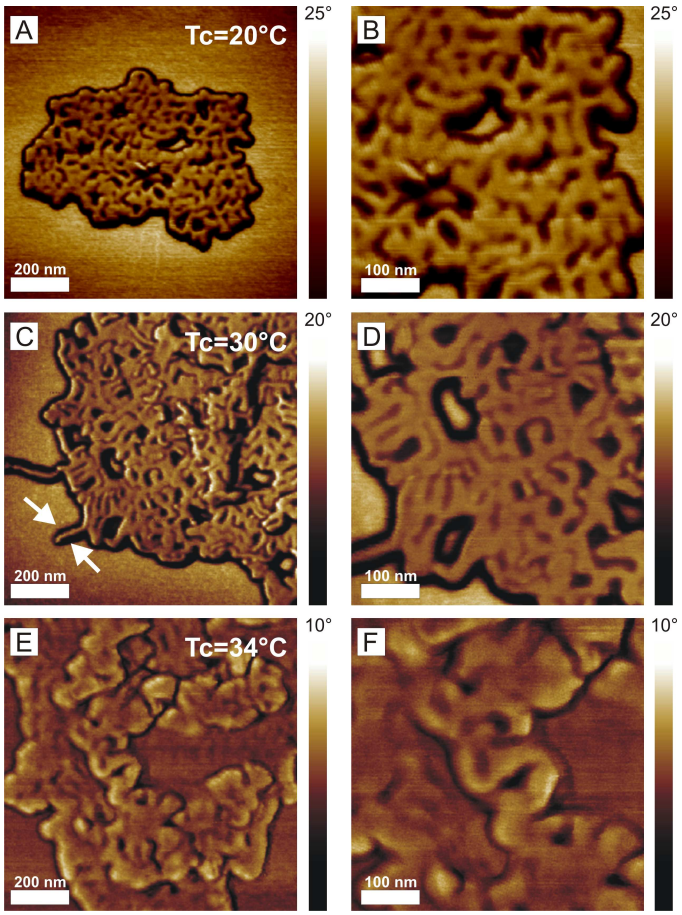

Figure 4.1: SFM phase image of $B_{52}EO_{48}^{5.6}$ crystalline micelles from a 0.1wt% solution in *n*-heptane after quenching to 20^0C (A, B), 30^0C (C, D) and 34^0C (E, F). The arrows point out to the PEO block (light areas) and the surrounding PB layer (darker area) as can be visualized from the phase contrast difference between the two polymers.

C. The higher contrast of the PEO core is related to a more dense packing of chains in a crystallite compared to the amorphous state. Similar values for the meanders were found in our previous work at this crystallization temperature. The overall thickness measured by SFM from the height images was 16 nm and 17 nm at 20^0C and 30^0C, respectively. The overall shape of the morphologies resembles that of a fractal growth [27], and is consistent with our previous investigations [22].

In contrast, when the solution is quenched to 34 ^0C (Fig. 4.1 E, F) a change of the crystal morphology is observed which hints to a twisted lamellae. The thickness of the twisted lamellae is 18 nm, which is comparable with that of the meanders. This shows that there is not change in chain folding due to T_c. The average width of the crystals increased to 80 $\pm$ 18 nm (quantified from measurements of over 50 crystals) which is twice the size of the crystals formed at lower crystallization temperatures, however the

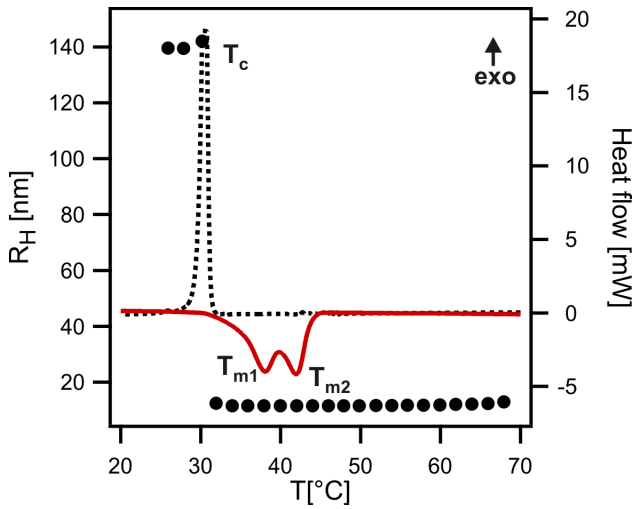

Figure 4.2: Left: Temperature dependence of the hydrodynamic radius (black circles) of a 0.1 wt% solution of $B_{52}EO_{48}^{5.6}$ upon cooling from 70^0C to 20^0C. Right: DSC cooling (black dash line) and heating scans (red line) of a 10 wt% solution of $B_{52}EO_{48}^{5.6}$ in *n*-heptane.

widths are not as uniform as compared to that of the meanders formed at 20^0 or 30^0C.

In thin films it has been demonstrated that the lamellae thickness increases with crystallization temperature [28, 29], as large undercooling induced a large chain-folding number, whereas at higher T_c the crystalline polymer chains adopted a fully extended conformation. In addition, investigations on a poly(ϵ-caprolactone)-*b*-poly(ethylene oxide) (PCL-*b*-PEO) block copolymer showed that the extend of chain folding, and as a result the final morphology, can be influenced by the crystallization temperatures [5]. However, in our case the different morphology formed at 34^0C does not result from a change in the extend of chain folding, as the thickness of the crystals is comparable to that formed at lower crystallization temperatures. This point will be discussed in more detail in the next section.

4.3.2 Kinetics and Mechanism of Structure Formation

The structure formation upon cooling from 70^0C to 20^0C of the $B_{52}EO_{48}^{5.6}$ *n*-heptane solution has been investigated by differential scanning calorimetry (DSC) and dynamic light scattering (DLS). DSC measurements (Fig. 4.2 Right) revealed a broaden crystallization transition between 27 and 32 ^0C with a maximum crystallization peak at 30 ^0C. The onset of the crystallization at 30 ^0C was supported by DSL measurements, where an increase from 12 to 140 nm of the hydrodynamic radius R_H was observed and is consistent with our previous investigations (Fig. 4.2 Left) [22]. DSC exposed a novel behavior

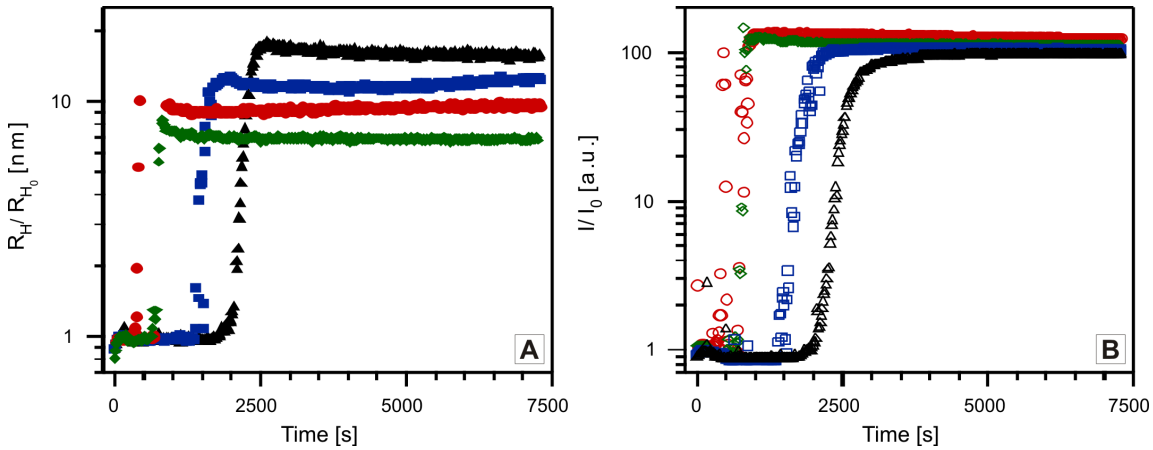

Figure 4.3: Evolution of the normalized hydrodynamic radius R_H/R_0 (A) and of the normalized scattering intensity I/I_0 (B) of 0.1wt% solution of $B_{52}EO_{48}^{5.6}$ in n-heptane first equilibrated at 70^0C and then immersed directly at 34^0C (black triangle), 32^0C (blue square), 30^0C (red circles) and 20^0C (green diamond). The full symbols correspond to the R_H/R_{H_0} and the empty symbols to I/I_0.

in n- heptane solution, which indicated two melting endothermal peaks at 38^0C (T_{m_1}) and 42^0C (T_{m_2}), whereas in the bulk only a single melting peak at 47^0C was observed. Hence, the double melting endotherms could not be observed in bulk, it is reasonably to inferred that this behavior is induced by the morphology formed in the solution. As the meanders are branched lammelar structures, the first melting endothermal peak from 38^0C has to be related with the melting of the less perfect branched points, whereas the second melting peak from 42^0C points out to the complete melting of the lamellar unites. The DSC heating trace at 70^0C is far away from the melting temperature of the crystals, i.e., no thermal history is expected at this temperature.

The kinetics of the crystallization/aggregation process and the size evolution of the aggregates were monitored measuring the time dependence of the R_H and I/I_0 after fast quenching of the 0.1 wt% solution from 70^oC to different T_c directly in the DLS bath. Fig. 4.3 displays the evolution with time of R_H/R_{H_0} and I/I_0 while quenching to different T_c. The R_H and I at time t was normalized to its initial average value R_{H_0} and I_0, respectively before the onset of the crystallization/ aggregation. The R_H retained a constant value of 12 nm when the solution is quenched to 35^0C or higher temperatures. At temperatures below 35 ^0C crystallization takes place in the micellar PEO core as monitored by the increase of R_H (Fig. 4.3 (A)). This indicates rearrangement of micelles and growth into larger structures. An enhancement of the normalized intensity of about two decades marked this transition (Fig. 4.3 (B)). R_H strongly depends on T_c, i.e., R_H decreases with decreasing T_c, from 195 nm at T_c= 34 ^0C to 85 nm at T_c= 20 ^0C,

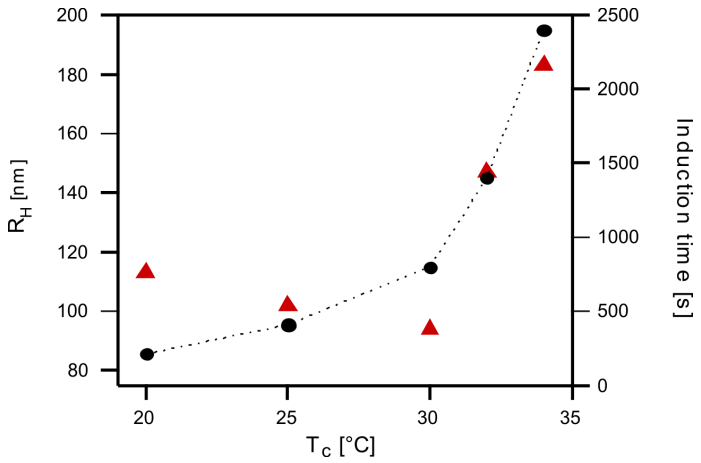

Figure 4.4: Dependence of the size of crystalline micelles (black circles with dash line) and of the induction time of the primary nucleation process (red triangle) on the crystallization temperature (T_c).

respectively (Fig. 4.4).

A small induction time of the crystallization process was recorded at $T_c \leq 30^0C$ (only few seconds), whereas at $T_c = 34\ ^0C$ was delayed with 30 min (Fig. 4.4). The shortest induction time (400 s) was observed at 30^0C, where the maximum of the crystallization exotherm was observed in micro-DSC measurements (Fig. 4.2). Moreover, the crystallization temperature affects the aggregation time of the micelles, that is, the time until a stable R_H plateau is reached, after the onset of crystallization. The lowest aggregation time was observed at $T_c \leq 30^0C$, as 225 and 470 s at 20 and 30^0C, respectively. At $T_c > 30^0C$, the aggregation time increased to 730 s at $34\ ^0C$.

The above results suggest the presence of two types of mechanism where the crystal growth proceeds in different manners. At $T_c \leq 30^0C$, crystallization induced a high nucleation rate in the solution on a narrow time scale. Subsequently, fast aggregation of adjacent micellar neighbors and fast advancing of the crystallization front in the solution leads to fast depletion of micelles at the growing front. Herein, the crystallization front, therefore the nucleation and growth process, propagates very fast in the solution.

At $T_c > 30^0C$, the nucleation rate is lowered and only few nuclei formed at the same time in the solution. At 34^0C, the long induction time of crystallization hinder the detection of an endothermic signal in the DSC, that is, nucleation is too slow at this temperature to create nuclei at a slow cooling rate of $0.5^0C\ \text{min}^{-1}$ (see Fig. 4.2). Due to the reduced number of nuclei/time the growth process is slow and no depletion of micelles occurred at the crystal growth front, as a gradual development of R_H to a stable value was observed (Fig. 4.3 (A)). Here, the growth process has obviously become the step

that determines the crystal pattern rather than the nucleation process. It is interesting to note that the crystal morphology changed from meanders (branched lamellae) to twist lamellae at $T_c > 30^0C$ (Fig. 4.1).

4.4 Conclusion

We can hence conclude that the resulting morphology is controlled by two competitive effects, namely, by the nucleation and growth of the PEO micellar core: At lower T_c, the nucleation rate is high, the crystal growth front is accelerated which results in a meander-like morphology. At higher T_c the nucleation rate is lowered. Thus, the micelles have enough time to reach the growth front of the crystals favoring the formation of twisted lamellae. This procedure allows us to tune morphological structures in dependence on crystallization temperature by change of the growth kinetics.

Acknowledgments

Financial support by the Deutsche Forschungsgemeinsschaft, SFB 840, Bayreuth, is gratefully acknowledged. We thank Dieter Gräbner (University of Bayreuth, BZKG) for conducting the DSC measurements. A.M.M. acknowledge the financial support from the European Community's "Marie-Curie Actions" under Contract No. MRTN-CT-2004-504052 [POLYFILM].

Bibliography

[1] B. Lotz and A. J. Kovacs. *Kolloid Z.Z.Polym.*, 209:97–114, 1966.

[2] B. Lotz, A. J. Kovacs, G. A. Bassett, and A. Keller. *Kolloid Z.Z.Polym.*, 209:115–128, 1966.

[3] E. K. Lin and A. P. Gast. *Macromolecules*, 29:4432–4441, 1996.

[4] T. Vilgis and A. Halperin. *Macromolecules*, 24:2090–2095, 1991.

[5] Z. X. Du, J. T. Xu, and Z. Q. Fan. *Macromol. Rapid Commun.*, 29:467–471, 2008.

[6] D. Richter, D. Schneiders, M. Monkenbusch, L. Willner, L. J. Fetters, J. S. Huang, M. Lin, K. Mortensen, and B. Farago. *Macromolecules*, 30:1053–1068, 1997.

[7] J. A. Massey, K. Temple, L. Cao, Y. Rharbi, J. Raez, M. A. Winnik, and I. Manners. *J. Am. Chem. Soc.*, 122:11577–11584, 2000.

[8] J. T. Xu, J. P. A. Fairclough, S. M. Mai, and A. J. Ryan. *J. Mater. Chem.*, 13:2740–2748, 2003.

[9] L. Shen, H. Wang, G. Guerin, C. Wu, I. Manners, and M.A Winnik. *Macromolecules*, 41:4380–4389, 2008.

[10] Z. X. Du, J. T. Xu, and Z. Q. Fan. *Macromolecules*, 40:7633–7637, 2007.

[11] J. Fu, B. Luan, X. Yu, Y. Cong, J. Li, C. Pan, Y. Han, Y. Yang, and B. Li. *Macromolecules*, 37:976–986, 2004.

[12] J. T. Xu, W. Jin, G. D. Liang, and Z. Q. Fan. *Polymer*, 46:17091716, 2005.

[13] L. Cao, I. Manners, and M. A. Winnik. *Macromolecules*, 35:8258–8260, 2002.

[14] J. Fu, B. Luan, X. Yu, Y. Cong, J. Li, Y. Pan, C.and Han, Y. Yang, and B. Li. *Macromolecules*, 37:976–986, 2004.

[15] H. Schmalz, J. Schmelz, M. Drechsler, J. Yuan, A. Walther, K. Schweimer, and A. M. Mihut. *Macromolecules*, 41:3235–3242, 2008.

[16] M. Lazzari, D. Scalarone, C. Vazquez-Vazquez, and M. A. Lopez-Quintela. *Macromol. Rapid Commun.*, 29:352–357, 2008.

[17] J. X. Zheng, H. M. Xiong, W. Y. Chen, K. M. Lee, R. M. Van Horn, R. P. Quirk, B. Lotz, E. L. Thomas, A. C. Shi, and S. Z. D. Cheng. *Macromolecules*, 39:641–650, 2006.

[18] T. Gädt, N. S. Ieong, G. Cambridge, Winnik M. A., and Manners I. *Nat. Mater.*, 8:144 – 150, 2009.

[19] G. Guerin, J. Raez, I. Manners, and M. A. Winnik. *Macromolecules*, 38:7819–7827, 2005.

[20] J. Raez, R. Barjovanu, J. A. Massey, M. A. Winnik, and I. Manners. *Angew. Chem. Int. Ed.*, 39:3862–3865, 2000.

[21] J. Raez, J. P. Tomba, I. Manners, and M. A. Winnik. *J. Am. Chem. Soc.*, 125:9546–9547, 2003.

[22] A. M. Mihut, A. Chiche, M. Drechsler, H. Schmalz, E. Di Cola, G. Krausch, and M. Ballauff. *Soft Matter*, 5:208–213, 2009.

[23] A. M. Mihut, M. Drechsler, M. Möller, and M. Ballauff. *accepted to Macromol. Rapid. Commun.*

[24] H. Schmalz, M. G. Lanzendörfer, V. Abetz, and A. H. E. Müller. *Macromol. Chem. Phys.*, 204:1056–1071, 2003.

[25] H. Schmalz, A. Knoll, A. J. Müller, and V. Abetz. *Macromolecules*, 35:10004–10013, 2002.

[26] R. V. Castillo, M. L. Arnal, A. J. Müller, I. W. Hamley, V. Castelletto, H. Schmalz, and V. Abetz. *Macromolecules*, 41:879–889, 2004.

[27] G. Reiter, P. Hörner, G. Hurtrez, G. Riess, J. U. Sommer, and J. F. Joanny. *J. Surf. Sci.Technol.*, 14:93–103, 1998.

[28] J. U. Sommer and G. Reiter. *J. Chem. Phys.*, 112:4384–4393, 2000.

[29] G. Reiter and J. U. Sommer. *J. Chem. Phys.*, 112:4376–4383, 2000.

CHAPTER 5

Sphere-to-Rod Transition of Micelles formed by the Semicrystalline Polybutadiene-*b*-Poly(ethylene oxide) Block Copolymer in a Selective Solvent

Abstract
We present a morphological study of the micellization of an asymmetric semicrystalline block copolymer, poly(butadiene)-*b*-poly(ethylene oxide), in the selective solvent *n*-heptane. The molecular weights of the poly(butadiene) (PB) and poly(ethylene oxide) (PEO) blocks are 26 kg/mol and 3.5 kg/mol, respectively. In this solvent, micellization into a liquid PEO-core and a corona of PB-chains takes place at room temperature. Through a thermally controlled crystallization of the PEO core at -30^0C, spherical micelles with a crystalline PEO core and a PB corona are obtained. However, crystallization at much lower temperatures (-196^0C; liquid nitrogen) leads to the transition from spherical to rod-like micelles. With time these rod-like micelles aggregate and form long needles. Concomitantly, the degree of crystallinity of the PEO-cores of the rod-like micelles increases. The transition from a spherical to a rod-like morphology can be explained by a decrease of solvent power of the solvent *n*-heptane for the PB-corona chains: *n*-Heptane becomes a poor solvent at very low temperatures leading to a shrinking of the coronar chains. This favors the transition from spheres to a morphology with a smaller mean curvature, that is, to a cylindrical morphology.

The results of this chapter have been published as:

Sphere-to-Rod Transition of Micelles formed by the Semicrystalline Poly(butadiene)-*b*-Poly(ethylene oxide) Block Copolymer in a Selective Solvent
by Mihut M. Adriana, Markus Drechsler, Michael Möller, and Matthias Ballauff, *Macromol. Rapid. Commun*, **2009**, DOI 10.1002/marc.200900571.

5.1 Introduction

Semicrystalline block copolymers have attracted a lot of interest in recent years because the subtle interplay of microphase separation of the blocks and crystallization may lead to new morphologies [1, 2, 3, 4]. Thus, in opposite to amorphous diblock copolymers in a selective solvent that form mostly spherical micelles, semicrystalline diblock copolymers self-assemble to form crystalline lamellar domains in which the micellar core is covered by a layer of the solvated amorphous amorphous block [2, 5, 6, 7, 8, 9]. Up to now, platelets, spherical and cylindrical micelles are the morphologies observed in highly selective solvents where the insoluble block can crystallize [2, 3, 6, 8, 10, 11, 12, 13, 14].

Recently, Winnik, Manners and co-workers demonstrated that block copolymers containing the crystallizable polyferrocenyldimethylsilane (PFS) as one block exhibit a unique phase behavior in the presence of a nonpolar selective solvent [15, 16, 17]. These authors have shown that micellar morphologies with cylinder-cylinder and platelet-cylinder connections are formed by epitaxial crystallization of PI-*b*-PSF diblock copolymers. The length of the micelles can be controlled by addition of additional PFS block-copolymer unimers acting as micellar seeds [18]. Thus, crystallization of one block may lead to new morphologies in a controlled manner.

In a previous study we demonstrated that thermally controlled crystallization of a symmetric poly(butadiene)-*block*-poly(ethylene oxide) block copolymer in the selective solvent *n*-heptane leads to different micellar morphologies depending on the pathway: [19] Supercooling to low temperatures, that is, immersion into liquid nitrogen, leads to rapid crystallization of the liquid PEO core. In this case the spherical micellar morphology that had formed previously in solution is retained. However, a novel type of meander-like structure was formed when crystallization take place at -30^oC. This structure was shown to result from the crystallization-induced aggregation of the spherical micelles. Hence, this work demonstrated that solutions of poly(butadiene)-*block*-poly(ethylene oxide) block copolymer in *n*-heptane present an excellent model system for the study of the interplay between aggregation and crystallization. In particular, the low melting point of *n*-heptane allows us to explore a wide range of temperatures not accessible by many other systems.

In this communication we extend these studies to the analysis of a highly asymmetric poly (butadiene)-*block*-poly(ethylene oxide) block copolymer. Compared to the system studied previously [19], the PB block is now the major component and longer by a factor of 7 than the crystalline PEO block. Using *n*-heptane we report on the formation of novel

crystalline micellar morphologies generated in solution through a thermally controlled crystallization of the PEO core. We demonstrate that changing the solvent power of the selective solvent for the corona block is a factor that can be used for control of the resulting morphologies.

5.2 Experimental

The diblock copolymer used in this study is poly (butadiene)-*block*-poly(ethylene oxide) (Polymer Source Inc.) [20, 21] with a composition given by $B_{88}EO_{12}^{29.5}$. The subscripts denote the mass fraction in percent and the superscripts give the overall number average molecular weight of the block copolymer in kg/mol. The molecular weights of the PB and PEO blocks are 26 kg/mol and 3.5 kg/mol, respectively. The polydispersity index of the diblock copolymer is very small (1.06). The block copolymer has a melting temperature at 52^0C and a crystallization temperature at -30^0C in bulk as determined by DSC. The self-assembly of this block copolymer was studied by using a 1wt% $B_{88}EO_{12}^{29.5}$ solution in *n*-heptane. The solution was first kept at 70^0C for 30 min and then quenched to different crystallization temperatures: -30^0C (pathway A) and in liquid nitrogen (pathway B). After isothermal crystallization, the micellar solutions were brought to ambient temperature. After 24 hours transmission electron microscopy (TEM) and scanning force microscopy (SFM) was used to characterize the resulting morphologies.

The TEM micrographs were obtained on a Zeiss CEM 902 microscope operating at 80 kV. The samples were prepared by placing $2\mu l$ droplet of the 1 wt% $B_{88}EO_{12}^{29.5}$ solution onto a carbon-coated copper grid. The cryo-TEM was performed on a Zeiss 922 OMEGA EFTEM and operated at an acceleration voltage of 200 kV. The SFM experiments were performed using a Dimension 3100M microscope (Veeco Instruments) equipped with a Nanoscope software operated in TappingMode at room temperature. The samples were prepared by spin-coating the 1 wt% $B_{88}EO_{12}^{29.5}$ solution onto freshly cleaned silicon wafers. Scan rates between 0.5 - 1.0 Hz were used.

Dynamic light scattering was carried out on an ALV/DLS/SLS-5000 compact goniometer system equipped with a He-Ne laser (λ = 632.8 nm). All measurements were performed on 0.1 wt% solutions of $B_{88}EO_{12}^{29.5}$ in *n*-heptane at a scattering angle of 90^0 , where the resulting apparent hydrodynamic radius was determined via Stokes-Einstein relation.

The X-ray diffraction data were collected with Cu-K_α radiation (1.54) on a Bragg-Brentano-type diffractometer (Panalytical XPERT-PRO) quipped with a X′Celerator

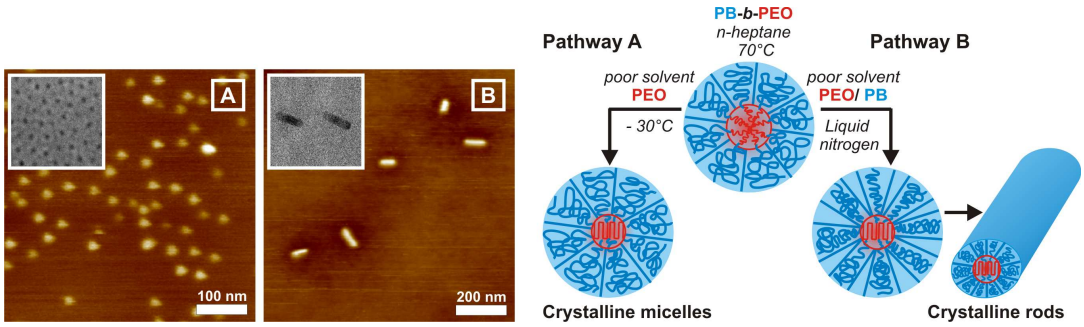

Figure 5.1: SFM phase contrast images of 0.1wt% solution of $B_{88}EO_{12}^{29.5}$ in *n*-heptane showing the morphologies formed by (A) quenching to -30^0C which leads to spherical micelles (pathway A) and (B) by quenching into liquid nitrogen leading to rod-like micelles (pathway B). The two insets represent the TEM micrographs of the two morphologies. The scales bare of the micrographs are identical with the ones of the corresponding SFM images. The SFM phase contrast images have a resolution of 256 x 256. The scheme represents both pathways and the reason for the different morphologies: The solvent *n*-heptane is a good solvent for the PB-chains down to temperatures of -30^0C. The PB-chains are highly swollen and the morphology with the highest curvature is the most stable one. *n*-Heptane must become a poor solvent for the PB block at much lower temperatures. The PB chain of the corona of the micelles will shrink and assume less space on the surface of the PEO-cores. Thus, a morphology with a smaller overall curvature, namely cylinders is formed.

Scientific RTMS detector. All the patterns were taken from 1wt% $B_{88}EO_{12}^{29.5}$ solutions applied on plane glass slides and dried at room temperature.

5.3 Results and discussion

The micellar morphologies discussed here have been generated by application of two thermal pathways: For pathway A solutions of the block copolymer were first kept at 70^0C for 30 min. Subsequently, they are quenched to -30^0C. For pathway B the solution were quenched from 70 ^0C by rapid immersion into liquid nitrogen (-196 ^0C). In the following we discuss the resulting morphologies:

Pathway A. For this pathway spherical micelles are formed in solution as shown by the SFM and TEM images in Fig. 5.1 (A). The solution was maintained for 24 hours at -30^0C to reach the maximum crystallinity. The micelles have an average diameter of 45.5 $\pm$ 4 nm and the film height was 20 nm. Similar values were obtained by the TEM micrographs where the micelles diameter was 48$\pm$ 5 nm. DLS at 70^0C revealed the presence of spherical micelles with a molten PEO core and an hydrodynamic radius R_H of 35 nm. Below 70^0C the solubility of *n*-heptane decreases for PEO block. However,

n-heptane remains a good solvent for the PB block at -30^0C. The crystalline spherical micelles have an R_H of 31.5 nm. The difference in size between the R_H value measured by DLS and the corresponding size in the SFM and TEM is due to the fact that the PB chains are fully stretched in *n*-heptane while SFM and TEM refers to the dried state. The spherical crystalline micelles are retaining the initial size as measured by R_H even after 6 months. No further evolution of the morphology was observed in these solutions.

Pathway B. Fig. 5.1 (B) shows the morphologies obtained through pathway B, namely, by quenching the hot solution from 70^0C into liquid nitrogen. Pathway B leads to the formation of rod-like micelles with a crystalline lamellar PEO core between the PB amorphous layers. The average length of the objects is 90 $\pm$ 20 nm from the SFM images and 90 $\pm$ 28 nm from the TEM micrographs. The height of the rods is 20 nm the width of which varied between 20 and 50 nm. DLS reveal an R_H of 38.5 nm.

The formation of rod-like structure can be rationalized by the concept of the packing parameter introduced by Israelachvili [22]. The main point is illustrated in Fig. 5.1: The solvent *n*-heptane is a good solvent for the PB-chains down to temperatures of -30^0C. Hence, the PB-chains are highly swollen and space-filling. Thus, the morphology with the highest curvature is the most stable one under these conditions. However, at much lower temperatures *n*-heptane must finally become a poor solvent for the PB block as can be argued from first principles [23]. Therefore the PB chain of the corona micelles will shrink and assume less space on the surface of the PEO-cores. As a consequence of this, spherical micelles become unstable and a morphology with a smaller overall curvature, namely cylinders are formed. The deterioration of the solvent quality is instantaneous and we presume that the coagulation of the now unstable micelles presents a rapid process. Then crystallization of the PEO block is sets in and the micellar core become solid. The freezing point of *n*-heptane is at -90.6^0C and once the solvent is frozen no further rearrangement of the micelles can occur. Hence, the temperature-induced conformational changes must occur somewhere between -30 and -90^0C in the solution. Thus the rod-like structure is fixed by crystallization in the solution and the rod-like shape is therefore preserved when the solution is warmed up to ambient temperature.

These findings are in full accord with Monte Carlo simulations of the self-assembly of amphiphilic diblock copolymers in a selective solvent [24]. These simulations demonstrate that the morphologies of A-*b*-B diblock copolymers in solution strongly depend on the length of corona-forming segments. With decreasing corona-forming segments the transition of spherical micelles to rod-like aggregates occurs. This is also well borne out from the experimental results observed by different groups [25, 26, 27, 28, 29]. However,

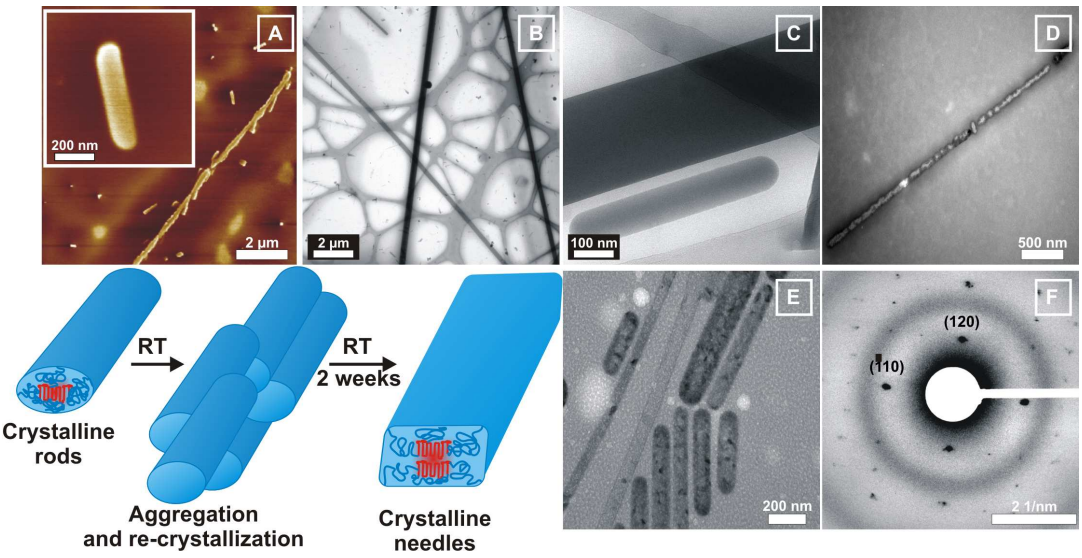

Figure 5.2: Assembly of the rod-like micelles at room temperature to needles after two weeks (A) shown by SFM phase contrast image of needle and rod-like micelles. (B) and (C): Cryogenic TEM (cryo-TEM) images of the needle-like morphology developed in solution. (D): TEM micrograph of needle-like morphology after staining with OsO_4 vapor for 60 seconds. The darker areas correspond to stained PB domains detected along the PEO crystalline domains. (E): TEM image indicating the coexistence of rods and needles with different lengths. (F): Selected area diffraction pattern of needle-like structure illustrating the reflections of the semi-crystalline PEO block. The schematic representation shows the proposed mechanism of morphological changes of the rod-like micelles in *n*-heptane at ambient temperature with time.

here we demonstrate for the first time that this transition can be brought about in a semicrystalline block copolymer solely by a change of temperature, not by a change of the block length.

In the following we shall discuss further structural changes that occur after several weeks in the solution. The rod-like micelles formed through pathway B rearrange with time when brought to room temperature. After two weeks, the rod-like micelles have aggregated to form needle-like structure as can be seen in Fig. 5.2. Obviously the needles grow on the expense of rod-like micelles by fusion or coalescence as their initial population was observed to decrease with time. Moreover, the solutions became turbid during this time. This indicates the formation of larger objects in the solution.

The rod-like micelles aggregate and form objects up to a length of 550 nm. The widths are varying between 60 to 100 nm. Coexistence of the rod-like and needle-like structures with heights of 40 and 150 nm can be seen in the SFM phase contrast image (Fig. 5.2 (A)). Figure Fig. 5.2 (B) shows the needle-like micelles grown in solution, where the samples were prepared by *in situ* freeze-drying cryo-TEM as describe elsewhere [19]. The

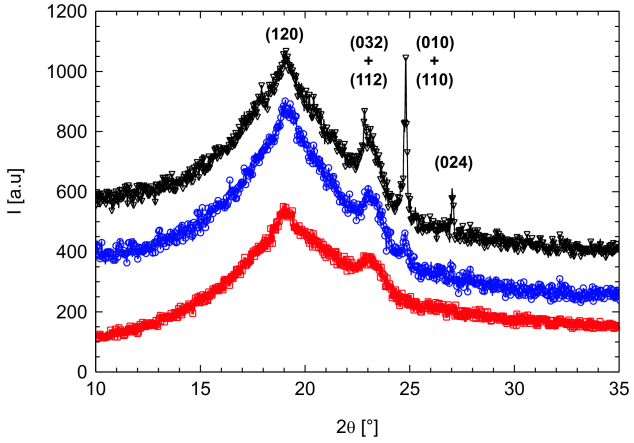

Figure 5.3: Crystallinity of the micelles: XRD pattern of a film of 1wt% $B_{88}EO_{12}^{29.5}$ solution in *n*-heptane corresponding to the spherical micelles (blue line), rod-like micelles (red line) and needle-like morphology (black line). The XRD patterns were shifted along the ordinate for a better visualization.

needles have lengths up to 30μm and the widths are ranging from 50 to 550 nm. Fig. 5.2 (C) was taken at a lower magnification for a better visualization of the needle-like and rod-like structure. Fig. 5.2 (E) represent the TEM micrograph taken at ambient temperature where rods and needle-like micelles of different lengths and widths can be seen.

Selective staining of the PB domains with OsO_4 vapor for 60 seconds was used to obtain closer insight into the needle morphology where individual rods units that aggregate into the solution can be observed (see Fig. 5.2 (D)). The crystalline PEO domains appear brighter because of the preferential staining of the PB block. DLS experiments carried out on solutions of the rod-like micelles after two weeks at room temperature confirmed the formation of larger objects (see Fig. 5.2). Selected area diffraction pattern of needle morphology was carried out at ambient temperature as illustrated in the inverted contrast micrograph in Fig. 5.2 (F). The crystalline reflections of PEO can be clearly observed. XRD measurements corroborated these results taken from TEM micrographs. In Fig. 5.3 the reflections at $2\Theta = 19^0$, 23^0, 25^0, 27^0 revealed crystallization of PEO in its triclinic modification for all the morphologies. The diffraction pattern are attributed to (120),(032+112),(010+ $\bar{1}$10) and (024) PEO reflections [30].

In the case of the needle morphology the reflex position at $2\Theta = 25^0$ is very intense and could be visualized in the SAED TEM micrograph as the overlapping (010+ $\bar{1}$10) reflections together with the two other reflections along the vertical on the first ring identified as (120) (see Fig. 5.2 (F)). The degree of crystallinity was estimated from the

XRD patterns as the ratio between the areas below the crystalline Bragg peaks to the total scattered area [31]. We found that the crystallinity of the needle-like morphology is higher as one of the rod-like micelles: The spherical micelles have a crystallinity of 7.9%. The initial crystallinity of the rod-like micelles was 4.8% and increased to 9% in case of the needle-like morphology. Moreover, the growth of the needle-like structures hints to a prefered direction of the crystalline growth of the PEO along the long axis. Most probably, this prefered direction is already generated in the early stage of rod formation. This clearly points to the importance of crystallinity in determining the micellar morphology. The low PEO crystallinity of the rods may be responsible for the rearrangements and recrystallization at room temperature. It seems that the rapid morphological transition from spherical to rod-like micelles leaves some PEO exposed in the rods as compared to the much better crystallized spherical micelles. Thus, there is a stronger tendency for the rods to thicken and recrystallize leading to more stable structures. A similar growth mechanism was observed by Winnik, Manners and coworkers in their systems where a driven crystallization process occurs in solution [18].

5.4 Conclusion

In conclusion, we demonstrated that different crystalline architectures were obtained by a marked lowering of the temperature. The low temperature turned out to be the decisive factor in as much it determines the micellar morphology as indicated in Fig. 5.1 and Fig. 5.2: When the hot solution is cooled down to -30^0C (pathway A) spherical micelles are formed. In case of pathway B, that is, by undercooling to the temperature of liquid nitrogen, rod-like micelles are formed. In both cases the shape of the liquid micelles is dictated by packing arguments as shown schematically in Figure 1. Crystallization then serves for freezing in the resulting spherical (pathway A) or rod-like (pathway B) morphologies. The rod-like micelles are metastable in solution and a further morphological transition to a needle-like morphology was observed with time.

Acknowledgments

Financial support by the Deutsche Forschungsgemeinsschaft, SFB 481, Bayreuth, is gratefully acknowledged. The authors thank Dr. Günther Jutz and Carmen Kunert for the TEM investigation. A.M.M. acknowledge the financial support from the European Community's "Marie-Curie Actions" under Contract No. MRTN-CT-2004-504052 [POLYFILM].

Bibliography

[1] Y. L. Loo, R. A. Register, and A. J. Ryan. *Macromolecules*, 35:2365–2374, 2002.

[2] D. Richter, D. Schneiders, M. Monkenbusch, L. Willner, L. J. Fetters, J. S. Huang, M. Lin, K. Mortensen, and B. Farago. *Macromolecules*, 30:1053–1068, 1997.

[3] J. T. Xu, J. P. A. Fairclough, S. M. Mai, and A. J. Ryan. *J. Mater. Chem.*, 13:2740–2748, 2003.

[4] Z. X. Du, J. T. Xu, and Z. Q. Fan. *Macromol. Rapid Commun.*, 29:467–471, 2008.

[5] T. Vilgis and A. Halperin. *Macromolecules*, 24:2090–2095, 1991.

[6] B. Lotz and A. J. Kovacs. *Kolloid Z.Z.Polym.*, 209:97–114, 1966.

[7] M. Droescher and T. L. Smith. *Macromolecules*, 15:442–449, 1982.

[8] E. K. Lin and A. P. Gast. *Macromolecules*, 29:4432–4441, 1996.

[9] T. Kawai, S. Shiozaki, S. Sonoda, H. Nakagawa, T. Matsumoto, and H. Maeda. *Makromol. Chem.*, 128:252–262, 1969.

[10] B. Lotz, A. J. Kovacs, G. A. Bassett, and A. Keller. *Kolloid Z.Z.Polym.*, 209:115–128, 1966.

[11] A. P. Gast, P. K. Vinson, and K. A. Coganfarinas. *Macromolecules*, 26:1774–1776, 1993.

[12] K. A. Cogan and A. P. Gast. *Macromolecules*, 23:745–753, 1990.

[13] J. T. Xu, W. Jin, G. D. Liang, and Z. Q. Fan. *Polymer*, 46:1709–1716, 2005.

[14] L. Shen, H. Wang, G. Guerin, C. Wu, I. Manners, and M.A Winnik. *Macromolecules*, 41:4380–4389, 2008.

[15] J. Raez, I. Manners, and M. A. Winnik. *Langmuir*, 18:7229–7239, 2002.

[16] J. Raez, J. P. Tomba, I. Manners, and M. A. Winnik. *J. Am. Chem. Soc.*, 125:9546–9547, 2003.

[17] X. Wang, H. Wang, D. J. Frankowski, P. G. Lam, P. M. Welch, M. A. Winnik, J. Hartmann, I. Manners, and R. J. Spontak. *Adv. Mater.*, 19:2279 – 2285, 2007.

[18] T. Gädt, N. S. Ieong, G. Cambridge, Winnik M. A., and Manners I. *Nat. Mater.*, 8:144 – 150, 2009.

[19] A. M. Mihut, A. Chiche, M. Drechsler, H. Schmalz, E. Di Cola, G. Krausch, and M. Ballauff. *Soft Matter*, 5:208–213, 2009.

[20] S. Fröster and E. Krämer. *Macromolecules*, 32:2783–2785, 1999.

[21] M. A. Hillmyer and F. S. Bates. *Macromolecules*, 29:6994–7002, 1996.

[22] J. N. Israelachvili. *Intermolecular and Surface Forces*. Academic Press San Diego, 2nd edition, 1992.

[23] P. J. Flory. *Principle of Polymer Chemistry*. Cornell University Press, Ithaca, 1953.

[24] X. He, H. Liang, and C. Pan. *Phys. Rev E*, 63:031804–1 – 031804–1, 2001.

[25] L. Zhang and A. Eisenberg. *Science*, 268:1728 – 1731, 1995.

[26] L. Zhang and A. Eisenberg. *Macromolecules*, 32:2239 – 2249, 1999.

[27] K. Yu and A. Eisenberg. *Macromolecules*, 31:3509 – 3518, 1998.

[28] K. Yu and A. Eisenberg. *Macromolecules*, 31:9399 – 9402, 1998.

[29] S. Jain and F. S. Bates. *Science*, 300:460 – 464, 2003.

[30] Y. Takahashi, I. Sumita, and H. Tadokoro. *J. Polym. Sci., Part B: Polym. Phys.*, 11:2113–2122, 1973.

[31] C. G. Vonk. *J. Appl. Crystallogr.*, 6:148–152, 1973.

CHAPTER 6

Block Copolymers Assembly in Solution via Kinetic Crystallization Control: Morphological Phase Diagram

Abstract
We have investigated the phase diagram of solution morphologies as a function of the molecular composition of the semicrystalline poly(butadiene)-*b*-poly(ethylene oxide)(PB-*b*-PEO) block copolymers. The structures have been quenched from a selective solvent condition (70^{o}C in *n*-heptane) following two thermal pathways: (A) by direct immersion into liquid nitrogen and (B) by quenching to the crystallization temperature of the PEO block. Pathway A allowed morphological transitions from spheres to rods, worms or twisted cylinders with the increase of the crystalline content of the PEO core. In Pathway B, the sequence of spheres, cylinders, lamellae, platelets and dendrites structures is observed with the increases of the PEO block length. SFM and TEM allowed imaging of the crystalline morphologies, whereas the hydrodynamic radii of the micelles in solution were investigated by dynamic light scattering (DLS). The crystallization of the PEO core was confirmed by selected area electron diffraction (SAED) and X-ray diffraction (XRD).

The results of this chapter will be submitted as:

Block Copolymers Assembly in Solution via Kinetic Crystallization Control: Morphological Phase Diagram
by Adriana M. Mihut, Jérôme J. Crassous, Holger Schmalz, Markus Drechsler and Matthias Ballauff.

6.1 Introduction

Self-assembly behavior of semicrystalline block copolymers in selective solvent is of great interest due to the rich variety in resulting crystalline structures. The versatile morphological behavior is affected by the interplay between the solvent-core interface energy and the repulsion between the swollen corona chains. In essence, the self-assembled morphologies can be viewed as sandwich- like structures consisting of chain-folded crystalline core domains coated with swollen amorphous layers on both sides [1, 2, 3, 4]. Alteration in the block copolymers composition, concentration and solvent selectivity as reported by few research groups, leads to different morphologies formation like spheres or spherical aggregates [5, 6, 7], cylinders (depending on their flexibility, these structures are refereed to as rod-like or worm-like micelles) [8, 9, 10, 11, 12, 13, 14, 15], and lamellar structures [2, 16, 17]. Morphological transitions caused by changes of solvent quality or by the variation of block lengths have been observed. Winnik and co-workers reported structures of PFS-*b*-PDMS block copolymer under varying solvent conditions [18]. Moreover, these authors have shown that micellar morphologies with cylinder-cylinder and platelet-cylinder connections are formed by epitaxial crystallization of PI-*b*-PSF diblock copolymers, and the length of the micelles is controlled by the addition of the PFS block-copolymer unimers acting as micellar seeds [17]. Xu and co-workers demonstrated that the micellar morphologies formed by the PCL-b-PEO block copolymers in aqueous medium, depend on the lengths of the PCL crystalline block [13].

The temperature of the system represents another approach to control the crystalline morphology, as well as kinetic pathways of crystallization [19, 20, 21]. For a symmetric poly(butadiene)-*b*-poly(ethylene oxide) block copolymer ($B_{52}EO_{48}$) in selective solvent (*n*-heptane), the spherical morphology is retained after a fast quenching into liquid nitrogen. If the solution was kept at a crystallization temperature of 30^oC, the competition between the crystallization and the aggregation of the spherical micellar units lead to a meander-like structure [19]. A detailed investigation of the formation mechanism of the crystals through micellar aggregation demonstrated that the nucleation and growth of the PEO core dictates the resulting morphology [21]. Moreover, in the case of a highly asymmetric PB-*b*-PEO block copolymer ($B_{88}EO_{12}$) we observed rod-like micelles. With time these rod-like micelles aggregate and re-crystallize in solution forming long needles [20].

The above studies demonstrated that the PB-*b*-PEO block copolymers are a promising system models for developing a general route towards tunable crystalline morphologies.

The main goal of the present investigation is to establish the relationship between the major parameters that govern morphological development from a selective solvent as a function of the crystallization temperature, defined by the length of the PEO block, and of the overall length of the block copolymers. The morphologies were generated from the hot polymer solutions via two routes: by immersion into liquid nitrogen (Pathway A) and by quenching to the crystallization temperature of the PEO block (Pathway B). The corresponding morphological characterization in the dried state was carried out by scanning force microscopy (SFM) and transmission electron microscopy (TEM). Cryogenic transmission electron microscopy (cryo-TEM) allowed the direct visualization of the structures formed in solution. In addition, dynamic light scattering experiments brought information about the hydrodynamic radius of the micelles. Selected area electron diffraction (SAED) and X-ray diffraction (XRD) were employed to highlight the crystalline nature of the structures generated though districted thermal pathways.

6.2 Experimental Part

Materials. The poly (butadiene)-*block*-poly(ethylene oxide) diblock copolymers with a composition given by B_xEO_y were purchased from Polymer Source Inc. [22, 23]. The subscripts denote the mass fraction in percent of the PB (x), respectively of the PEO block (y). Molecular characteristics of the diblock copolymers such as the number average molecular weights of PB blocks and PEO blocks M_{PB} and M_{PEO}, the overall number average molecular weight of the block copolymer M_n in kg/mol, the polydispersity (PDI), the weight fraction of the PEO blocks w_{PEO} and the degree of polymerization of PB and PEO blocks, N_{PB}, respectively N_{PEO} are listed in Table. 6.1. The crystallization/ melting temperatures of the bulk determined by DSC are summarized as well. The $B_{52}EO_{48}$ diblock copolymer was synthesized via sequential anionic polymerization as described in a previous study [19]. The samples prepared from 1 wt% *n*-heptane solutions were first kept at 70 ^0C for 30 min and then quenched via the two pathways. If lower concentrations were required, the stock solutions were diluted accordingly.

Scanning Force Microscopy (SFM). The SFM experiments were performed using a Dimension 3100M microscope (Veeco Instruments) equipped with a Nanoscope software operated in TappingMode at room temperature. The samples were prepared by spin-coating the 0.1 wt% *n*-heptane solutions solution onto freshly cleaned silicon wafers. Scan rates between 0.5 - 1.0 Hz were used. The crystalline PEO block is much stiffer then the amorphous PB block which allowed us an imaging mode base on a mechanical

Table 6.1: Characteristics of diblock copolymers

Name	M_{PB}	M_{PEO}	M_n	PDI	w_{PEO}	T_c	T_m	N_{PEO}	N_{PB}
$B_{88}EO_{12}$	26.0	3.5	29.5	1.06	0.12	-30	52	80	481
$B_{80}EO_{20}$	11.8	2.9	14.7	1.09	0.2	-27	45	66	219
$B_{78}EO_{22}$	26.0	7.5	33.5	1.06	0.22	-19	57	170	481
$B_{68}EO_{32}$	5.0	2.3	7.3	1.06	0.32	30	47	52	93
$B_{62}EO_{38}$	6.5	3.9	10.4	1.10	0.38	25	48	89	120
$B_{53}EO_{47}$	5.5	5.0	10.5	1.05	0.47	43	60	114	102
$B_{52}EO_{48}$	2.9	2.7	5.6	1.02	0.48	32	47	61	54
$B_{42}EO_{58}$	5.7	8.0	13.7	1.05	0.58	37	51	182	106
$B_{31}EO_{69}$	3.5	7.8	11.3	1.08	0.69	50	62	177	65

contrast, complementary to the topographic imaging mode.

Transmission Electron Microscopy (TEM). Samples were prepared by placing a drop of the polymers solution (0.1wt% in *n*-heptane) on a carbon-coated copper grid. After few seconds, excess solution was removed by blotting with filter paper. Staining was performed with OsO_4 vapor for 60s. OsO_4 is known to selectively stain PB; i.e., PB domains are expected to appear darker compared to PEO domains, which enables to distinguish between the two polymers. Subsequently, bright-field TEM was performed on a Zeiss CEM 902 operating at 80 kV.

Cryogenic Transmission Electron Microscopy (cryo-TEM). The samples were prepared by adding a $2\mu l$ droplet of a 1wt% polymers solution in *n*-heptane on a lacey carbon coated copper grid. The specimens were prepared by vitrification in liquid nitrogen and then cooled to approximately 77K in a temperature controlled freezing unit (Zeiss Cryobox, Zeiss NTS GmbH, Oberkochen, Germany). After freezing the specimen was placed into a cryo-transfer holder (CT 3500, Gatan, München, Germany) and transferred to a Zeiss 922 OMEGA EFTEM (Zeiss NTS GmbH, Oberkochen, Germany). The samples were cooled to 97K for image recording. The TEM was operated at an acceleration voltage of 200 kV.

X-ray diffraction (XRD). The X-ray diffraction data were collected with Cu-K_α radiation (1.54) on a Bragg-Brentano-type diffractometer (Panalytical XPERT-PRO) quipped with a X′ Celerator Scientific RTMS detector. The XRD patterns were recorded in the 2θ range from 10 to 40^0. All the patterns were taken from 1wt% B_xEO_y solutions dried at room temperature on glass slides. WAXS experiments were carried out on the polymer solutions at the ID2 beam lime at the European Synchrotron Radiation Facilities (ESRF, Grenoble, France). The operating wavelength of the X-ray was $\lambda =$ 0.1 nm. A Linkam THMS600 temperature controller system was used as a sample holder.

Dynamic Light Scattering (DLS). The experiments were carried out on an ALV-5000 compact goniometer system equipped with a He-Ne laser ($\lambda = 632.8$ nm). All measurements were performed on 0.1 wt% solutions of B_xEO_y in *n*-heptane at a scattering angle of 90^0 , where the resulting apparent hydrodynamic radius was determined via the Stokes-Einstein relation.

6.3 Results and discussion

6.3.1 Change of morphology with thermal pathways

The crystalline micellar morphologies discussed here have been generated from the hot solutions (70^0C, that is, above the melting temperature of the PEO block) via two thermal pathways: (A) by direct immersion liquid nitrogen, where *n*-heptane becomes a poor solvent for both blocks at very low temperatures, and (B) by quenching to the crystallization temperature of the PEO, i.e., determined by the length of PEO block (Table. 6.1). In this pathway *n*-heptane is a poor solvent only for the PEO block. At 70^oC the block copolymers self-assembled into micellar structures consisting of a PEO molten core and a soluble PB corona. In the following we discuss the resulting morphologies upon cooling.

6.3.2 Pathway A: Morphological Self-Assembly at Low Crystallization Temperature

Fig. 6.1 shows the SFM phase images of the morphologies of B_xEO_y block copolymers formed via pathway A in *n*-heptane. The bright areas correspond to the hard PEO block surrounded by the soft PB layers (appears as darker areas in phase images). While the SFM measurements provide information about the sizes of the dried micelles with a collapse coronar chains, DLS allows to determine the hydrodynamic radius R_H of the micelles with fully stretched PB chains in *n*-heptane (Table. 6.2).

At a weight fraction of w_{PEO} of 12%, rod-like micelles are formed upon cooling (Fig. 6.1 (A)), whereas an increase of the w_{PEO} between 20% and 48% leads to the formation of spherical micelles with dimensions ranging from 25 nm to 43.5 nm (Tabel. 6.2). For the symmetric $B_{52}EO_{48}$ (w_{PEO}= 0.48) block copolymer, a fast quenching in liquid nitrogen retained the spherical shape present in the molten state at 70^0C (Fig. 6.1 (G)) [19], whereas in the case of the highly asymmetric $B_{88}EO_{12}$ (w_{PEO}= 0.12) block copolymer, a transition from spheres to rods was reported due to a decrease of the solvent quality for

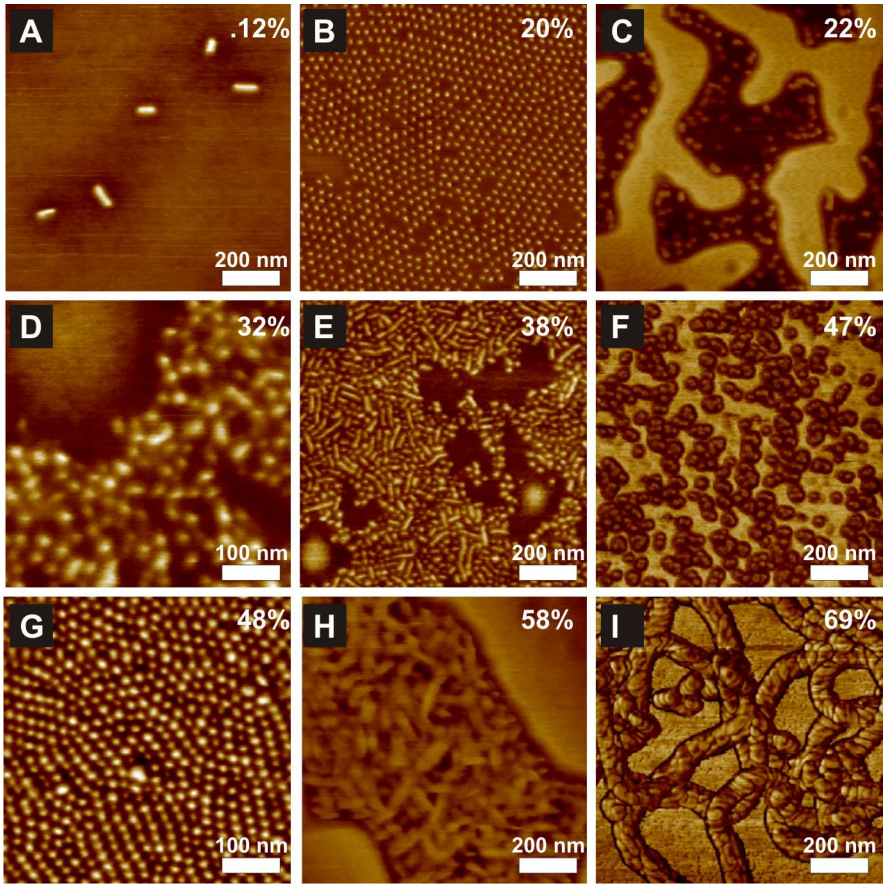

Figure 6.1: Pathway A: SFM phase contrast images of crystalline micellar morphologies of B_xEO_y block copolymers in *n*-heptane after immersion into liquid nitrogen of the 0.1 wt% polymer solutions from 70^0C: (A) $B_{88}EO_{12}$: rods; (B) $B_{80}EO_{20}$: spheres; (C) $B_{78}EO_{22}$: spheres; (D) $B_{68}EO_{32}$: spheres; (E) $B_{62}EO_{38}$: cylinders; (F) $B_{53}EO_{47}$: spheres;(G) $B_{52}EO_{48}$: spheres; (H) $B_{42}EO_{58}$: spheres and worms; and (I) $B_{31}EO_{69}$: branched cylinders. The weight fraction of the PEO block is indicated for guidance.

PB coronar chains at very low temperatures (Fig. 6.1 (A)) [20]. The rod micelles had lengths of 90 ± 20 nm. These structures are not at equilibrium and with time rearranged into long needles.

Rod-like micelles are formed in solution at a weight fraction of w_{PEO}= 0.38 (Fig. 6.1 (E)). The rods were typically short, with length of 78± 7 nm and diameters of 26± 3 nm. DLS revealed a R_H of 89 nm. The morphology present in the molten state was retained after a quenching into liquid nitrogen as DLS indicated at 70^0C, the presence of micelles with a R_H of 98 nm.

By increasing the weight fraction of the PEO block a transition from spheres to cylindrical micelles was observed. At w_{PEO}= 0.58, short worm-like micelles with an average length of 50± 10 nm and a width of 26± 4 nm (Fig. 6.1 (H)) coexist with spherical mi-

Name	Pathway A			Pathway B		
	Morphology	R_H^{DLS}	D^{SFM}	Morphology	R_H^{DLS}	D^{SFM}
$B_{88}EO_{12}$	R	38.50	90 ± 20[a]	S	31.5	45.5 ±4
$B_{80}EO_{20}$	S	22	34± 3	S	23	33.5±4
$B_{78}EO_{22}$	S	36.5	39± 5	S	34.5	42±5
$B_{68}EO_{32}$	S	28	42± 5	P	-	5500±4000
$B_{62}EO_{38}$	R	89	78±7[a], 26±3[b]	C, P	-	35±2[b], 5750±2000
$B_{53}EO_{47}$	S	23	43.55±5	L, P	-	107±27[b], 204±50
$B_{52}EO_{48}$	S	18	25±2	BL	115	40±4[b]
$B_{42}EO_{58}$	S, W	28	50±10[a], 26±4[b]	P	-	372±96[a],280±70[b]
$B_{31}EO_{69}$	BC	-	128±24[b]	D	-	81±8[b]

Table 6.2: Micellar Sizes of PB-*b*-PEO Block Copolymers. The hydrodynamic radius R_H measured by DLS and the average sizes measured by SFM where [a] is the length and [b] the width of the structure are summarized. The observed basic morphologies are spheres (S), rods (R), worms (W), cylinders (C), twist cylinders (BC), lamellae (L), branched lamellae (BL), platelets (P) and dendrites (D).

celles. The worm-like micelles are the predominant morphologies at this weight fraction. Twisted cylinders formed at w_{PEO}= 0.69 (Fig. 6.1 (I)). These cylindrical micelles had an average width of 81± 9 nm with a height of 32 nm. We could not obtain an average length due to the limited size of the images; however, lengths in excess of 5 μm were observed. Best to our knowledge this kind of bent cylinders have been observed for the first time for block copolymers which contains a crystalline PEO block in solution.

6.3.3 Pathway B: Morphological Self-Assembly at the Crystallization Temperature of the PEO Block

Fig. 6.2 shows the SFM images of the morphologies obtained from pathway B, that is, by direct quenching of the hot solutions to the crystallization temperature of the PEO block. Spherical micelles were obtained for smaller weight fractions of PEO ($w_{PEO} \leq$ 0.32) in the copolymers (Fig. 6.2 (A-C)). The spheres had diameters ranging from 45.5 ± 4nm to 42±5 nm (Table. 6.2).

Increasing the weight fraction of w_{PEO} to 32% and 38% square platelet-like structures are formed. The platelets had an overall diameter of the 5.5± 4 μm (Fig. 6.2 (D)). Coexistence of platelets with cylindrical micelles was observed at w_{PEO}= 0.38 (Fig. 6.2 (E)). The cylinders had diameters of 35± 2 nm, whereas the platelets average size was 5.75± 2 μm.

The lamellar morphologies coexist at w_{PEO}= 0.47 with small platelets (Fig. 6.2 (F)).

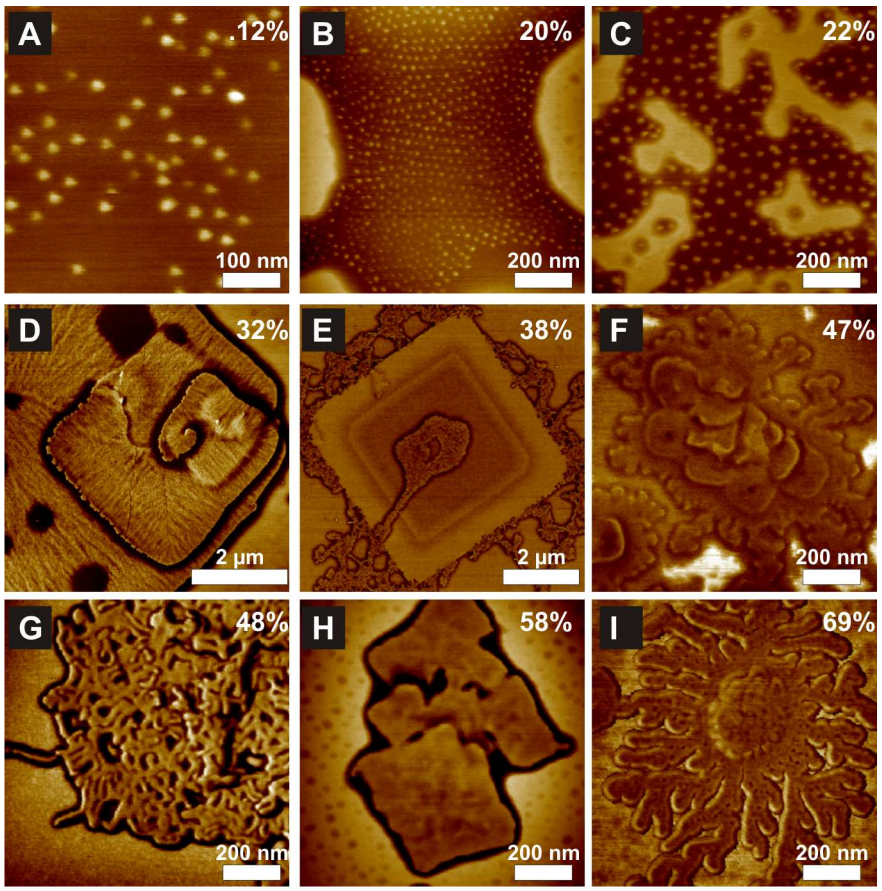

Figure 6.2: Pathway B: SFM phase contrast images of crystalline morphologies formed in *n*-heptane at the crystallization temperature of the PEO block from 0.1 wt% polymer solutions: (A) $B_{88}EO_{12}$: spheres; (B) $B_{80}EO_{20}$: spheres; (C) $B_{78}EO_{22}$: spheres; (D) $B_{68}EO_{32}$: platelets; (E) $B_{62}EO_{38}$: coexistence of cylinders and platelets; (F) $B_{53}EO_{47}$: coexistence of lamellae and platelets; (G) $B_{52}EO_{48}$: meander-like (lamellae); (H) $B_{42}EO_{58}$: platelets and (I) $B_{31}EO_{69}$: dendrites structures. The weight fraction of the PEO block is indicated for guidance.

The average widths of the lamellae was estimated to be 107± 27 nm, whereas the average size of the platelets was 204± 50 nm. Meander-like structure containing a ribbon-like PEO core formed at w_{PEO}= 0.48 (Fig. 6.2(G)). The width of the meanders was found to be rather uniform 40 ± 4 nm and the length distribution of the branches is ranging from 35 nm to 300 nm [19, 21]. A morphological transition from branched lamellae to platelets (Fig. 6.2 (H -I)) and dendritic-like structures (Fig. 6.2 (I)) occurred when w_{PEO} is increased to 0.58 and 0.69, respectively.

It can be seen that an increase in the PEO block composition yielded morphological transitions from spheres to lamellae or platelet-like structures. Therefore, the lengths of the PEO and PB blocks have an important effect on the micellar morphology. A remark-

able aspect disclosed by our SFM imaging is the coexistence of different morphologies, and can be inferred that the morphological boundaries are influenced by the molecular weight distribution of the copolymer. This behavior was found in the PEO composition ranges where the spheres/platelets and platelets/ branched lamellae boundaries are located (w_{PEO}: 0.22- 0.32 and 0.47-0.48).

Morphological coexistence. The detailed discussion of the structure in the coexistence regions and the comparison between the morphologies formed upon cooling via the two thermal pathways, at the same w_{PEO} composition, will be given in context of the TEM results (Fig. 6.3). Selective staining of the samples with osmium tetroxide, which reacts only with the PB chains, generated a characteristic contrast between the two polymers confirming that the PB chains (dark areas) constitute the corona of the micellar morphologies. Pathway A generally retained the melt morphology, whereas the quenching of the polymer solutions at the crystallization temperature (T_c) of the PEO block (pathway B) induced structural changes. At weight fractions of the PEO block < 0.32, the spherical shape present in the molten state is retained upon cooling via the two thermal pathways. Rod- like micelles are formed for the $B_{62}EO_{38}$ block copolymer ($w_{PEO}= 0.38$) after quenching in liquid nitrogen, whereas pathway B ($T_c= 25^0C$) leads to the formation of cylinders and platelets structures (Fig. 6.3 (A-B)). Above $w_{PEO} \geq 0.32$, crystallization breakout the melt morphology via pathway B and leads to larger morphologies formation.

Crystallization at T_c yielded morphological transitions from spherical micelles to lamellar structure at weight fractions of 47 and 48%, respectively. The $B_{53}EO_{47}$ block copolymer self-assembled into lamellae and platelet-like structures (Fig. 6.3 D), whereas the $B_{52}EO_{48}$ block copolymer formed branched lamellae reported as meanders in our previous studies (Fig. 6.3 F) [19, 21]. The meander structure formed via crystallization-induced aggregation of spherical micelles upon cooling at 30^0C.

The worm-like micelles formed at $w_{PEO} \geq 0.58$ are retained after immersion into liquid nitrogen, whereas pathway B leads to the formation of square platelets (Fig. 6.3 (H)) and dendritical-like structure (Fig. 6.3 (J)). The values of the structures revealed by TEM are consistent with the results obtained from SFM.

Fig. 6.4 summarizes the morphological behavior of the PB-*b*-PEO block copolymers upon cooling at the crystallization temperature T_c. The length of the PEO block affects the crystallization temperature (see Table. 6.1). At low T_c (small weight fractions of the PEO block) spherical micelles are formed upon cooling, whereas the block copolymers with larger PEO composition, i.e., higher T_c, favored development of larger morphologies

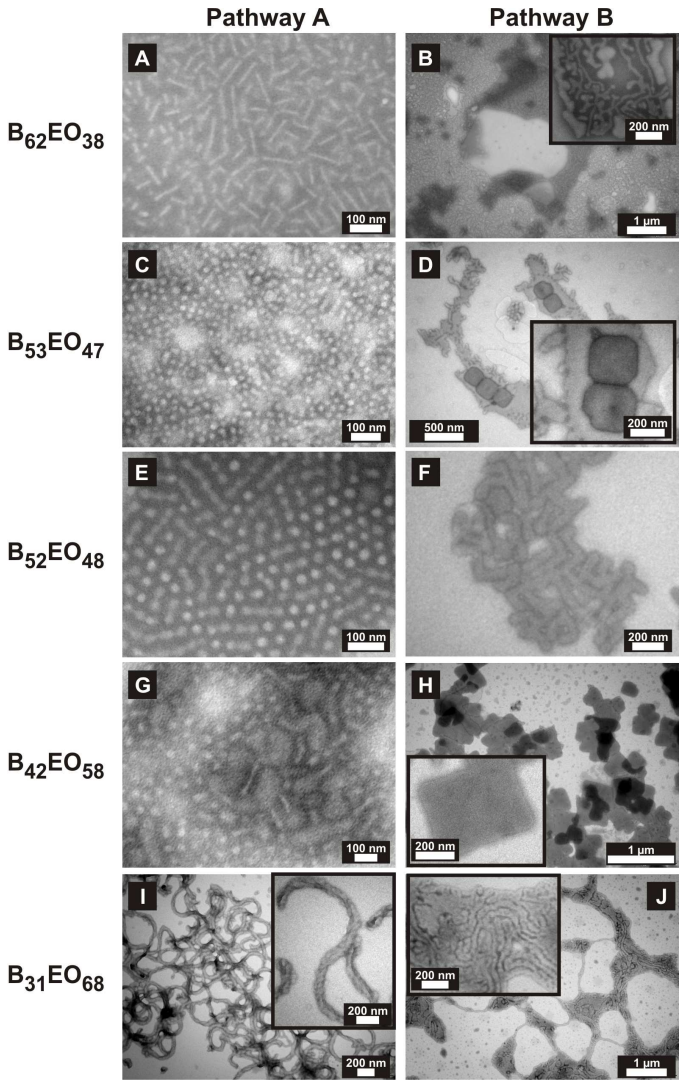

Figure 6.3: TEM micrographs of morphologies of the B_xEO_y block copolymers in *n*-heptane formed by pathway A and B: $B_{62}EO_{38}$: (A) rods;(B) coexistence of cylinders and platelets; $B_{53}EO_{47}$: (C) spheres; (D) coexistence of lamellae and platelets; $B_{52}EO_{48}$: (E) spheres; (F) branched lamellae; $B_{42}EO_{58}$: (G) spheres and worms; (H) platelets; $B_{31}EO_{69}$: (I) branched cylinders; (J) dendrites.

as lamellae and platelets.

This can be qualitatively explain by the Halperin and Vilgis theory [4]. When the amorphous block is longer and has a large contribution to the overall free energy, spherical micelles rather then lamellae micelles tend to be formed. The free energy of a semicrystalline block copolymer consists of three parts: the enthalpy of fusion of the crystalline block, the conformational entropy of the amorphous block, and the interfacial energy. The geometry of the micelles is determined by the balance between the

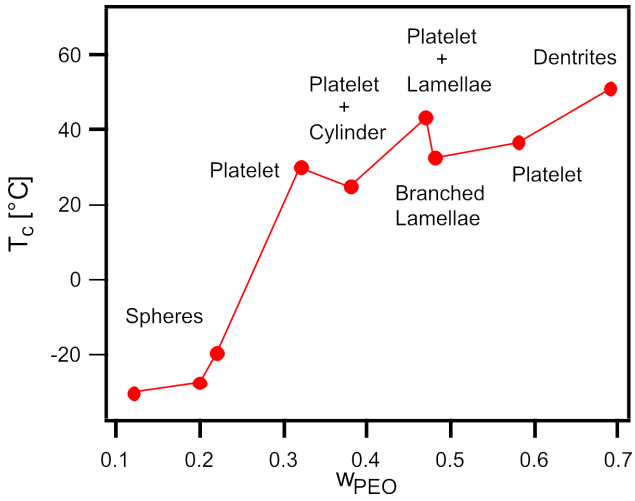

Figure 6.4: Experimentally determined correlation between the crystallization temperature and the molecular composition of the trend morphology obtained from pathway B. Coexistence behaviors were observed in the ranges between w_{PEO}: 0.38- 0.47.

interfacial energy between the solvent and the core surface, and the stretching within the swollen coils of the corona. All these components are depended on the chain folding of the crystalline block. With increasing the length of the crystalline block (therefore, the T_c), the folding number of PEO increase, and thus the area occupied by each PB chain becomes larger, leading to decrease in the crowding of the PB chains, and spherical micelles are transformed into cylinders or lamellar structures.

Dimension of the crystals. Due to the complexity of the crystalline morphologies different parameters that can influence the self- assembly mechanism will be discussed in the following. In order to understand how the chain folding evolves with the length of the PEO block, the overall thickness average (H) of the PB-*b*-PEO lamellar crystals has been determined from the SFM images. Fig. 6.5 shows the thickness evolution with the weight fraction of the PEO block. To calculate the thickness of the PEO, the first assumption we made is that the density of the PEO block is identical to that of the crystalline bulk density (ρ_{PEO}= 1.239 g/ cm^3), where the density of the amorphous PB is ρ_{PB}= 0.884 g/ cm^3. The micellar platelets appear as a crystal core grafted with solvent-swollen coronae at both sides [2, 4]. The lamellar thickness (H) is the sum of the corona thickness (d_{PB}) and the core thickness (d_{PEO}), i.e., H= 2d_{PB}+ d_{PEO}. The d_{PEO}= H*V_{PEO} and can be calculated using the expression:

$$d_{PEO} = H\frac{M_{PEO}/\rho_{PEO}}{M_{PEO}/\rho_{PEO} + M_{PB}/\rho_{PB}} \tag{6.1}$$

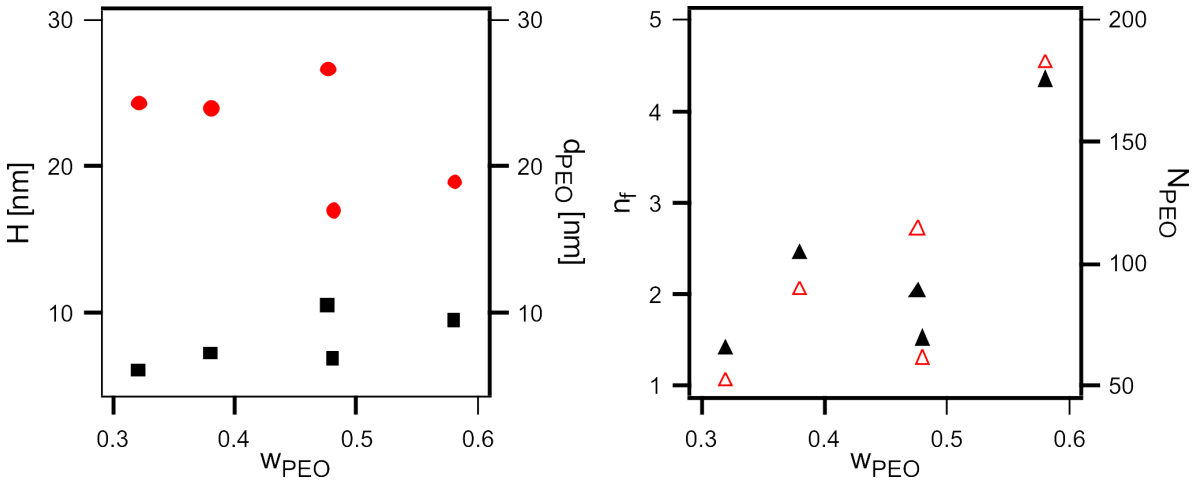

Figure 6.5: Left: Overall average thickness (H, red circles) of the PB-$_b$-PEO lamellar crystals and calculated PEO thickness (d_{PEO}, black squares) as a function of the PEO block weight fraction. Right: Folded chain number of the PEO block (n_f, black triangles) of the lamellar crystals and the polymerization degree of the PEO (N_{PEO}, red triangles) as a function of the PEO block weight fraction.

The d_{PEO} values were calculated for the lamellar morphologies formed at weight fractions varying between 0.32 and 0.69 (Fig. 6.5). The thickness of the core is determined by the number of folds, n_f and the length of the crystallisable block:

$$d_{PEO} = \frac{L_{PEO}}{n_f + 1} \tag{6.2}$$

where the L_{PEO} is the unfolded length of PEO block with a helical conformation, L_{PEO} = 0.2783* N_{PEO} and a repeating unit of 0.2783 nm. The estimated folds number are plotted in Fig. 6.5 as a function of the PEO block weight fraction w_{PEO}. The n_f increases as the weight fraction w_{PEO} and the polymerization degree of the PEO, N_{PEO} increase. A large number of chain folds, n_f, leads to strong repulsions and to a sharp interface between the crystalline PEO core and the solvent- swollen PB corona, favoring smaller lamellar thickness, d_{PEO}.

One has to take into account that, the n_f is limited by the length of the PEO block. In this case, the behavior of the $B_{53}EO_{47}$ (w_{PEO}= 0.47) and $B_{52}EO_{48}$ (w_{PEO}= 0.48) block copolymers at the T_c was compared. In the $B_{53}EO_{47}$ and $B_{52}EO_{48}$ block copolymers, the fully extended chains of the PEO with a helical conformation are 31.72 nm and 16.97 nm, respectively. The PEO block is two times folded in the $B_{53}EO_{47}$ (N_{PEO}= 114) block copolymer, whereas in the smaller $B_{52}EO_{48}$ (N_{PEO}= 61) block copolymer exhibits only one fold. As the folding number increase, the core curvatures decreased and the lateral

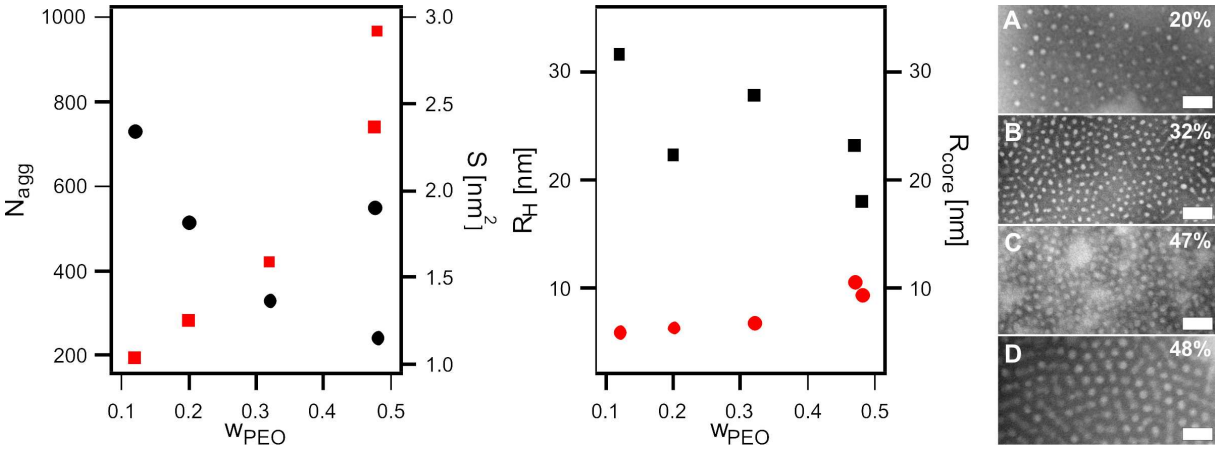

Figure 6.6: Left: The aggregation number, N (red squares), and the area occupied per PB block, S (black circles) as a function of the PEO block weight fraction. Right: Hydrodynamic radius (black squares) of the spherical micelles and PEO core radius (red circles) evaluated from the stained TEM micrographs as a function of the weight fraction of the PEO block. TEM micrographs of spherical block copolymer micelles formed in *n*-heptane: (A) $B_{80}EO_{20}$ (w_{PEO}= 0.20); (B) $B_{68}EO_{32}$ (w_{PEO}= 0.20); (C) $B_{53}EO_{47}$ (w_{PEO}= 0.32);(D) $B_{52}EO_{48}$ (w_{PEO}= 0.48). Osmium tetroxide was used as a staining agent to improve the contrast. The scale bars were 200 nm.

growth of the crystals was enlarged.

Aggregation Number. Representative TEM images of spherical micelles formed via the pathway A are reported in Fig. 6.6. Imaging of the micellar core was possible after staining the samples with osmium tetroxide, which reacts only with the PB chains. The PEO core diameters varied from 12 to 20 nm as the PEO block weight fractions increased.

When the dimension of the core in the micelles is known, we can estimate the aggregation number and the area occupied per PB block from the density of the PEO block. Assuming that the density of the crystalline micelles is the same as in the bulk (ρ_{PEO}= 1.239 g/ cm^3), the aggregation number (N) is:

$$N_{agg} = \frac{4/3\pi R_{PEO}^3 \rho_{PEO}}{M_{PEO}} * 6.02 * 10^{23} \tag{6.3}$$

where the ρ_{PEO} and M_{PEO} are the density and the number average molecular weight of the PEO block. The area occupied per PB block (S) is:

$$S = \frac{4\pi R_{PEO}^2}{N_{agg}} \tag{6.4}$$

Fig. 6.6 illustrates the estimated aggregation number (N_{agg}) and the area occupied per PB block (S). Larger aggregation numbers are expected for crystalline polymers because of higher driving force for aggregation compared to the amorphous polymers. According to Vilgis and Halperin [4] theory where the crystalline chain adopts a folding conformation, the minimization of the core-solvent interfacial energy favors a decrease in the surface area per chain, which results in an increase of the aggregation number. As emphasized in Fig. 6.6 the spherical micelles formed by PB-*b*-PEO diblock copolymers in *n*- heptane follow this prediction. The aggregation number (N_{agg}) increases with the weight fraction of the PEO block. In block copolymers with longer amorphous block the entropy of the amorphous block has a larger contribution to the total free energy, whereas the amorphous block is densely packed rather then highly stretched. The densely packed amorphous block protect the lateral interface from interaction with the solvent and hinders the aggregation of block copolymers, which explains the formation of structures of high curvature, i.e. spherical micelles at lower composition of the PEO block. The diblock copolymers with a w_{PEO} composition between 0.12 to 0.22 formed spherical micelles at the T_c of the PEO block.

In the present work, we observed that via pathway A, the spherical morphology present in the molten state at 70^0C is retained at PEO compositions between 20- 48%. Here, crystallization sets in the PEO cores very fast imposing a number of folds. At the same time, we can imagine that exist barriers preventing rearrangements to lamellar structures imposed by the densely packed amorphous block, which protects the lateral interface from interaction with *n*-heptane. Moreover, at -91^0C the solvent (*n*-heptane) freezes and no further rearrangements of the micelles can occur. Therefore, the spherical shape present in the molten state is retained by rapid immersion into liquid nitrogen.

An exception from this behavior were observed at w_{PEO}= 0.12. In this case, the PB chains are long enough to impose a smaller curvature, and conformational changes from spheres to rod-like micelles occurred before the freezing point of *n*-heptane. We can emphasize that the overall effect of the amorphous PB block on the geometry of the crystalline micelles lies reasonably to the scaling predictions of Vilgis and Halperin.

6.4 Insights on the Crystalline Nature of the Morphologies

To access to the crystal structure of the micellar PEO core X-ray diffraction experiments were carried out. The XRD patterns highlighted the crystalline nature of dried mor-

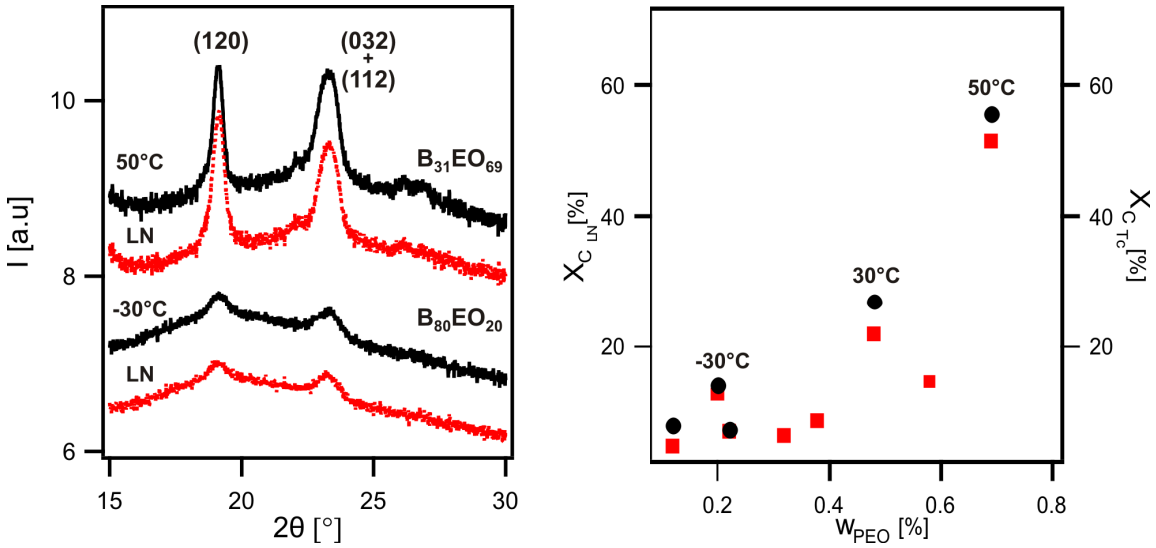

Figure 6.7: Left: Crystallinity of the PEO core: XRD patterns of films of 1wt% $B_{80}EO_{20}$ and $B_{31}EO_{69}$ polymers solutions in *n*-heptane. The red lines indicate the diffraction patterns of the block copolymer morphologies formed by pathway A: spheres ($B_{80}EO_{20}$) and branched cylinders ($B_{31}EO_{69}$); whereas, the black lines represent the diffraction patterns of the morphologies formed by pathway B: spheres ($B_{80}EO_{20}$, T_c= -30^0C) and dendrites ($B_{31}EO_{69}$, T_c= 50 ^0C). The XRD patterns were shifted along the ordinate for a better visualization. The diffraction patterns are attributed to (120) and (032+ 112) PEO reflections. Right: Crystallinity degree dependence of the morphologies formed by: pathway A (Xc_{LN}, red squares) and pathway B (Xc_{Tc}, black circles).

phologies; whereas, WAXS measurements were performed on the polymer solutions [19]. Fig. 6.7 displays the XRD patterns of the films of 1wt% $B_{80}EO_{20}$ and $B_{31}EO_{69}$ polymers solutions in *n*-heptane. One can see from Fig. 6.7 that the two XRD peaks appear at 2Θ = 19^0, 23^0, which are assigned to (120) and (032 + 112) reflexions of polyethylene oxide crystallized in its monoclinic modification [24]. Only the $B_{88}EO_{12}$ diblock copolymer shows a triclinic modification of the PEO block [20, 25].

The degree of crystallinity (X_c) was estimated from the XRD patterns, as the ratio between the areas below the crystalline Bragg peaks to the total scattered area [26]. As emphasized in Fig. 6.7 (Right) the weight fraction of the PEO block is the major parameter that affects the X_c of the structures rather then the thermal history of the polymers solutions. The observed variation in the peaks intensities is directly related with the difference in the PEO block composition. As the w_{PEO} in the block copolymer increases, the crystallinity degree Xc_{Tc} shifts to higher values when the morphology varied from spheres to lamellar structures (pathway B). The same trend was observed in the Xc_{LN} when the polymers solutions are quenched into liquid nitrogen (pathway

A). The maximum crystallinity values were reached at the highest PEO composition. Small variations in X_c were observed between the morphologies formed through pathway A and pathway B, respectively at the same w_{PEO}. Our previous time-resolved WAXS investigations of the $B_{52}EO_{48}$ block copolymer reveled that the meander morphology formed via the pathway B, had a higher X_c compared with the spherical micelles obtained though the pathway A [19].

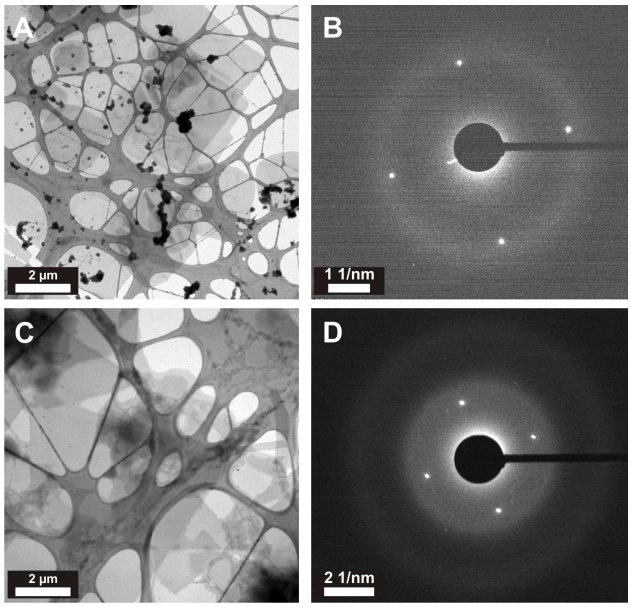

Figure 6.8: Cryo-TEM micrographs and selected area diffraction of platelets structures of $B_{68}EO_{32}$ (A-B) and $B_{62}EO_{38}$ (C-D) diblock copolymers. The diffraction patterns are attributed to (120) PEO reflections.

Fig. 6.8 shows the cryo-TEM micrographs of the platelet morphologies formed via pathway B of the $B_{68}EO_{32}$ (A) and $B_{62}EO_{38}$ (C) diblock copolymers. Selected area electron diffraction (SAED) of the platelet structures was carried out at the same conditions as the cryo- TEM investigations. The four strong diffraction spots were attributed to the (120) plane of the monoclinic PEO crystals (Fig. 6.8 (B, D)).

Generality of the Method. Fig. 6.9 summarizes the diagram of the PB-*b*-PEO crystalline morphologies in *n*-heptane as a function of molecular size and composition, where N_{PEO} and w_{PB} are the degree of polymerization and weight fraction of the PEO and PB blocks, respectively. This representation describes the tendency of the micelles (present in the molten state at 70^0C) to reorganizes at different crystallization conditions.

As crystallization takes place at low temperatures (pathway A), the spherical morphology is mostly retained at compositions of the PB block ≥ 0.52. The spherical morphology of the melt, breaks-out at the crystallization temperature of the PEO block

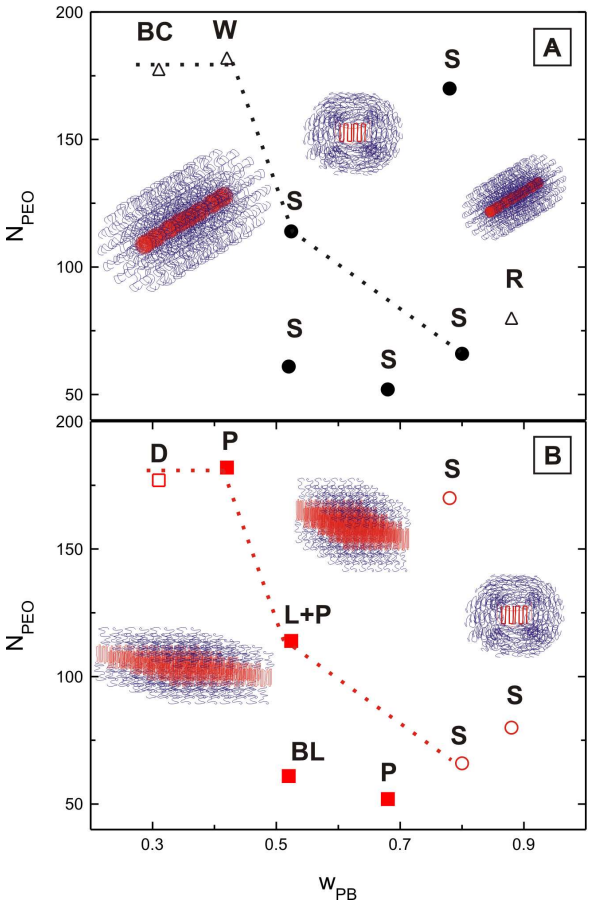

Figure 6.9: Crystalline morphology diagram for PB-*b*-PEO in *n*-heptane as a function of molecular size and composition, where N_{PEO} and w_{PB} are the degree of polymerization and weight fraction of the PEO and PB blocks, respectively. Two basic morphologies-spheres (S) and cylinders (referred as rods (R), worms (W) and twisted cylinders (BC)) formed by immersion into liquid nitrogen, pathway A (Top graph). As a decreasing of the PB block composition, at the crystallization temperature of the PEO block (pathway B, bottom graph) spheres (S), lamellae (L) or branched lamellae (BL), platelets (P) and dendrites (D) formed in the solutions. Mixed population of lamellae + platelets (L + P) was observed at w_{PB}= 0.53. The dashed lines establish the morphological trend of the PB-*b*-PEO block copolymers at similar molecular weights, M_n.

(pathway B) after w_{PB}= 0.68. Here, transitions from spheres to lamellar morphologies are observed. Decreasing the size of the PB block below 42%, the worm-like micelles are retained into liquid nitrogen, whereas pathway B leads to larger morphologies as platelets or dendrites. At equal composition of the PEO and PB block, crystallization induced aggregation of the spherical units of the melt, favoring the development of branched cylinders (BL, meanders) [19], platelets (P), and lamellae with platelets (L + P). An exception occurred at w_{PB}= 0.88, where rod- like micelles formed via pathway

A, whereas pathway B retained the spherical shape present in the molten state [20].

The present results can be hence qualitatively compared to data obtained by Jain and Bates [27], for PB-*b*-PEO morphologies in water. Even if, the PEO block is not crystallizing in water, the self-assembly behavior of the PB-*b*-PEO block copolymers in selective solvents, i.e., water and *n*-heptane, followed a similar trend. These authors reported that spherical micelles are formed at high PEO weight fraction whereas, morphological transitions to cylinders or bilayers are observed with the decrease of the PEO block fraction. Mixed morphologies like spheres with cylinders, or cylinders with bilayers appeared to coexist in a broad overlapping range between 0.60 and 0.40. In this study, we observed that pathway B, in the same broad range (0.40-0.60) favors the coexistence of crystalline morphologies. Phenomena of morphological coexistence is believed to occurs as a consequence of the polydispersity in chain lengths, which allows assembly in more than one aggregate geometry. Here, crystallization is the main driving force that controls the morphology evolution in a selective solvent additionally to the block lengths variation.

6.5 Conclusion

In conclusion, we demonstrated that crystalline morphologies of poly(butadiene)-*block*-poly(ethylene oxide) diblock copolymers in *n*-heptane can be controlled by the crystallization temperature and by the block lengths of the polymer. A convenient way to generate crystalline morphologies from a selective solvent condition (from 70^{o}C, that is, above the melting point of PEO) via two thermal histories is described: pathway A, that is, direct immersion into liquid nitrogen of the hot solutions leads to the formation of rods, spheres, and cylinders as the crystalline PEO core content was increased. Moreover, the aggregation number of the spherical micelles increased with the weight fraction of the crystalline PEO block.

In case of pathway B, i.e., quenching of the hot solutions to the crystallization temperature of the PEO block, leads to spherical micelles formation for the block copolymers with the shortest PEO block. As the composition of the PEO block increases, the micellar morphology evolves into lamellae, platelets and dendrites structures. An increase of the chain folding number was observed at high PEO composition, which in turn reduced the lamellar thickness of the crystals. At equal composition of the PEO and PB block, crystallization induced aggregation of the spherical units of the melt upon cooling, favoring the development of branched lamellae (meanders), platelets and lamellae with

platelets, respectively.

Acknowledgments

Financial support by the Deutsche Forschungsgemeinsschaft, SFB 481, Bayreuth, is gratefully acknowledged. The authors thank Dr. Markus Drechsler and Carmen Kunert for the TEM investigation. The authors thank Michael Möller for the XRD investigations. We thank Dr. Emanuela Di Cola for assistance with the WAXS experiments at ESRF. A.M.M. acknowledge the financial support from the European Community's "Marie-Curie Actions" under Contract No. MRTN-CT-2004-504052 [POLYFILM].

Bibliography

[1] B. Lotz and A. J. Kovacs. *Kolloid Z.Z.Polym.*, 209:97–114, 1966.

[2] B. Lotz, A. J. Kovacs, G. A. Bassett, and A. Keller. *Kolloid Z.Z.Polym.*, 209:115–128, 1966.

[3] E. K. Lin and A. P. Gast. *Macromolecules*, 29:4432–4441, 1996.

[4] T. Vilgis and A. Halperin. *Macromolecules*, 24:2090–2095, 1991.

[5] D. Richter, D. Schneiders, M. Monkenbusch, L. Willner, L. J. Fetters, J. S. Huang, M. Lin, K. Mortensen, and B. Farago. *Macromolecules*, 30:1053–1068, 1997.

[6] J. T. Xu, J. P. A. Fairclough, S. M. Mai, and A. J. Ryan. *J. Mater. Chem.*, 13:2740–2748, 2003.

[7] J. Fu, B. Luan, X. Yu, Y. Cong, J. Li, C. Pan, Y. Han, Y. Yang, and B. Li. *Macromolecules*, 37:976–986, 2004.

[8] J. A. Massey, K. Temple, L. Cao, Y. Rharbi, J. Raez, M. A. Winnik, and I. Manners. *J. Am. Chem. Soc.*, 122:11577–11584, 2000.

[9] L. Shen, H. Wang, G. Guerin, C. Wu, I. Manners, and M.A Winnik. *Macromolecules*, 41:4380–4389, 2008.

[10] J. Raez, J. P. Tomba, I. Manners, and M. A. Winnik. *J. Am. Chem. Soc.*, 125:9546–9547, 2003.

[11] J. Raez, I. Manners, and M. A. Winnik. *Langmuir*, 18:7229–7239, 2002.

[12] X. Wang, H. Wang, D. J. Frankowski, P. G. Lam, P. M. Welch, M. A. Winnik, J. Hartmann, I. Manners, and R. J. Spontak. *Adv. Mater.*, 19:2279 – 2285, 2007.

[13] Z. X. Du, J. T. Xu, and Z. Q. Fan. *Macromolecules*, 40:7633–7637, 2007.

[14] H. Schmalz, J. Schmelz, M. Drechsler, J. Yuan, A. Walther, K. Schweimer, and A. M. Mihut. *Macromolecules*, 41:3235–3242, 2008.

[15] M. Lazzari, D. Scalarone, C. Vazquez-Vazquez, and M. A. Lopez-Quintela. *Macromol. Rapid Commun.*, 29:352–357, 2008.

[16] Z. X. Du, J. T. Xu, and Z. Q. Fan. *Macromol. Rapid Commun.*, 29:467–471, 2008.

[17] T. Gädt, N. S. Ieong, G. Cambridge, Winnik M. A., and Manners I. *Nat. Mater.*, 8:144 – 150, 2009.

[18] J. Raez, I. Manners, and M. A. Winnik. *J. Am. Chem. Soc.*, 124:10381–10395, 2002.

[19] A. M. Mihut, A. Chiche, M. Drechsler, H. Schmalz, E. Di Cola, G. Krausch, and H. Schmalz. *Soft Matter*, 5:208–213, 2009.

[20] A. M. Mihut, M. Drechsler, M. Möller, and M. Ballauff. *accepted to Macromol. Rapid. Commun.*

[21] A. M. Mihut, J.J. Crassous, H. Schmalz, and H. Schmalz. *to be submitted.*

[22] S. Fröster and E. Krämer. *Macromolecules*, 32:2783–2785, 1999.

[23] M. A. Hillmyer and F. S. Bates. *Macromolecules*, 29:6994–7002, 1996.

[24] H. Tadokoro, Y. Chatani, T. Yoshihara, S. Tahara, and S. Murahashi. *Makromol. Chem.*, 73:109–127, 1964.

[25] Y. Takahashi, I. Sumita, and H. Tadokoro. *J. Polym. Sci., Part B: Polym. Phys.*, 11:2113–2122, 1973.

[26] C. G. Vonk. *J. Appl. Crystallogr.*, 6:148–152, 1973.

[27] S. Jain and F. S. Bates. *Science*, 300:460–464, 2003.

CHAPTER 7

Summary

This thesis reports the development of micellar crystalline morphologies in a selective solvent. The phase diagram of solution morphologies as a function of the molecular composition of the semicrystalline poly(butadiene)-*b*-poly(ethylene oxide)(PB-*b*-PEO) block copolymers was investigated. The crystalline morphologies discussed here have been generated from selective solvent condition (70^{o}C in *n*-heptane) via two thermal pathways: (A) by direct immersion into liquid nitrogen, where *n*-heptane becomes a poor solvent for both blocks at very low temperatures, and (B): by quenching to the crystallization temperature of the PEO, i.e., determined by the length of PEO block. In pathway B, *n*-heptane is a poor solvent only for the PEO block. At 70^{o}C, the block copolymers self-assembled into micellar structures consisting of a PEO molten core and a soluble PB corona. As crystallization takes place in the PEO core, a fast quenching into liquid nitrogen results in the formation of crystalline micelles retaining the shape present in the molten state at 70^0C (pathway A). In the case of pathway B, the competition between the PEO core crystallization and the self-assembly of the micellar units, is the driving force that dictates the morphological development, therefore crystallization breaks out the melt morphology. These studies, demonstrated that the PB-*b*-PEO block copolymers are a promising system models for developing a general route towards tunable crystalline morphologies.

In a symmetric PB-*b*-PEO block copolymer, crystalline morphologies like spheres and meanders formed upon quenching into liquid nitrogen and at 30^{o}C, respectively. The

meander morphology consisting of branched lamellae with a crystalline PEO ribbon-like core and ellipsoidal endings was observed for the first time in solution. Investigations of the crystal development revealed that this structure formed via crystallization-induced aggregation of spherical micelles upon cooling.

A systematic study of the effect of crystallization kinetics on the formed morphology upon crystallization-induced aggregation of spherical micelles of a symmetric PB-*b*-PEO block copolymer was discussed. We demonstrated that the resulting morphology is controlled by two competitive effects, namely, by the nucleation and growth of the PEO micellar core: at lower crystallization temperatures ($T_c \leq 30^0C$), a high nucleation rate leads to a meander-like morphology formation, whereas at higher crystallization temperatures ($T_c > 30^0C$), a low nucleation rate favors the formation of twisted lamellae.

For a highly asymmetric PB-*b*-PEO block copolymer, crystallization at -30^0C induced the formation of crystalline micelles retaining the spherical shape present in the molten state at 70^0C. However, a quenching into liquid nitrogen facilitated a transition to rod-like micelles caused by changes of solvent quality for the PB coronar chains. This triggers the onset of an interfacial instability, therefore the spherical micelles preferred to reorganize into a morphology with a smaller interfacial curvature. The low crystallinity of the PEO core imposed a stronger tendency of the rods to aggregate and to thicken into more stable morphologies as needle-like structures, with a preferred growth direction along the long axis.

Finally, the micellar morphology diagram of the PB-*b*-PEO block copolymers has been studied as a function of the crystallization temperature and molecular composition of the blocks via two thermal pathways. Pathway A allowed morphological transitions from spheres to rods, worms or twisted cylinders with the increase of the crystalline content of the PEO core. In Pathway B, the sequence of spheres, cylinders, lamellae, platelets and dendrites structures is observed with the increases of the PEO block length. The aggregation number of the spherical micelles is affected by the weight fraction and crystallinity of the PEO block. Moreover, an increased chain folding was observed at a high PEO composition which reduced the lamellar thickness of the crystals. The competition between the PEO core crystallization and the aggregation of the micellar units leads to coexistence regions of lamellae with platelets and cylinders with platelets.

The novelty of this thesis relies on the development of novel crystalline morphologies in a selective solvent, as well as, in the detailed analysis of the major parameters that govern morphological formation in a controlled manner.

Zusammenfasssung

In der vorliegenden Arbeit wird über die Bildung mizellarer kristalliner Morphologien in einem selektiven Lösungsmittel berichtet. Dazu wurde das Phasendiagramm der Morphologien des semikristallinen Blockcopolymers Poly(butadien)-*b*-Poly(ethylenoxid) (PB-*b*-PEO) in Lösung in Abhängigkeit von der molekularen Zusammensetzung untersucht. Die kristallinen Morphologien wurden aus selektiven Lösungsbedingungen (70^{o}C in *n*-Heptan) über zwei thermische Wege dargestellt. Weg A bestand in direktem schnellem Abkühlen in flüssigem Stickstoff. Bei diesen Temperaturen wird *n*-Heptan ein schlechtes Lösungsmittel für beide Polymerblöcke. Weg B bestand im Abkühlen auf die Kristallisationstemperatur von PEO, die durch die Länge des PEO-Blocks bestimmt ist. Bei dem Weg B ist *n*-Heptan lediglich für den PEO-Block ein schlechtes Lösungsmittel. Bei 70^{o}C formen die Blockcopolymere mizellare Strukturen aus einem geschmolzenen PEO-Kern und einer gelösten PB-Schale. Da die Kristallisation im PEO-Kern stattfindet, führt schnelles Abkühlen in flüssigem Stickstoff zur Bildung kristalliner Mizellen, die ihre Form aus dem geschmolzenen Zustand bei 70^{o}C behalten (Weg A). Im Fall des Weges B bestimmt die Konkurrenz zwischen der Kristallisation des PEO-Kerns und der Selbstanordnung der mizellaren Einheiten die Entwicklung der Morphologie. Daher kann die Kristallisation die Morphologie aus der Lösung verändern. Durch diese Untersuchungen wird gezeigt, dass PB-*b*-PEO Blockcopolymere vielversprechende Modelsysteme sind, um einen allgemeinen Weg zu einstellbaren kristallinen Morphologien zu entwickeln.

In einem symmetrischen PB-*b*-PEO Blockcopolymer formen sich durch Abkühlen in flüssigem Stickstoff bzw. auf 30^{o}C kugel- und meanderförmige Strukturen als kristalline

Morphologien. Die Meander-Morphologie besteht aus verzweigten Lamellen mit einem kristallinen PEO-Band als Kern und ellipsoiden Enden und wurde zum ersten Mal in Lösung beobachtet. Untersuchungen der Bildung der kristallinen Strukturen zeigte, dass diese Struktur beim Abkühlen durch Aggregation der kugelförmigen Mizellen während des Kristallisationsprozesses entstehen.

Der Einfluss der Kristallisationskinetik auf die gebildete Morphologie durch die vom Kristallisationsvorgang induzierte Aggregation der kugelförmigen Mizellen eines symmetrischen PB-*b*-PEO Blockcopolymers wurde in einer systematischen Untersuchung behandelt. Es konnte gezeigt werden, dass die entstehende Morphologie durch die zwei konkurrierenden Effekte Keimbildung und Wachstum des mizellaren PEO-Kerns kontrolliert wird. Bei tiefer Kristallisationstemperatur führt die hohe Keimbildungsrate zur Bildung der meanderförmigen Morphologie, während bei hoher Kristallisationstemperatur durch die geringere Keimbildungsrate die Bildung von verdrehten Lamellen bevorzugt ist.

Für stark asymmetrische PB-*b*-PEO Blockcopolymere bleibt die kugelförmige Morphologie mit einem geschmolzenen PEO-Kern, die in Lösung bei 70^{o}C vorliegt, erhalten, wenn die Kristallisation bei -30^{o}C stattfindet. Ein schnelles Abkühlen in flüssigem Stickstoff führt zu einem bergang zu stäbchenförmigen Mizellen, die von einer Veränderung der Lösungsmittelqualität für die PB-Ketten der Schale herrührt. Die entstehende Instabilität der Grenzfläche führt zu einer Umorganisation der kugelförmigen Mizellen zu einer Morphologie mit kleinerer Krümmung der Grenzfläche. Die geringe Kristallinität des PEO-Kerns bedingt eine stärkere Tendenz der Stäbchen zu aggregieren und sich zu stabileren Strukturen, wie zum Beispiel nadelförmige Strukturen, zu verdicken. Die bevorzugte Wachstumsrichtung ist dabei entlang der langen Achse der Stäbchen.

Schlielich wurde das Diagramm der mizellaren Morphologien von PB-*b*-PEO Blockcopolymeren als Funktion der Kristallisationstemperatur und der molekularen Zusammensetzung der Blöcke über zwei thermische Wege untersucht. Über den Weg A waren mit der Zunahme des kristallinen Anteils des PEO-Kerns morphologische Übergänge von kugelförmigen zu stäbchen- und wurmartigen Strukturen sowie verdrehten Zylindern möglich. Auf dem Weg B wurden mit der Zunahme der Länge des PEO-Blocks die Morphologien Kugeln, Zylinder, Lamellen, Plättchen und dendritische Strukturen beobachtet. Die Aggregationszahl der kugelförmigen Mizellen wird von dem Gewichtsanteil und der Kristallinität des PEO-Blocks beeinflusst. Weiterhin wurden eine stärkere Kettenfaltung bei hohen PEO-Anteilen beobachtet, die zu einer verringerten Lamellendicke der Kristalle führte. Die Konkurrenz zwischen der Kristallisation des PEO-Kerns

und der Aggregation der mizellaren Einheiten führt zu Gebieten in denen Lamellen mit Plättchen und Zylinder mit Plättchen nebeneinander auftraten. Die Neuheit dieser Arbeit besteht in der Darstellung, wie neue kristalline Strukturen in einem selektiven Lösungsmittel entstehen sowie in der detaillierten Analyse der wichtigsten Parameter, die die Bildung der Morphologien kontrollieren.

Erklärung

Die vorliegende Arbeit wurde von mir selbständig verfasst und ich habe dabei keine anderen als die angegebenen Hilfsmittel und Quellen benutzt. Ferner habe ich nicht versucht, anderweitig mit oder ohne Erfolg eine Dissertation einzureichen oder mich der Doktorprüfung zu unterziehen.

Bayreuth, den 21.10.2009

Adriana Mirela Mihut